ΠΟΛΥΤΕΧΝΕΙΟ ΚΡΗΤΗΣ

Σχολή Χημικών Μηχανικών και
Μηχανικών Περιβάλλοντος

Κατεύθυνση: Μηχανικών Περιβάλλοντος

Η ΜΕΓΑΛΗ ΠΥΡΚΑΓΙΑ ΤΟΥ ΕΒΡΟΥ ΤΟΥ 2023 ΚΑΙ Η ΜΕΛΕΤΗ ΣΥΣΧΕΤΙΣΗΣ ΤΗΣ ΜΕ ΤΗΝ ΚΛΙΜΑΤΙΚΗ ΑΛΛΑΓΗ

ΔΙΠΛΩΜΑΤΙΚΗ ΕΡΓΑΣΙΑ

ΤΗΣ

ΠΑΡΑΣΚΕΥΗΣ ΡΩΜΗ ΚΥΡΙΜΗ

ΕΠΙΒΛΕΠΩΝ ΚΑΘΗΓΗΤΗΣ

ΑΠΟΣΤΟΛΟΣ ΒΟΥΛΓΑΡΑΚΗΣ

ΤΡΙΜΕΛΗΣ ΕΠΙΤΡΟΠΗ

ΑΠΟΣΤΟΛΟΣ ΒΟΥΛΓΑΡΑΚΗΣ

ΕΜΜΑΝΟΥΗΛ ΓΡΥΛΛΑΚΗΣ

ΑΡΙΣΤΕΙΔΗΣ ΚΟΥΤΡΟΥΛΗΣ

ΧΑΝΙΑ, ΣΕΠΤΕΜΒΡΙΟΣ, 2025

COMMITTEE

Voulgarakis Apostolos Professor,
School of Chemical and Environmental Engineering TUC

Koutroulis Aristeidis Associate Professor,
School of Chemical and Environmental Engineering TUC

Grillakis Emmanouil Laboratory Teaching Staff,
School of Chemical and Environmental Engineering TUC

Ευχαριστίες

Ευχαριστώ θερμά τον κύριο Απόστολο Βουλγαράκη, επιβλέποντα καθηγητή, καθώς και τον κύριο Μανώλη Γρυλλάκη, για την καθοδήγηση και την πολύτιμη βοήθειά τους καθ' όλη τη διάρκεια εκπόνησης της διπλωματικής μου εργασίας. Παρά τις πολλές τους υποχρεώσεις, αφιέρωναν πάντοτε χρόνο και διάθεση για να συζητήσουν τόσο τα ζητήματα που προέκυπταν στην εργασία, όσο και όσα άλλα θέματα ζητούσα τη συνδρομή τους. Το ερευνητικό τους έργο υπήρξε για εμένα πηγή έμπνευσης. Ιδιαίτερη χαρά και τιμή αποτέλεσε η συνεργασία μου με το Εργαστήριο Ατμοσφαιρικού Περιβάλλοντος και Κλιματικής Αλλαγής, από το οποίο αποκόμισα γνώσεις και εμπειρίες μέσα σε ένα ιδιαίτερα ευχάριστο περιβάλλον. Επίσης, θα ήθελα να ευχαριστήσω θερμά τον κύριο Αριστείδη Κουτρούλη, ο οποίος, παρά το ιδιαίτερα απαιτητικό πρόγραμμά του, βρήκε τον απαραίτητο χρόνο να συμμετάσχει στην επιτροπή.

Οφείλω ένα τεράστιο ευχαριστώ στους γονείς μου και ειδικά στην μητέρα μου, η οποια δεν σταματάει ποτέ να παλεύει για το καλύτερο. Σημαντικό είναι και το ευχαριστώ προς τις φίλες και φίλους μου που με βοηθούσαν ψυχικά και πρακτικά όποτε το χρειαζόμουν και προς τον άνθρωπο που έκανε αυτά τα τελευταία φοιτητικά χρόνια τόσο ξεχωριστά. Τέλος, ευχαριστώ όλα τα Φρουντ αυτού του κόσμου.

Περίληψη

Η πυρκαγιά του 2023 στον Έβρο, στη βορειοανατολική Ελλάδα, αποτέλεσε τη μεγαλύτερη που έχει καταγραφεί ποτέ στην Ευρωπαϊκή Ένωση, καίγοντας σχεδόν 94.000 εκτάρια και αναδεικνύοντας επείγοντα ερωτήματα σχετικά με τον ρόλο της κλιματικής αλλαγής σε ακραία επεισόδια πυρκαγιών. Η παρούσα διπλωματική εργασία εξετάζει τις μετεωρολογικές συνθήκες κατά τη διάρκεια του γεγονότος και επιχειρεί να αξιολογήσει σε ποιον βαθμό η ανθρωπογενής κλιματική αλλαγή συνέβαλε στην πιθανότητα εμφάνισης τέτοιων ακραίων συνθηκών.

Η ανάλυση συνδύασε δεδομένα επανάλυσης και σύνολα δεδομένων κλιματικών σεναρίων. Αρχικά, χρησιμοποιήθηκαν μετεωρολογικά δεδομένα από το ERA5 (Copernicus Climate Change Service, ECMWF) για τους μήνες Ιούλιο–Σεπτέμβριο, κατά την περίοδο 1940–2024. Εξετάστηκαν η θερμοκρασία, η σχετική υγρασία, η ταχύτητα ανέμου και η βροχόπτωση, και υπολογίστηκε ο δείκτης επικινδυνότητας πυρκαγιάς Fire Weather Index (FWI). Παράλληλα, χρησιμοποιήθηκαν δεδομένα από την πρωτοβουλία ISIMIP3a (GSWP3–W5E5) υπό δύο σενάρια: obsclim (επανάλυση με ανθρωπογενείς επιδράσεις) και counterclim (επανάλυση χωρίς ανθρωπογενείς επιδράσεις), επιτρέποντας ανάλυση απόδοσης (attribution).

Τα αποτελέσματα δείχνουν ότι κατά την πυρκαγιά του Έβρου επικράτησαν εξαιρετικά ευνοϊκές συνθήκες για την εξάπλωση της φωτιάς. Τα δεδομένα ERA5 κατέγραψαν παρατεταμένο καύσωνα, πολύ χαμηλή υγρασία, ισχυρούς ανέμους και ελάχιστη βροχόπτωση, με τιμές FWI που ξεπέρασαν τις 80 μονάδες, από τις υψηλότερες στην ιστορική σειρά. Η ανάλυση έδειξε σαφή αύξηση των ημερών με FWI άνω του 90ού και 95ού εκατοστημορίου μετά τη δεκαετία του 1990, σε συμφωνία με τη θερμότερη και ξηρότερη θερινή κλιματολογία της Μεσογείου. Η σύγκριση obsclim–counterclim αποκάλυψε ότι τα παρατηρημένα άκρα θα ήταν πολύ λιγότερο πιθανά χωρίς την ανθρωπογενή θέρμανση. Ειδικά για το διάστημα 19 Αυγούστου–3 Σεπτεμβρίου 2023, οι περισσότερες ημερήσιες τιμές FWI αντιστοιχούσαν σε ≥99ο εκατοστημόριο στο counterclim, υπογραμμίζοντας την εξαιρετική σπανιότητά τους σε ένα «φυσικό» κλίμα.

Η εργασία καταδεικνύει με σαφήνεια ότι το ανθρωπογενές σήμα της κλιματικής αλλαγής έχει μετατοπίσει την στατιστική κατανομή του FWI προς υψηλότερες τιμές, αυξάνοντας σημαντικά την πιθανότητα ακραίων επεισοδίων όπως η πυρκαγιά του Έβρου. Τα ευρήματα υπογραμμίζουν τη σημασία ενσωμάτωσης της κλιματικής απόδοσης στην αξιολόγηση κινδύνου και στη διαχείριση πυρκαγιών στη Μεσόγειο.

Abstract

The 2023 wildfire in the Evros region of northeastern Greece was the largest ever recorded in the European Union, burning nearly 94,000 hectares and raising urgent questions about the role of climate change in extreme fire events. This thesis investigates the meteorological conditions during the event and evaluates to what extent anthropogenic climate change influenced the likelihood of such extremes.

The analysis combined reanalysis and impact-model datasets. First, meteorological data from ERA5 (Copernicus Climate Change Service, ECMWF) were retrieved for July–September over the period 1940–2024. Temperature, relative humidity, wind speed, and precipitation were analyzed and used to compute the Fire Weather Index (FWI). In parallel, bias-adjusted climate input from ISIMIP3a (GSWP3–W5E5) was examined under two scenarios: obsclim (with anthropogenic forcing) and counterclim (without anthropogenic forcing), allowing an attribution assessment.

Results show that during the Evros wildfire, meteorological conditions were exceptionally conducive to fire spread. ERA5 data indicate a persistent heat episode, very low humidity, strong winds, and negligible rainfall, producing FWI values that peaked above 80, among the highest on record. Analysis of the historical series revealed a clear upward shift in the frequency of days exceeding the 90th and 95th percentiles of FWI after the 1990s, consistent with Mediterranean summer warming and drying. Comparison of obsclim and counterclim scenarios demonstrated that the observed extremes would have been far less probable in a climate without anthropogenic warming. Specifically, during 19 August–3 September 2023, most daily FWI values corresponded to ≥99th percentiles in the counterclim world, highlighting their exceptional rarity in the absence of human influence.

This work provides robust evidence that the anthropogenic climate signal has shifted the distribution of fire weather conditions in northeastern Greece, substantially increasing the likelihood of extremes such as the 2023 Evros wildfire. The findings underscore the importance of integrating climate attribution into fire risk assessment and preparedness planning in the Mediterranean.

Table of Contents

List of Figures

List of Tables

1. Introduction

Fires are natural combustion processes with a worldwide presence, playing a significant role in shaping ecosystems, carbon cycles, and climate. Literature highlights that, although humans have coexisted with fire for millennia, managing it is becoming harder in a changing climate [Bowman et al., 2020]. Fires, and especially wildfires, are multifactorial phenomena in which ignition, the amount and moisture content of available fuels, and "fire weather" (heat, dryness, wind) determine whether an incident will evolve into a large burn [Ruffault et al., 2020; San-Miguel-Ayanz et al., 2013]. Beyond habitat losses and material damage, the atmospheric impacts are critical. Smoke contains fine particulate matter $PM_{2.5}$, black carbon, and organic aerosols, that affect both radiation and health. As plume travels, theor chemistry evolves, producing secondary pollutants such as ozone and secondary organic aerosol, which can degrade air quality hundreds or even thousands of kilometers away. In extreme episodes, pyro-cumulonimbus (pyroCb) clouds inject smoke up to the stratosphere, causing measurable disturbances to the radiative balance. The above pollutants have been associated with increased respiratory morbidity and a deterioration in public health during periods of extensive burning [IPCC, 2021].

By climate change we refer to long-term changes in the climate system, which today are driven primarily by the rise of greenhouse gases from human activities (energy, transport, land use). The IPCC (Intergovernmental Panel on Climate Change) is the UN's intergovernmental body that does not conduct primary research, but systematically assesses the global scientific knowledge base and publishes Assessment Reports. Specifically, the IPCC documents, with high confidence, anthropogenic warming, and identifies the Mediterranean as a hotspot with trends toward drier, hotter summers and an increase in days with conditions favorable to fire [Cramer et al., 2018; Turco et al., 2019]. This shift in the thermal and hydrological baseline favors lower fuel moisture and therefore increases the likelihood of large burns. In the European context, 2023 saw in Greece (the Evros region) the largest wildfire recorded in the EU since systematic records exist, demonstrating in practice how extreme conditions can translate into exceptionally large episodes [Copernicus EMS, 2023].

1.1 Negative impacts of wildfires worldwide

In recent years, many regions of the world have experienced an increase in the frequency and/or intensity of large wildfires, with extensive episodes in North America, Australia, Siberia, and parts of the Mediterranean. In this context, wildfire impacts span from the atmosphere and ecosystems to human health and the economy, with the Mediterranean considered a highly vulnerable region due to its hot and dry summer conditions [Turco et al.; 2019, IPCC, 2021].

Among the most important and immediate impacts are those related to the atmosphere and air quality. Wildfires release greenhouse gases (CO_2, CH_4, N_2O), primary particulate matter (especially $PM_{2.5}$, black/elemental and organic carbon), and precursor compounds (NO_x, VOCs, ammonia) that, through the photochemical "aging" of smoke, lead to secondary aerosols and enhancement of tropospheric ozone. In the near term, this translates into degraded visibility and substantial increases in air-quality indices—even far from the sources—as smoke clouds are transported on continental scales. Aerosols alter the radiative balance (surface dimming, localized heating aloft) and affect cloud microphysics. In particularly intense episodes, pyro-cumulonimbus (pyroCb) clouds, i.e., thunderstorm clouds generated by the fire's own hot updraft, can loft smoke into the upper

troposphere or even the lower stratosphere, prolonging particle residence times and strengthening radiative effects. In the Mediterranean, summertime anticyclonic patterns and dry–hot air masses favor regional pollution build-up. Other aerosol types (e.g., mineral dust) often co-occur, producing complex episodes [San-Miguel-Ayanz et al., 2017].

Regarding climate, warmer and drier conditions are observed, internationally associated with more days of severe fire weather and an extension of the fire season, especially in arid and hot climates such as the Mediterranean [Ruffault et al., 2020]. Beyond ignition, this has tangible consequences for the post-fire landscape:

- Lower moisture in fuels and soils for weeks to months, due to loss of vegetation cover and reduced evapotranspiration.
- Higher near-surface daytime temperatures, because burned surfaces have lower albedo and increased sensible heat flux.
- Changes in surface roughness and microscale airflow that accelerate the drying of fine fuels.

Over longer horizons, repeated burns promote a shift of vegetation toward more flammable covers (e.g., shrublands–grasslands), entrenching a higher likelihood of ignition and/or spread [Cramer et al., 2018].

Wildfires cause acute species mortality, biomass loss, and habitat fragmentation. In ecosystems with fire adaptations, moderate-intensity episodes may be part of a natural regeneration cycle. However, high-intensity or frequent burns delay recovery and shift communities toward compositions with greater flammability. As a result, critical ecosystem services are degraded, including microclimate regulation, soil retention, riparian protection, air and water quality, the provision of materials and non-timber products, and landscape values. The carbon balance is disrupted: fire emissions are followed by a period of reduced uptake due to loss of vegetation cover. If episodes recur, a forest can shift from a carbon sink to a carbon source for years, with consequences for the CO_2 budget at local and regional scales [Bowman et al., 2020; IPCC, 2021].

Equally important are the impacts on surface and groundwater, on soil formation, and on the flood risk. After fire, many soils develop water repellency, resulting in reduced infiltration and increased surface runoff. Combined with steep slopes and intense convective storms (common in Mediterranean autumn), this produces runoff peaks, erosion, elevated sediment yields, and debris-flow conditions (including coarse transported material). Water quality deteriorates (turbidity, nutrients, metals), affecting supplies and aquatic ecosystems. The international literature shows that flows and sediment yields can increase from multiples up to orders of magnitude relative to pre-fire conditions, especially when the first heavy rains follow soon after the episode. Timely deployment of erosion-control measures (mulching, contour log barriers, small check dams) significantly reduces risk [Shakesby, 2011].

‘Smoke days’ are associated with increased respiratory and cardiovascular events and excess mortality, particularly among vulnerable groups (older adults, children, people with chronic conditions). Major cities worldwide have repeatedly recorded exceedances of $PM_{2.5}$/PM_{10} guidelines during smoke transport events. The combination of heat and smoke exacerbates thermal and respiratory stress, increasing public-health needs (early warnings, clean/filtered indoor spaces, behavioral guidance, high-efficiency masks for outdoor work). For instance, during the severe wildfire episode in Athens, Greece (1–20

August 2021), daily mean $PM_{2.5}$ concentrations ranged between 8.9 and 78.7 μg/m³ on days with smoke transport [Johnston et al., 2012].

Beyond direct damage to forests, agriculture, and infrastructure, smoke days entail service disruptions (work, education), higher healthcare expenditures, and elevated civil-protection or suppression costs. In the long run, large and recurrent burns reduce landscape attractiveness (e.g., for tourism), increase insurance and financial costs, and prolong the time required for the ecological and economic recovery of affected areas.

1.2 Negative impacts of wildfires in Greece and the Mediterranean

Having outlined the general negative impacts of wildfires, the focus now moves on the Mediterranean and, specifically, on Greece, where seasonal drought, heat extremes, and the proximity of settlements to natural areas combine into a particularly vulnerable setting. Indeed, recent assessments highlight a rising trend in the frequency and extent of large wildfires across the Mediterranean basin, which is recognized as one of the most fire-prone regions in Europe [San-Miguel-Ayanz et al., 2020; Jones et al., 2024].

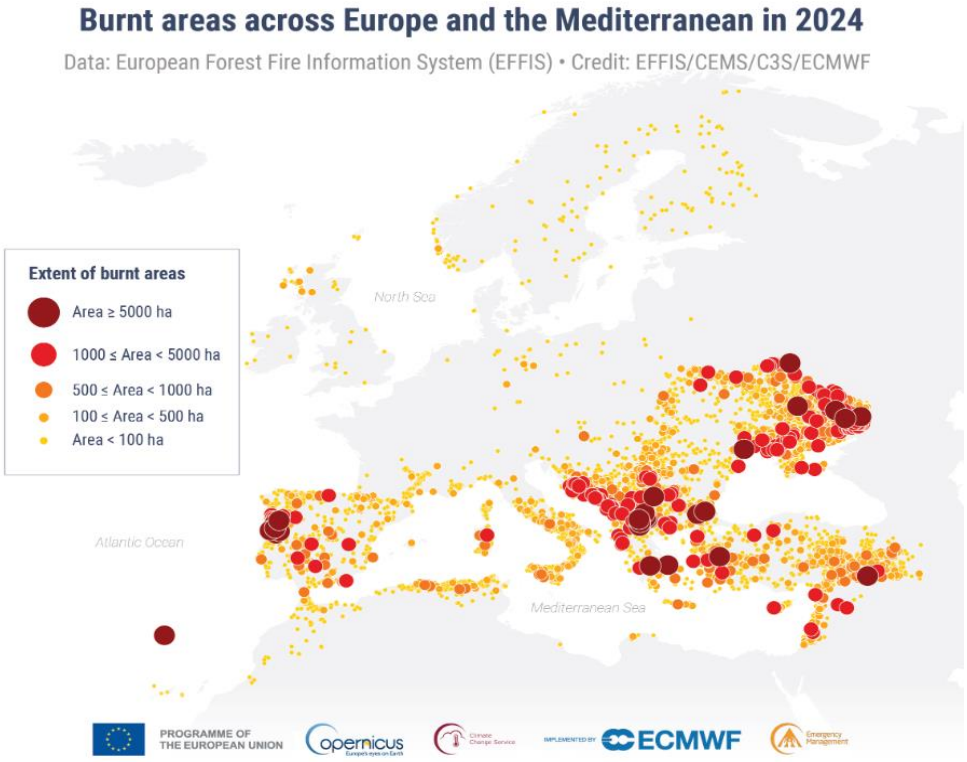

Figure 1.1. Burned area distribution across Europe and the Mediterranean during the 2023 fire season.
The map highlights the concentration of large wildfires in the Mediterranean basin, confirming the region's status as one of the most fire-prone areas in Europe.
Reproduced under CC BY 4.0 license. Source: European Commission, Joint Research Centre (JRC), "State of Wildfires 2023–2024", Earth System Science Data, 16, 3601–3685 (2024).

The Mediterranean is vulnerable to wildfires for three main reasons: (a) Climate: hot, dry summers with long rainless intervals and often strong winds. (b) Fuels: extensive pine forests, shrublands (maquis–phrygana), and agricultural mosaics that dry quickly and favor rapid fire spread. (c) People/land use: dwellings, roads, and infrastructure located

very close to natural areas (WUI – wildland–urban interface). When a heatwave, low fuel moisture, and strong winds coincide, fires tend to grow rapidly and become difficult to control [San-Miguel-Ayanz et al., 2020].

In the atmospheric domain, during large smoke episodes over urban centers (e.g., Attica, Thessaloniki), multiple consecutive days have been recorded with daily $PM_{2.5}$ in the tens of μg/m³ (locally >70 μg/m³) and PM_{10} with 24-hour values >100 μg/m³, far exceeding WHO guidelines, as already noted above. Smoke also triggers other problems: it increases tropospheric ozone (especially on sunny, warm days with abundant precursors), reduces incoming solar radiation (temporary losses in photovoltaic output on the order of a few to several tens of percent), and degrades visibility at island and coastal airports and ports. Saharan dust and sea salt frequently co-occur, creating “heavy” aerosol episodes with complex chemistry [WHO, 2021; Querol et al., 2009].

The hydrological response is particularly intense due to Greece’s relief, which consists largely of small, steep catchments with short response times. After fire, the loss of plant cover and water repellency of the upper soil cause the first autumn storms to produce runoff peaks and sediment transport, especially in torrent-prone mountain basins (Peloponnese, Evia, Attica, Thrace). Streams and rivers receive high loads of turbidity and organic matter. Water clarity can decrease sharply relative to pre-fire conditions, “blanketing” gravel beds and microhabitats for days to a few weeks. Reservoirs and lakes become loaded with sediments and nutrients from ash, with short-term turbidity increases and a risk of eutrophication (often manifesting as phytoplankton blooms), while coastal mouths may remain turbid for 1–3 weeks depending on rainfall and currents. On flysch substrates or fine-textured soils, sediment yields are enhanced, increasing the likelihood of small, localized debris flows on slopes and torrents [Shakesby, 2011].

Greek territory includes a dense Natura 2000 network with sensitive habitats (e.g., conifer forests, semi-natural mosaics, wetlands). Shrublands and dry grasses, landscapes commonly found in rural Greece, are more flammable than mature forests with a moist understory. Habitat fragmentation occurs when a continuous natural environment is “broken” into pieces by roads or burned strips, hindering species movement. Large or repeated burns lead to biomass losses and fragmentation, with direct and indirect consequences for indicator species (raptors, forest birds, reptiles, pollinators). In the pine forests of Attica, Evia, the Peloponnese, and on Aegean islands, a moderate-intensity fire can “recycle” life—cones open, a new cohort germinates—whereas very intense or frequent fires leave extensive shrub and dry-grass cover that is slow to consolidate and more prone to fueling the next fire. In mountain ranges with Greek fir (Abies cephalonica), as well as in small island ecosystems, recovery is even slower. Among fauna, terrestrial tortoises, pollinators (e.g., wild bees), and raptors (vultures, eagles) face pressures when shrublands and grasslands burn or when roosting sites are lost. In island ecosystems with endemic plants or small bird colonies, a single large fire can have a disproportionately large impact [Arianoutsou et al., 2011].

Finally, socioeconomic consequences are especially tangible across the Mediterranean and particularly in Greece. The tourism season coincides with the fire season. Smoke, evacuations, and beach closures lead to cancellations and a freeze in bookings, while aesthetic degradation and restrictions on trails and protected zones also harm alternative tourism. In agriculture, impacts are not only direct (burned olive groves, vineyards, beekeeping losses) but also indirect: erosion and loss of fertile topsoil increase restoration costs for many years. In WUI zones, the frequent encroachment of fire into settlements brings damage to buildings and equipment, power and water outages, blockages of key

roads, and significant evacuation, insurance, and restoration costs. Overall, in years with extensive burning, the fiscal footprint is twofold: direct costs of suppression and rehabilitation, and indirect losses in tourism and agricultural production [San-Miguel-Ayanz et al., 2020; WWF, 2023].

1.3 Fire Weather Index

In wildfire science, fire danger is defined as the expected occurrence, spread and intensity of fires, as determined primarily by meteorological and fuel conditions [FAO, 1986].The FWI is the most widely used meteorological index of wildfire danger. Developed in Canada, it combines six components: three fuel-moisture codes (FFMC, DMC, DC—Fine Fuel Moisture Code, Duff Moisture Code, and Drought Code, respectively) and two fire-behavior indices (ISI – Initial Spread Index, BUI – Buildup Index). The FWI itself results from combining ISI and BUI. The final, open-ended FWI is interpreted as a measure of potential frontal fire intensity: the higher it is, the harder suppression becomes [Van Wagner, 1987; NRCan/CFS].

The Fire Weather Index (FWI) is calculated from four daily meteorological inputs measured at 12:00 local time: air temperature, relative humidity, wind speed, and 24-hour accumulated precipitation. These variables drive three fuel-moisture codes — the Fine Fuel Moisture Code (FFMC), the Duff Moisture Code (DMC), and the Drought Code (DC), which represent short-, medium-, and long-term fuel dryness, respectively. The FFMC is combined with wind to generate the Initial Spread Index (ISI), while the DMC and DC are combined to form the Buildup Index (BUI). Finally, ISI and BUI are integrated into the open-ended FWI value, which is interpreted as a measure of potential frontal fire intensity and overall fire danger [Van Wagner, 1987].

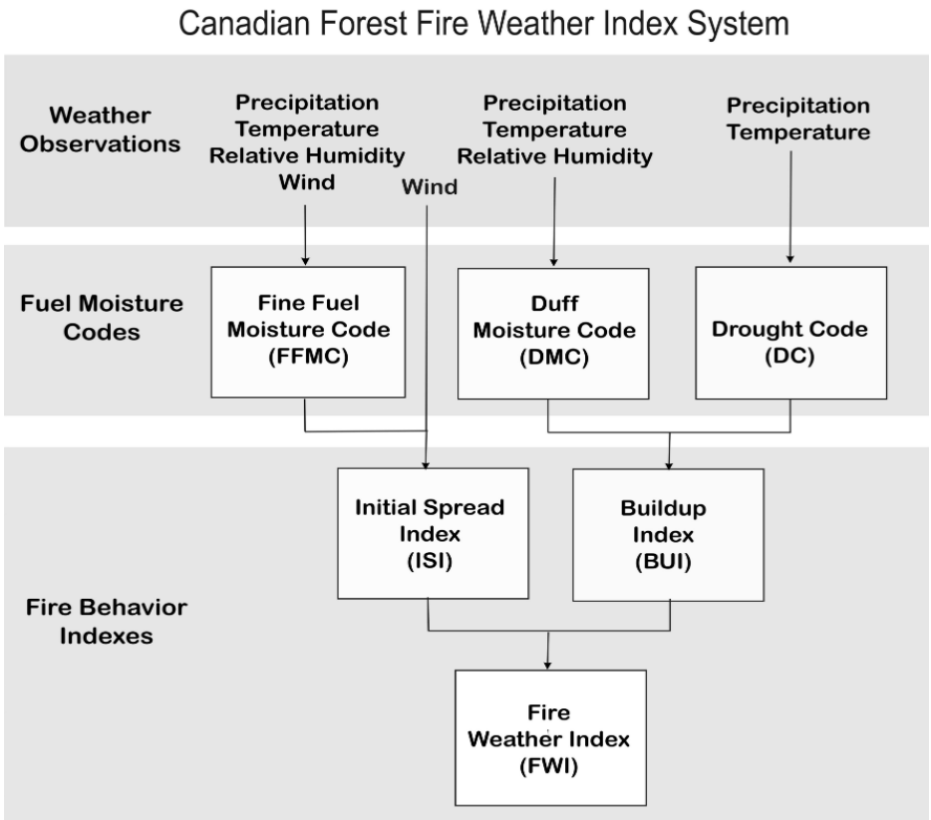

Figure 1.2. Structure of the Canadian Fire Weather Index (FWI) System, as presented in Taylor and Alexander (2006). Reproduced with permission from *International Journal of*

Wildland Fire (CSIRO Publishing). Source: Taylor, S. W., & Alexander, M. E., 2006. *Science, technology, and human factors in fire danger rating: the Canadian experience*. *International Journal of Wildland Fire*, 15(1), 121–135.

The diagram shows how daily meteorological inputs (temperature, relative humidity, wind speed, and precipitation) are used to calculate fuel-moisture codes (FFMC, DMC, DC), which are then combined into fire behavior indices (ISI, BUI) and finally integrated into the Fire Weather Index (FWI).

The Fire Weather Index (FWI) is widely applied in Europe as the main indicator of fire danger. However, the thresholds that define danger classes differ depending on scale and operational purpose. At the continental level, harmonized absolute thresholds ensure comparability between countries [CEMS–ECMWF/EFFIS/C3S], while percentile-based thresholds allow adaptation to the climatological distribution of each region [EFFIS/GWIS]. In the Mediterranean, and particularly in Greece, further adjustments have been proposed to better capture local fuel, terrain, and wind conditions.

Table 1.1 summarizes the two main European approaches to FWI thresholds: fixed harmonized values as adopted by CEMS–ECMWF/EFFIS/C3S, and percentile-based categories as used by EFFIS/GWIS.

Table 1.1. Harmonized European and percentile-based FWI thresholds.

Category	**Fixed thresholds (CEMS–ECMWF/EFFIS/C3S)**	**Percentile-based thresholds (EFFIS/GWIS)**
Very Low	< 5.2	–
Low	5.2 – 11.2	< 40th percentile
Moderate	11.2 – 21.3	40th – 60th percentile
High	21.3 – 38.0	60th – 80th percentile
Very High	38.0 – 50.0	80th – 90th percentile
Extreme	> 50.0	> 90th percentile

These dual approaches allow both harmonized interpretation across Europe and locally adapted danger classes. Fixed thresholds provide comparability for pan-European monitoring and reporting, while percentile-based thresholds ensure that the definition of “Extreme” reflects the top end of the historical FWI distribution for each country or climate zone.

In Mediterranean countries, and particularly in Greece, the FWI has proven especially effective in capturing high-risk days due to hot, dry summers and frequent winds (e.g., Etesians, downslope winds). However, local thresholds vary by region, reflecting differences in fuels and topography. Indicative values proposed in the literature for Greece and the Eastern Mediterranean are shown in Table 1.2 [Angelis, 2023].

Table 1.2. Indicative Mediterranean FWI thresholds (Greece – Eastern Mediterranean).

FWI value	Risk category
< 15	Low – Moderate
15 – 30	High
30 – 45	Very High
> 45	Extreme

Overall, Europe relies on the Canadian FWI system as its operational backbone, but adapts it through both fixed and relative thresholds to meet the diverse needs of forecasting and cross-country comparison. In Mediterranean regions, further calibration is required, and any adjustment of the index should be validated against local fire history and burned-area records before operational use [Angelis, 2023]. This highlights the importance of regional studies in ensuring the effective use of FWI for fire risk assessment.

2. Study Area

Greece lies at the south-eastern edge of Europe, at the crossroads of Europe–Asia–Africa. It extends roughly from 34.8° to 41.8° N and 19.4° to 28.3° E. Its territory combines a continental core with an exceptionally extensive coastline and pronounced insularity: official texts of the Greek National Tourism Organization report about 6,000 islands and islets, of which 227 are inhabited. Geomorphology is strongly dissected, with mountain ranges, narrow drainage basins, long shorelines, and a “mosaic” of ecosystems from montane forests to xerothermic shrublands. The climate is Mediterranean, with hot–dry summers and mild–wet winters, but with marked spatial and seasonal variability due to relief and marine influences [Kotlarski et al., 2014].

Within this setting, Thrace (Region of Eastern Macedonia & Thrace) concentrates particular features: Mediterranean conditions along the coast and continental influences farther north, which affect vegetation phenology, fuel moisture, and, consequently, the seasonality of fire risk. The Regional Unit (R.U.) of Evros, at the tip of Thrace, is emblematic of this transition (coastal–lowland–hilly/mountainous) and hosts two flagship protected areas of pan-European importance: the Dadia–Lefkimi–Soufli Forest and the Evros Delta [WWF Greece, 2021; Ramsar Secretariat, 2019].

2.1 Regional Unit of Evros

The Regional Unit of Evros is located at the edge of Thrace and constitutes the north-easternmost land part of the country. It borders Bulgaria to the north and north-west, Turkey to the east, where the Evros River forms the natural boundary, and is washed by the Thracian Sea to the south, it also includes Samothraki. Its area is approximately 4,242 km², with Alexandroupoli as the administrative capital. The Evros River is transboundary: it is referred to as Maritsa in its Bulgarian reach and Meriç in Turkey, hence all three names appear in maps and reports [ICPDR, 2021]. Its drainage basin reaches about 53,000 km² (the larger share outside Greece) and its total length is ~480 km, ending in a deltaic outflow system of high ecological value [Ramsar Secretariat, 2019].

The permanent population, according to the 2021 census of ΕΛΣΤΑΤ (Hellenic Statistic Authority), is 133,802 inhabitants. Administratively, Evros comprises five municipalities. The municipalities and their corresponding permanent population (2021) are:
• Municipality of Alexandroupoli: 71,751
• Municipality of Orestiada: 31,686
• Municipality of Didymoteicho: 16,060
• Municipality of Soufli: 11,709
• Municipality of Samothraki: 2,596

On Samothraki, Mount Saos (Feggari) reaches 1,611 m and is the highest summit in the Aegean Sea, confirming how abruptly topography can change even within the same regional unit [WWF Greece, 2021].

Evros's landforms are highly heterogeneous. There are extensive lowland and riparian areas along the main river axis and the Delta, hill chains and gentle ridges in the central and southern parts, and higher zones to the west, mainly formed by the eastern spurs of the Rhodope range. In the hydrographic network, noteworthy tributaries are the Ardas (with a substantial reach and dams in Bulgaria) and the Erythropotamos (*Luda Reka*), which drain hilly and semi-mountainous basins and flow into the Evros near Didymoteicho. The coexistence of narrow valleys and successive ridges creates natural wind corridors and micro-climatic gradients from the coast towards the interior [Xystrakis et al., 2014].

In the Regional Unit of Evros there are nine designated Natura 2000 sites, covering in total more than 220,000 ha, including both Sites of Community Importance (SCI) and Special Protection Areas (SPA). These sites are: Dadia–Soufli Forest, Treis Vryses, Vouna Evrou–Potamos Lyras–Spilaia Didymoteichou kai Kefalovounou, Evros Delta, Evros Delta and Western Branch, Parapotamio Dasos Voreiou Evrou kai Arda, Notio Dasiko Symplegma Evrou, Oreinos Evros–Koilada Dereiou, and Koilada Erythropotamou (Asvestades, Koufovouno, Vrysika). Among these, two stand out as protected areas of national and international significance. The Dadia–Lefkimi–Soufli Forest National Park extends over approximately 42,800 ha, with strictly protected cores of ~7,258–7,290 ha and a wider management zone. It is a mosaic of mixed pine and oak forests on low ridges and hills (~20–650 m), interspersed with clearings, pastures, and small cultivated "islets." The Evros Delta National Park, designated as a Ramsar Wetland, covers 9,267 ha and consists of lagoons, shallow water bodies, and reedbeds, where marine–fluvial processes intersect and large numbers of waterbirds and waders gather during migration and overwintering [Ramsar Secretariat, 2019; WWF Greece, 2021].

The inland flora belongs mainly to the zone of xerophilous deciduous oaks (*Quercus* spp.) in a mosaic with pine forests. Turkish pine (*Pinus brutia*) is extensive, while black pine (*Pinus nigra*) occurs locally at higher elevations. The landscape also includes typical sub-Mediterranean shrublands (e.g., arbutus, economically valuable shrubs, phrygana), as well as riparian belts with broadleaved species. The fauna is exceptionally rich: beyond the internationally renowned raptor avifauna—with dozens of diurnal and nocturnal species regularly recorded and the emblematic co-occurrence of three vulture species—there are mammals (e.g., wolf, roe deer), reptiles, amphibians, and lepidoptera, confirming the biogeographic uniqueness of the Dadia–Rhodope complex at the European scale. In the Delta, high concentrations of waterbirds and waders (flamingos, herons, ducks, etc.) occur, while mixed brackish–freshwater zones create ecotones of high ecological value [Skartsi et al., 2008].

As for land use and the economy, Evros combines agri-food and livestock activities (cereals, maize, cotton, livestock holdings), forest and ecotourism resources (Dadia

Information Center, observation posts), fisheries and aquaculture, and services in the main urban hubs. The cross-border character confers a special role in trade and transport. The primary road network includes the A2 (Egnatia/E90) and EO51/E85 (National Road), the railway axis Alexandroupoli–Orestiada–international, as well as the Port and the State Airport “Dimokritos” (AXD) in Alexandroupoli. In several areas, settlements and peri-urban zones and cultivated land adjoin directly shrublands or peri-urban groves, forming typical WUI (Wildland–Urban Interface) zones where the needs of agricultural production, settlement protection, and infrastructure operation intersect [EEA, 2020].

Finally, three key climatic characteristics “define” the area: the Mediterranean regime with hot, dry summers and wetter winters; the summer prevalence of etesians (meltemi) with a N–NE component over the Aegean, which can dominate throughout the day when the pressure gradient between the Balkans and the Eastern Mediterranean is large (then they overwhelm the local sea–land breeze); and the variability of the transitional seasons (spring–autumn), which affects vegetation phenology and natural soil moisture. These parameters are not only related to fire risk; they more broadly explain the seasonality of agricultural and ecotourism activities, the pressures on wetlands, and the management requirements in coastal and riparian zones [Kotlarski et al., 2014].

The zone where the large 2023 wildfire occurred extends north of Soufli and east–northeast of Dadia, up to the outskirts of Lefkimi and the neighboring settlements of Dadia, Lefkimi, Giannouli, Kotronia, connected to each other by a local provincial road network. The topography is mainly hilly, with successive ridges and narrow valleys that open toward the Evros plain, while elevations range roughly from 20 to 650 m. Land cover forms a characteristic Mediterranean mosaic: pine forests (*Pinus brutia*, locally *P. nigra*) and oak forests alternate with shrublands and herbaceous/grassland sites. Cultivated areas (mainly cereals, sunflower, cotton, depending on the year) occur in valleys, on small plateaus, and around settlements, and there are also pastures. The settlement nuclei mentioned above, together with scattered farmsteads and agricultural installations, create extensive WUI zones. Within and around the Dadia–Lefkimi–Soufli National Park there are strict protection cores and Natura 2000 areas, while seasonal streams incise the valleys and discharge toward the plain. Overall, this is a continuous forest mass on low ridges, interrupted by agricultural islets and peri-urban settlements, with a close coexistence of forest management, agricultural production, and daily mobility along the local road network [WWF Greece, 2021].

2.2 Climatological analysis of Evros

Evros lies within the transition zone between a typical Mediterranean regime (hot–dry summers, mild–wet winters) and more continental influences from the northern Balkans. At the Europe–Mediterranean scale, the area belongs to the recognised Mediterranean “hotspot”: summers tend to become warmer and drier, with an increase in days of high “fire weather” and an elongation of the fire season [IPCC, 2021].

In Evros, a typical Mediterranean seasonality prevails, with maxima in July and August and minima in January and February. The coastal zone (e.g., Alexandroupoli) exhibits a milder annual range due to marine influence and the sea–land breeze, whereas further north in the interior (e.g., Orestiada and the semi-mountainous basins) winters are appreciably colder, with more frequent frosts and a larger diurnal and annual temperature range [Hellenic National Meteorological Service, 2020].

The distribution of precipitation is distinctly winter-centred. Most of the annual rainfall (about 60%–70%) falls from October to March, while summer (June–August) is the driest

quarter. In the coastal and lowland areas, the bulk of cold-season rainfall is associated with passing low-pressure systems and fronts, whereas the inland and semi-mountainous areas are more affected by local instability in spring and autumn (short-lived but locally intense thunderstorms). The orography of the Rhodope enhances precipitation across windward–leeward sectors, creating microclimatic differences within the same regional unit. This occurs because, when moist air masses meet the slopes of the Rhodope, they are forced to ascend, cool, and condense, leading to enhanced rainfall on the windward slopes and forelands. After crossing the main crests, the air descends, warms, and dries, producing a “rain shadow” with reduced precipitation totals over the leeward basins. In winter, snowfall episodes occur mainly in the north and at higher elevations, while the first autumn storms after a dry summer can be strong, with high rainfall intensities over short durations. Overall, annual precipitation shows substantial year-to-year variability [Xystrakis et al., 2014].

In summer, the Etesians (meltemi) establish a persistent northerly–northeasterly flow over the Aegean, which extends into Thrace. When the pressure gradient between the Balkans and the Eastern Mediterranean is strong, the Etesians can override the diurnal sea and land breeze and persist throughout the 24-hour cycle. In winter, cold-air outbreaks from northerly–northeasterly sectors bring temperature drops and stronger gusts. The climatology and mechanisms of the Etesians have been described in detail in the literature [Tyrlis & Lelieveld, 2013, JAS], confirming the frequency and intensity of the summer northerly–northeasterly flow over the eastern Mediterranean.

Summer dryness and winds reduce the moisture of fine fuels (FFMC), while spring rainfall deficits affect deeper moisture (DMC/DC). In years with persistent heat and precipitation deficits in the Mediterranean, episodes of very high FWI increase, as does the duration of the “window” of favourable conditions for spread. The European State of the Climate 2023 (C3S/EUMETSAT) and the assessments by JRC (Joint Research Centre) and EFFIS (European Forest Fire Information System) record 2023 as a year with widespread warm/dry episodes and very high fire danger.

The hilly, semi-mountainous terrain between Dadia–Lefkimi, with successive ridges and narrow valleys opening towards the plain and the coastal sector, creates flow corridors for the northerly–northeasterly wind in summer. Shrublands and pine forests (xerophilous vegetation) dry out quickly, while the agricultural mosaics around settlements add peripheral transmission zones. This “mix” of topography–wind–fuels explains why, on days with high FWI, spread can become rapid [Xystrakis et al., 2014].

2.3 The 2023 Evros wildfire

The Evros wildfire (Alexandroupoli–Dadia, August 2023) was recorded as the largest single forest fire in the European Union since comparable records exist, according to the European Commission. In terms of size, the Copernicus EMS technical report (EMSN166) estimates the burned area at approximately 93,880 ha, while the WWF Greece assessment places it at 94,250 ha, the small differences arise from methodology and the temporal bounds of the mapping. In terms of duration, WWF reports 16 days for the main front—19 August to 3 September—whereas Copernicus Rapid Mapping (EMSR686) considers the event extinguished on 08/09/2023, i.e., roughly 20 days from the ignition on 19/08/2023 (04:49 local).

What follows is a chronological (day-by-day) description of spread and operational picture, based on EMSR686 products (Delineation & Monitoring) and the findings of the EMSN166 technical report.

20/08/2023 08:27 UTC – First Estimate (FEP)
First estimate with Sentinel-3: 5,559.7 ha burned and 3 recorded active hotspots. The depiction is coarse (300 m) and serves as a quick snapshot of the situation.

20/08/2023 08:56 UTC – Delineation (DEL)
More accurate mapping with Sentinel-2: 5,040.8 ha burned, 25 active hotspots, and 7.6 km of active fire fronts. Active hotspots appear scattered along the mapped front within the AOI (Area Of Interest).

21/08/2023 09:25 UTC – Monitoring 01
8,529.4 ha burned, 34 active hotspots, 7.0 km of active fronts. The increase relative to the previous day reflects front expansion; hotspots remain distributed along the perimeter.

23/08/2023 09:19 UTC – Monitoring 02
Explosive increase: 67,692.8 ha burned, 40 active hotspots, 13.6 km of active fronts. The large change reflects rapid spread between 21–23/08.

24/08/2023 08:44 UTC – Monitoring 03
73,526.5 ha burned, 81 active hotspots, 0.9 km of active fronts. The number of hotspots doubles relative to 23/08, even though the “length” of active fronts decreases (likely fragmented activity along the perimeter).

25/08/2023 09:18 UTC – Monitoring 04
75,668.2 ha burned, 63 active hotspots, 2.8 km of active fronts. The total area continues to increase, with scattered hotspots along the mapped perimeter.

26/08/2023 09:04 UTC – Monitoring 05
Burned area 77,068.2 ha, 120 active hotspots, 2.6 km of active fire fronts. The burned area increases marginally relative to 25/08, while the number of hotspots jumps (63 → 120), indicating extensive perimeter activity/re-ignitions; the total length of active fronts decreases slightly (2.8 → 2.6 km).

28/08/2023 09:28 UTC – Monitoring 06
80,873.0 ha burned, 104 active hotspots, 0.6 km of active fronts. A very large number of active points (likely smouldering/re-ignitions) compared with the near-zero front length.

29/08/2023 09:03 UTC – Monitoring 07
81,260.7 ha burned, 40 active hotspots. The growth of the burned area slows, while hotspots remain scattered across the fire footprint.

02/09/2023 08:31 UTC – Monitoring 08
93,511.0 ha burned, 7 active hotspots. The total burned area approaches the final value, active hotspots have decreased substantially.

03/09/2023 09:16 UTC – Monitoring 09
Final Rapid Mapping depiction: 93,880.8 ha burned with 2 active hotspots.

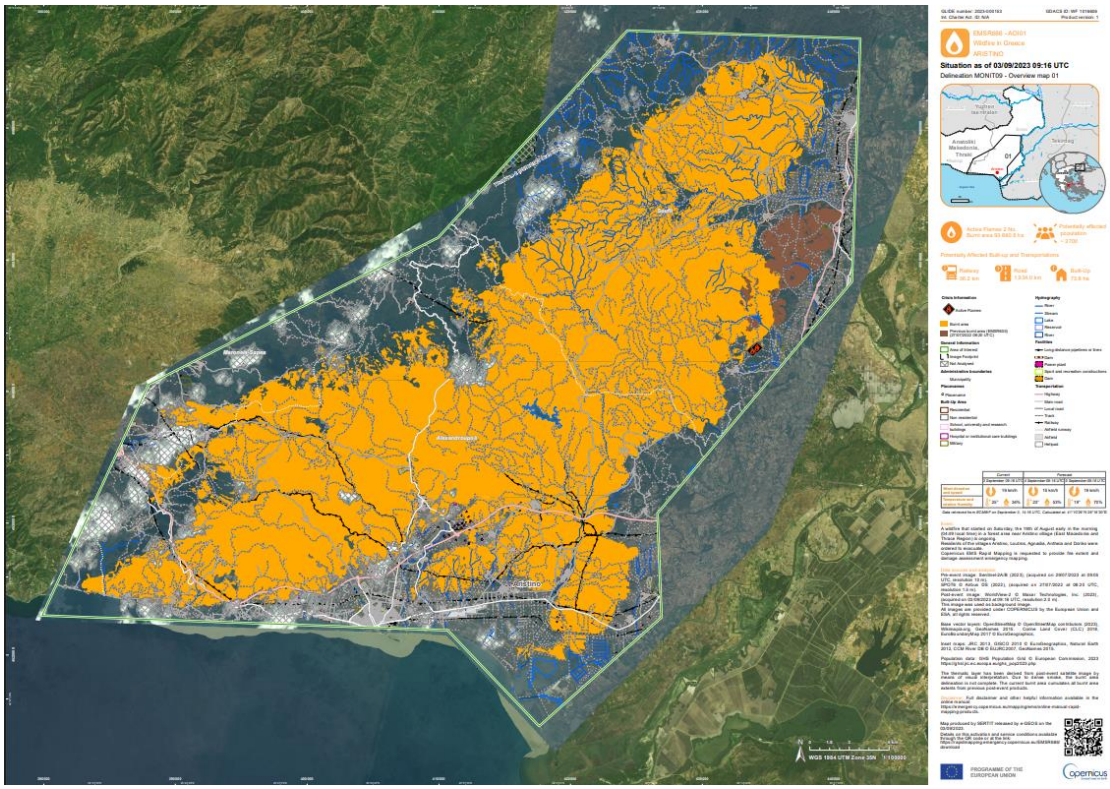

Figure 2.1. Burned area delineation map of the Evros wildfire, produced by Copernicus EMS Rapid Mapping on 03 September 2023 (Activation EMSR686, AOI01). Reproduced under CC BY 4.0 license. Source: European Union, Copernicus Emergency Management Service.

The wildfire ignited at dawn on 19 August 2023 (04:49 local) in the Aristino area (P.E. Evros). The first mapping on 20/08 had already recorded thousands of hectares burned and a few active hotspots, while the analytical product of the same day confirmed a burned area of about 5,000 ha. Within 24 hours, on 21/08, the burned area rose to 8,529 ha with 34 active hotspots.

The 23/08 jump is a turning point: the burned area surges to 67,693 ha and the active front reaches 13.6 km. The next day (24/08) the area increases further (73,527 ha) with 81 active hotspots, while on 25/08 it exceeds 75,668 ha. This dynamic continues through 28–29/08, when the burned area reaches 80.9–81.3 thousand ha, with a very large number of active points on 28/08 (104).

In early September the fire recedes: on 02/09 93,511 ha and 7 active hotspots are recorded, and on 03/09 the final Rapid Mapping depiction closes at 93,881 ha with 2 active hotspots. According to the EMSN166 technical report, the activation closed on 08/09/2023, at which point the incident was considered extinguished.

The wildfire's consequences are particularly severe and can remain perceptible for a long period. In the damage-grading product (P07, dNBR method), 92,321 ha of burned land were inventoried within the AOI, of which 4,587 ha "Destroyed," 34,843 ha "High damage" (≈36% of the total), 22,154 ha "Moderate," and 30,738 ha "Negligible–Slight" (Copernicus EMS, 2023a). That is, the largest share of the burned area is classified as high or very high burn severity, which explains the temporary loss of high-quality plant cover and the soil's high susceptibility to erosion during the first intense rains. In Mediterranean

landforms like Thrace, the literature shows that the first storms after fire are often linked to runoff peaks and pulses of sediment and turbidity in streams, reservoirs, and estuaries, before vegetation “knits” back together [Shakesby & Doerr, 2006].

In the atmosphere, CAMS data recorded strong smoke emissions and plume transport from late August, with the cloud affecting the eastern Mediterranean and the Balkans; CAMS also notes that Greece’s fire emissions in 2023 ranked among the three highest of the past two decades (behind 2007 and 2021). On such “smoke days,” increases in $PM_{2.5}$/PM_{10} and tropospheric ozone are expected downwind of sources, as shown in CAMS operational bulletins and analyses for the August 2023 episode. Beyond health, smoke reduces incoming solar radiation (temporary losses in PV performance) and visibility at airports/ports, while dry and wet deposition of ash/soot affects surfaces, open water intakes, and crops [Andreae, 2019].

Human losses and operational consequences were severe. During the multi-day evolution of the wildfire, 20 deaths were recorded, while in Alexandroupoli evacuations took place, notably the transfer of 65 patients (including newborns) from the University Hospital to a ship that served as a temporary medical unit in the port. The smoke cloud affected a broad swath of northern Greece for days, with repeated civil-protection advisories and disruptions to transport and operations [WWF Greece, 2023; Civil Protection Greece, 2023].

At the European response level, the rescEU mechanism was activated at a record scale: the ERCC coordinated 11 fixed-wing aircraft and 1 helicopter from the EU pool, as well as ground teams from many Member States, with continuous asset rotations as suppression progressed. In parallel, JRC/EFFIS emphasized that the incident occurred in a year of exceptionally high wildfire burden for Europe and was associated with very high–extreme fire-danger conditions. The operational experience, from Copernicus EMS rapid re-mapping to cross-border reinforcement, makes the Evros case a reference point for preparedness planning, management, and post-fire monitoring in the Mediterranean.

3. Datasets and Methodology

3.1 Datasets

In order to carry out the present analysis, it was necessary to use climate datasets that combine global coverage, long temporal span, and reliable quality. For this purpose, two complementary sources were selected. The first is the ERA5 reanalysis dataset, produced within the Copernicus Climate Change Service, which offers detailed historical climate information at high temporal and spatial resolution. The second is the ISIMIP3a dataset, which provides bias-adjusted climate input data designed for impact studies and includes both observed (obsclim) and counterfactual (counterclim) scenarios. Together, these datasets ensure that the study is based on robust and internationally recognized climate data, while also enabling the assessment of anthropogenic climate influences.

3.1.1 ERA5 - Copernicus Climate Data Store

https://cds.climate.copernicus.eu/datasets/reanalysis-era5-single-levels?tab=download

The Copernicus Programme is the European Union’s tool for Earth observation initiative, created to provide free, reliable, and consistent information about the environment. It is coordinated by the European Commission and implemented in partnership with

institutions such as the European Space Agency (ESA), EUMETSAT, and the European Centre for Medium-Range Weather Forecasts (ECMWF). Among its six thematic services, the Copernicus Climate Change Service (C3S) plays a central role in delivering climate datasets that describe past, present, and future conditions. Within this framework, the ERA5 reanalysis, developed by ECMWF, constitutes the fifth generation of global atmospheric reanalyses and is widely regarded as one of the most reliable climate data products available today.

ERA5 provides data at an hourly temporal resolution and covers the vertical structure of the atmosphere with 137 levels, extending from the surface to approximately 80 km (~0.01 hPa). This high resolution allows detailed monitoring of both near-surface and atmospheric processes relevant for applications such as wildfire modelling, climate trend detection, and energy flux analysis. Spatially, ERA5 is produced on a reduced Gaussian grid with a horizontal resolution of ~31 km, which is appropriate for large-scale studies but less suitable for capturing fine-scale processes in regions with complex topography. For this reason, the ERA5-Land dataset, at ~9 km resolution, has been developed to offer more accurate representation over land and mountainous regions.

ERA5 provides a broad set of variables, including both single-level fields (e.g., 2 m temperature, 10 m wind speed, precipitation, soil moisture) and multi-level atmospheric variables (temperature, humidity, wind components, vertical velocity, geopotential). This versatility makes ERA5 suitable for a wide range of environmental and climate applications.

The production of ERA5 relies on the Integrated Forecasting System (IFS) Cycle 41r2, using a 4D-Var assimilation scheme with 12-hour windows. More than 10 million observations per day are assimilated, drawing on over 80 satellite missions in addition to radiosondes, buoys, aircraft reports, and surface stations. The quality of ERA5 improves significantly after 1979, when global satellite coverage became continuous. Earlier decades, however, relied on far fewer observations (~17,000 per day in 1940 compared to ~25 million in 2022), leading to greater uncertainty, especially in regions such as Southern Europe.

ERA5 data are provided through the Copernicus Climate Data Store (CDS) and can be accessed either from the web platform or through the CDS API. The dataset is updated every day, with a typical delay of about five days, which allows almost real-time use for both past records and recent conditions. In total, ERA5 includes more than 240 variables that describe the surface, the atmosphere, and the subsurface. Examples are 2 m air temperature, total precipitation, solar radiation, and soil temperature and moisture at different depths. It also provides pressure-level fields such as temperature, humidity, wind, and geopotential height, as well as derived variables like convective available potential energy (CAPE), evaporation, vertical velocity, cloud cover, and energy fluxes.

One of the main advantages of ERA5 is the ability to capture long-term temperature and precipitation trends with good accuracy. The dataset also represents winds and extreme events such as heatwaves in a reliable way, which makes it useful for hazard studies and wildfire analysis. In addition, ERA5 provides uncertainty estimates through a 10-member ensemble, so that users can evaluate variability in the results. Finally, the continuous daily coverage and the stable production process make it a robust source for seasonal and year-to-year studies.

Some limitations, however, also exist. Data from the early decades (1940s–1970s) are less reliable because of fewer observations and stronger reliance on the model. Studies

such as Soci et al. (2024) have shown discontinuities in variables like temperature and humidity before 1978. ERA5 is also known to underestimate some extremes, for example the diurnal temperature range, minimum temperatures, or the intensity and duration of heatwaves, especially in Mediterranean and arid regions. The horizontal resolution of about 31 km cannot fully describe local terrain features, which adds uncertainty in processes such as soil moisture and evapotranspiration. For such cases, ERA5-Land is often a better choice. Finally, regional uncertainties remain in areas with limited observations, such as the Balkans during the mid-20th century, where the model component has a stronger influence than actual measurements.

ERA5 is considered a cornerstone dataset for climate research, combining state-of-the-art assimilation methods, a vast observational basis, and consistent updates. Its strengths make it invaluable for climate-sensitive applications such as wildfire risk assessment, agriculture, and hydrology. At the same time, careful consideration of its limitations—particularly in the early years and in complex terrain—is essential. Complementary use of higher-resolution products (e.g., ERA5-Land) and local observational datasets can help mitigate these uncertainties and enhance the robustness of analyses.

3.1.2 ISIMIP3a – GSWP3-W5E5 Forcings

https://data.isimip.org/search/tree/ISIMIP3a/InputData/climate/

The Inter-Sectoral Impact Model Intercomparison Project (ISIMIP) provides a coordinated framework for climate impact assessments across different sectors such as agriculture, water resources, ecosystems, human health and natural hazards. The ISIMIP3a dataset is a key part of this effort, designed to supply bias-adjusted climate input data for multi-model impact simulations. It integrates observational and model-based data to provide a consistent foundation for quantifying the impacts of both historical climate variability and anthropogenic climate change.

The ISIMIP3a input data are built upon the GSWP3-W5E5 dataset, which combines the Global Soil Wetness Project Phase 3 (GSWP3) historical meteorological forcing with the W5E5 dataset, a merged observational product that ensures global consistency. For each variable, ISIMIP3a provides two complementary climate scenarios:

- obsclim, which represents climate as observed, including both natural and anthropogenic forcings.
- counterclim, which provides a counterfactual scenario where anthropogenic climate change signals are removed, allowing for attribution studies.

The ISIMIP3a dataset provides daily global climate data at a resolution of 0.5° × 0.5° (~55 km), covering a wide range of essential variables such as near-surface air temperature (tasmax, tasmin), precipitation, wind speed, humidity, and radiation. The dataset has been structured to ensure full compatibility across different impact models, which allows comparative and multi-sectoral assessments in fields such as agriculture, hydrology, and ecosystem research.

One of the main advantages of ISIMIP3a is that it offers bias-adjusted data, thereby reducing inconsistencies between climate model outputs and observational records. It also provides globally consistent coverage at daily temporal resolution, making it suitable for both long-term studies and cross-sectoral analyses. A key feature of the dataset is the inclusion of two scenarios: obsclim, which incorporates anthropogenic influence, and counterclim, which represents a climate without human-induced forcing. This dual structure enables attribution studies that distinguish anthropogenic signals from natural

variability. Furthermore, ISIMIP3a is designed to be multi-model compatible, ensuring harmonized inputs across different impact studies, while its open availability through the ISIMIP data portal promotes transparency and reproducibility in research.

At the same time, the dataset presents some limitations and uncertainties. Its spatial resolution of approximately 55 km may not be adequate for fine-scale regional applications, especially in areas with complex topography or strong local gradients. The bias-adjustment methods, although useful for improving consistency, can sometimes introduce artifacts or reduce the variability of extremes. In addition, the dataset depends on input forcings such as GSWP3 and W5E5, meaning that uncertainties from these sources are directly propagated into ISIMIP3a. The counterclim scenario also represents a simplified version of a world without anthropogenic forcing and therefore may not fully capture certain complex feedbacks. Finally, the lack of sub-daily processes limits the representation of short-term events, which can be critical for extreme weather and event-based attribution studies.

Overall, ISIMIP3a constitutes a robust and harmonized climate forcing dataset that is widely used for assessing the impacts of climate change on extreme events. By enabling direct comparisons between the observed world and a hypothetical climate without human-induced warming, it provides a solid basis for attribution analyses and supports a deeper understanding of how climate change influences wildfire risk.

3.1.2.1 Obsclim (factual climate scenario)

The obsclim dataset represents the factual world, meaning the observed climate that includes both natural climate variability and the anthropogenic climate change signal. It is constructed by bias-adjusting reanalysis and observational datasets to a consistent daily grid at 0.5° resolution, ensuring spatial and temporal homogeneity across variables.

In practice, obsclim is treated as the reference scenario because it reflects the climate conditions as they have actually occurred. It provides a realistic basis for simulating impacts and for validating attribution analyses. In this study, obsclim data are used to represent the climate conditions under which the extreme fire season of 2023 unfolded.

The dataset has several strengths, as it is closely aligned with observations and therefore suitable for impact studies at both regional and global scales. It also preserves realistic day-to-day variability together with long-term climate trends, which makes it reliable for assessing changes over time. At the same time, some limitations need to be acknowledged. The spatial resolution of 0.5° tends to smooth fine-scale processes and can lead to an underestimation of extremes in areas with complex topography. In addition, certain variables still present biases even after the bias-adjustment procedures, especially in regions where observational data are scarce.

3.1.2.2 Counterclim (counterfactual climate scenario)

The counterclim dataset represents a counterfactual world in which the anthropogenic climate change signal has been removed. This is achieved by estimating the anthropogenic warming trend from climate model ensembles and subtracting it from the factual climate (obsclim), while preserving the same daily weather sequence. In this way, natural variability is maintained, but the long-term warming trend is absent.

The counterclim scenario allows researchers to explore “what would have happened” without human-induced climate change. Comparing counterclim to obsclim provides an estimate of how anthropogenic forcing has influenced the frequency and intensity of extreme events, such as wildfires.

An important strength of the dataset is that it enables attribution studies by isolating the human-induced contribution, while maintaining the same natural variability as the obsclim scenario and thus ensuring comparability between the two. However, there are also some limitations. The removal of the anthropogenic signal introduces methodological uncertainty, as it depends on the choice of climate models and the detrending method applied. In addition, this dataset does not represent an independent observational record but rather a model-derived construct. Finally, the spatial resolution of 0.5° remains the same as in obsclim, which restricts detailed interpretation at the local scale.

3.2 Methodology

The methodological framework was designed to evaluate the influence of climate change on the 2023 Evros wildfire, through the analysis of relevant meteorological conditions and the application of attribution techniques. As an external reference point, the *State of Wildfires 2023–2024* study for the Evros fire was selected, in order to test whether the trends derived from the analysis agree with an independent source [Jones et al., 2024].

In the first stage, hourly ERA5 reanalysis fields (single levels) were retrieved from the Copernicus Data Store for an initially broad area that safely covered the entire burned extent. The choice of a wide window was intentional, so as to ensure that potential spatial inconsistencies would not affect mean temporal trends. For the initial comparison with the *State of Wildfires*, two temporal foci were used: (a) exclusively the fire days (19/8–3/9/2023) and (b) the summer period June–September 2023.

The variables retrieved and processed were: 2 m air temperature (T2m) in Kelvin (converted to °C where required), 10 m wind speed derived from u10, v10 components (m s^{-1}), soil temperature at layer 1: 0–7 cm (K → °C), volumetric soil water at 0–7 cm, 7–28 cm, 28–100 cm (m^3 m^{-3}), 2 m dewpoint temperature (K → °C), and precipitation (mm).

The hourly fields were converted to daily mean values (24 values/day) to facilitate comparison with summary plots and reduce sub-hourly noise. At all steps, a spatial average was applied over the selected polygon of interest (AOI). In this way, daily mean time series were produced for the above variables, both for the 19/8–3/9/2023 window and for June–September (JAS) 2023, and qualitatively compared with the corresponding *State of Wildfires* plots (temperature, wind, soil/moisture conditions).

Subsequently, a small sensitivity analysis was carried out to select the “optimal” spatial window representing the burned area, by testing different domains in the wider incident region and evaluating potential deviations in daily mean values (especially for August–September 2023 and for the same variables). The final ERA5 AOI adopted was a rectangular window with N: 41.14, S: 40.86, W: 25.72, E: 26.18, consistent with the latest Copernicus EMS Rapid Mapping burned area delineation.

For the computation of the Fire Weather Index (FWI), midday meteorological values and the cumulative 24 h precipitation are required. The analysis adopted values at 12:00 local time (EEST, UTC+2) for air temperature, relative humidity, and 10 m wind, while precipitation was calculated as a daily sum.

- Air temperature (T, °C) at 12:00 LT: $T_{\circ C}=T_K-273.15$.
- Relative humidity (RH, %) at 12:00 LT from air temperature (T) and dewpoint (Td), in °C, using the Magnus formula:

$$e_s(T) = 6.112 \exp\left(\frac{17.62T}{243.12+T}\right),\ e(T_d) = 6.112 \exp\left(\frac{17.62T_d}{243.12+T_d}\right),\ RH = 100 \times \frac{e(T_d)}{e_s(T)}$$

- 10 m wind (U10) at 12:00 LT: wind speed from u10, v10: $U_{10}=\sqrt{\left(u_{10}^2 \quad + v_{10}^2\right)}$ in m s^{-1} and converted to km h^{-1} (unit consistent with the FWI definition).
- Precipitation (Pr24h, mm day^{-1}): daily sum from hourly values 00:00–24:00 LT.

For 12:00 LT in ERA5, the corresponding time was set to 10:00 UTC (EEST = UTC+2). All the above parameters were computed at the grid-cell level, then spatially averaged over the AOI.

FWI was computed daily for the entire 1940–2024 period with inputs T (°C, 12:00 LT), RH (%, 12:00 LT), U10 (km h^{-1}, 12:00 LT), Pr24h (mm). Implementation was carried out in MATLAB (standard operational sequence of the FWI system). Subsequently, the following were produced: histogram of all daily FWI values (JAS(Jouly-August-Septeember), 1940–2024) with summary statistics min, max, mean, 25th percentile (P25), 75th percentile (P75), 90th percentile (P90), 95th percentile (P95), annual exceedances: time series with days/year for FWI > P90 and FWI > P95 (where thresholds derive from the JAS climate distribution), JAS climate curves: for each calendar day of July–September, min, max, mean, P25, P75 were computed along with a 2023 curve (for direct comparison of 2023 against the 1940–2024 climate context), comparison of two 30-year periods (1961–1990 vs 1991–2020) with identical bins (bin width = 5), to test whether the distribution shifts towards higher values in the later period.

For visualization, all plots (including climate curves) were created in Python, while histograms of distributions and annual exceedance time series were prepared in Microsoft Excel.

As a second major step, the daily climate forcings ISIMIP3a (GSWP3–W5E5) were used for the scenarios obsclim (with anthropogenic influence) and counterclim (without anthropogenic influence), at 0.5° resolution. For grid compatibility, a tailored AOI was set with N: 41.34, S: 40.84, W: 25.70, E: 26.20. The four FWI inputs (T, RH, U10, R24h) were directly available/exportable from the forcing set (or computable with the same steps, where required), without the need for further spatial resampling, since the 0.5° grid adequately covered the AOI with cells consistent with the model scale. The analysis period for the scenarios was 1941–2019.

Using exactly the same approach, daily FWI was computed (MATLAB) and the following were produced: histograms of FWI distributions and a distribution-difference plot (obsclim − counterclim) with identical bins (bin width = 5), to capture potential shifts towards higher values in obsclim, annual exceedances >P90 and >P95 (days/year) per scenario, JAS climate curves per scenario (5 curves: min, max, mean, P25, P75, without a 2023 curve).

The direct comparison of the two scenarios focused on the distribution of values (dual-plot histogram) and quantification of bin-wise differences, aiming to determine whether obsclim shifts the frequency towards medium and high bins compared with counterclim.

Finally, for 19/8–3/9/2023, a percentile/quantile mapping was performed to estimate how “rare” the same physical FWI values would be in a climate without anthropogenic influence. Specifically:

Each daily FWI value (ERA5) was placed within the 1940–2024 climate distribution and its percentile extracted (rank/N). In obsclim (1941–2019), the equivalent FWI value was identified at the same percentile (quantile mapping). This value was then mapped onto the

counterclim distribution (1941–2019), yielding the percentile in the hypothetical climate without anthropogenic forcing.

FWI calculation was implemented in MATLAB. Preprocessing and most visualizations were carried out in Python (notably: xarray, pandas, numpy, matplotlib). Histograms of distributions and annual exceedance time series were prepared in Microsoft Excel, with cross-checks of numerical results against Python/MATLAB computations. The conversion from hourly to daily values was made by simple averaging (for T, u10/v10, soil T, soil moisture) and daily accumulation for precipitation. For FWI inputs, the system's units were strictly followed: T (°C), RH (%), U10 (km h^{-1}), Pr24h (mm) at 12:00 local time (with UTC conversion where required). In all analyses, a spatial average over the AOI was used, a practice that reduces the impact of individual grid cells and highlights the overall regional signal.

4. Results and Discussion

4.1 Comparison of meteorological conditions with the State of Wildfires 2023–2024 study

Using the State of Wildfires 2023–2024 study for the Evros wildfire as a reference point, a comparison is made between the meteorological conditions during the event and the results of the present analysis, based on ERA5 reanalysis data (Copernicus Climate Change Service, ECMWF) [Jones et al., 2024].

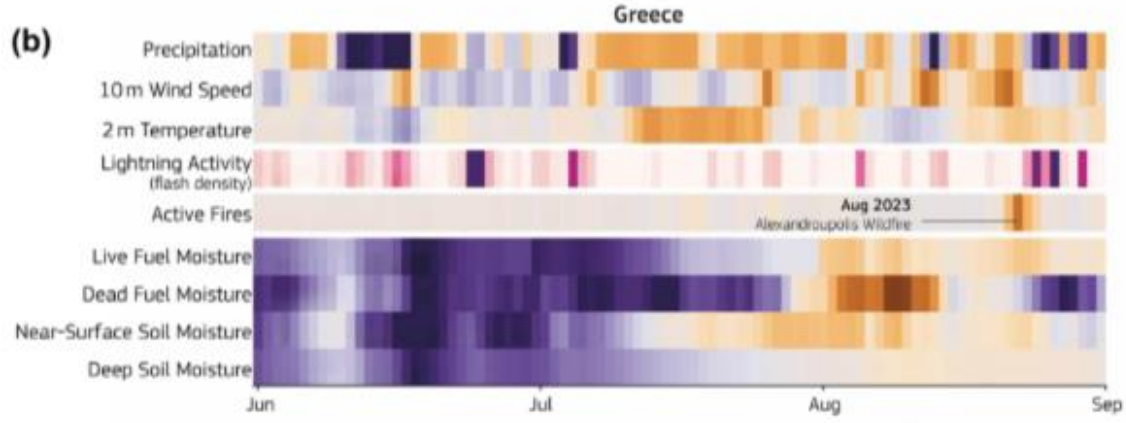

Figure 4.1. Meteorological conditions in the area of interest during summer 2023, as presented in the State of Wildfires 2023–2024. Reproduced under CC BY 4.0 license. Source: European Commission, Joint Research Centre (JRC), State of Wildfires in Europe, Middle East and North Africa 2023–2024, Earth System Science Data (Copernicus Publications).

For comparison purposes, the plot with the meteorological conditions as published in the State of Wildfires 2023–2024 is included, providing a summary framework for summer 2023 in the area of interest. The main trends emerging from the figure (increased temperatures, temporary strengthening of winds before the episode, gradual decline in soil moisture) are generally consistent with the results we calculated from ERA5 for Evros, with minor deviations in the timing of local peaks [Jones et al., 2024]. Subsequently, the plots created with ERA5 data are presented, in order to document quantitatively both the distribution of the indicators and the shift in FWI values during the wildfire days. Hourly data (24 values per day) were used, from which daily mean values were derived and are shown in the plots. The coordinates used cover the area of all active fronts (N: 41.35°, W:

25.50°, E: 26.50°, S: 40.80°). The analysis focuses on three key parameters: temperature, wind, and soil conditions.

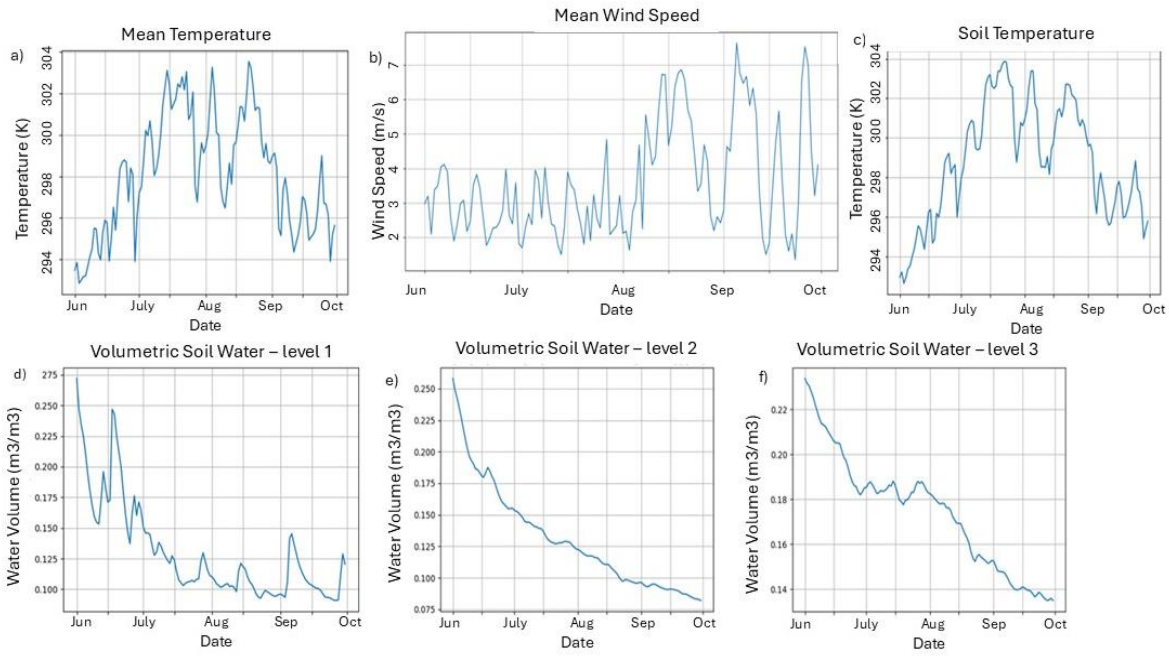

Figure 4.2. Climate Conditions from ERA5 in Evros region (July-September 2023), (a) Temperature 2m, (b) Wind Speed 10 m, (c) Soil Temperature, (d) Volumetric Soil Water – level 1, (e) Volumetric Soil Water – level 2, (f) Volumetric Soil Water – level 3.

The plots are used for comparison with the State of Wildfires 2023–2024, highlighting the agreement in the main trends and the timing of the peaks.

In the article, a relatively stable temperature behavior is observed in June, with the exception of a sharp drop in the middle of the month. In the ERA5 data this pattern is confirmed, although a more pronounced drop appears at the end of June. In July, both sources show persistently high temperatures with a gradual decrease towards the end of the month. In August, both depictions converge in showing an increase in temperature peaking around August 21, that is, two days after the wildfire outbreak. This is followed by a gradual decline until early September, a fact linked to the retreat of the active fronts.

Wind speed is presented as low in June and July, with only minor fluctuations, both in the article and in ERA5 data. The picture changes in August, where wind strengthening is observed in the days before the wildfire outbreak, a feature confirmed by both sources. After August 20, a gradual decline follows, with no strong new peaks until the end of the episode.

Soil temperature increases until August and remains high during the first days of the wildfire, before gradually decreasing. Regarding soil moisture, ERA5 data show a decline in the upper layers during July–August, consistent with the drying also shown in the article plot. In the deeper layers (deep soil moisture) the decrease is slower, with relative stability in July before a sharp drop by mid-August. In both depictions, an overall marked decrease in soil moisture is evident by late summer, a factor that favored wildfire development and spread.

The comparison shows good agreement between ERA5 data and the plots of the State of Wildfires 2023–2024, which are likewise based on ERA5 fields. The main trends in temperature, wind, and soil moisture parameters are consistent, with minor deviations in

the exact timing of local changes. Overall, a period of high temperatures, strengthened winds before the wildfire, and reduced soil moisture is documented, conditions which combined confirm the favorable fire weather framework of August 2023.

4.2 Sensitivity analysis of the burned area domain

As shown in Chapter 2.3, the wildfire evolved on a daily basis with the burned area increasing from day to day, leaving, as expected, an irregular footprint. For the purposes of this study and for data extraction from the Copernicus Climate Data Store, it is necessary to define a rectangular domain. Based on final burned area estimates from the Copernicus EMS rapid mapping service, this study assumes that the rectangle representing the extent of this event has the following coordinates: N: 41.14°, S: 40.86°, W: 25.72°, E: 26.18°.

To ensure that even in the case of a domain selection error the deviations in daily mean values of different parameters remain small, a comparison was made across different coordinate sets of burned area domains. Specifically, five different regions/domains were examined:

- Region 1: N: 41.14°, S: 40.86°, W: 25.72°, E: 26.18°, the main study area derived from the final burned area footprint
- Region 2: N: 41.04°, S: 40.90°, W: 25.84°, E: 26.07°, smaller than the main area, restricted towards the center of the burned area
- Region 3: N: 41.00°, S: 40.90°, W: 25.78°, E: 26.01°, an even smaller domain at the core of the burned area
- Region 4: N: 41.31°, S: 40.86°, W: 25.46°, E: 26.34°, extending from the city of Komotini in the west to the border with Turkey in the east
- Region 5: N: 41.50°, S: 40.86°, W: 24.93°, E: 26.67°, extending from the city of Xanthi in the west to the Hamidiye province of Turkey in the east

Finally, the parameters studied were 2 m air temperature, wind speed, precipitation, soil temperature at level 1 (0–7 cm), volumetric soil water content at level 1 (0–7 cm), volumetric soil water content at level 2 (7–28 cm), and volumetric soil water content at level 3 (28–100 cm).

The comparisons were made for July and August 2023, the months during which the wildfire occurred. The plots presented for the parameters 2 m air temperature, wind speed, precipitation, and soil temperature at level 1 correspond, from left to right, to Region 1, Region 2, Region 3, Region 4, and Region 5. For the parameters volumetric soil water content at level 1, volumetric soil water content at level 2, and volumetric soil water content at level 3, the plots correspond to the regions (in order): Region 1, Region 2, Region 3, and Region 4.

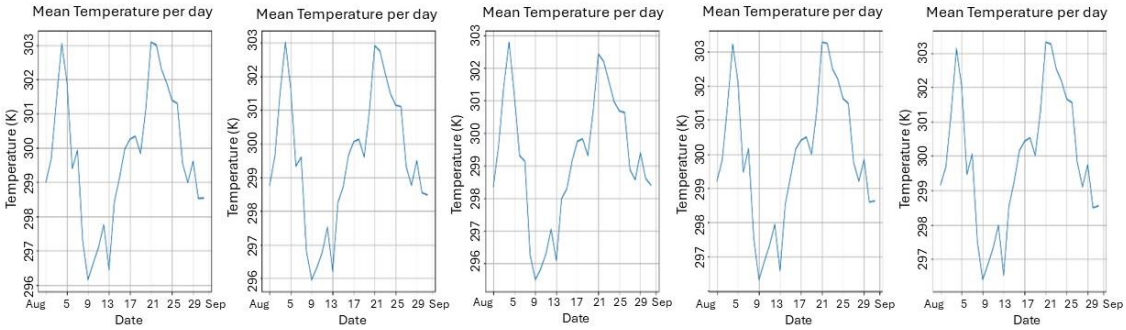

Figure 4.3. Mean Daily Temperature for Regions 1, 2, 3, 4 and 5, for the August-September period.

Across all five plots of daily mean temperature (K) for August 2023, essentially the same signal appears: a mild start (~299–300 K), a pronounced warm surge on 4–6 Aug (~302–303 K), an abrupt cool spell on 8–10 Aug (down to ~296–297 K), a gradual rebound on 12–18 Aug (~299–301 K), and a second/stronger peak on 21–23 Aug (~302–303 K), followed by a decline toward the end of the month (29 Aug–1 Sep ~298–300 K). Differences among the five series are mainly limited to small phase shifts (0–1 day) and amplitude of up to ~0.5–1.0 K—especially in mid-month and after 24 Aug. The intra-monthly range is about 6–7 K. Overall, all panels converge on the timing of the two warm episodes and the cool break on 8–10 Aug, indicating a common regional control on temperature rather than local noise.

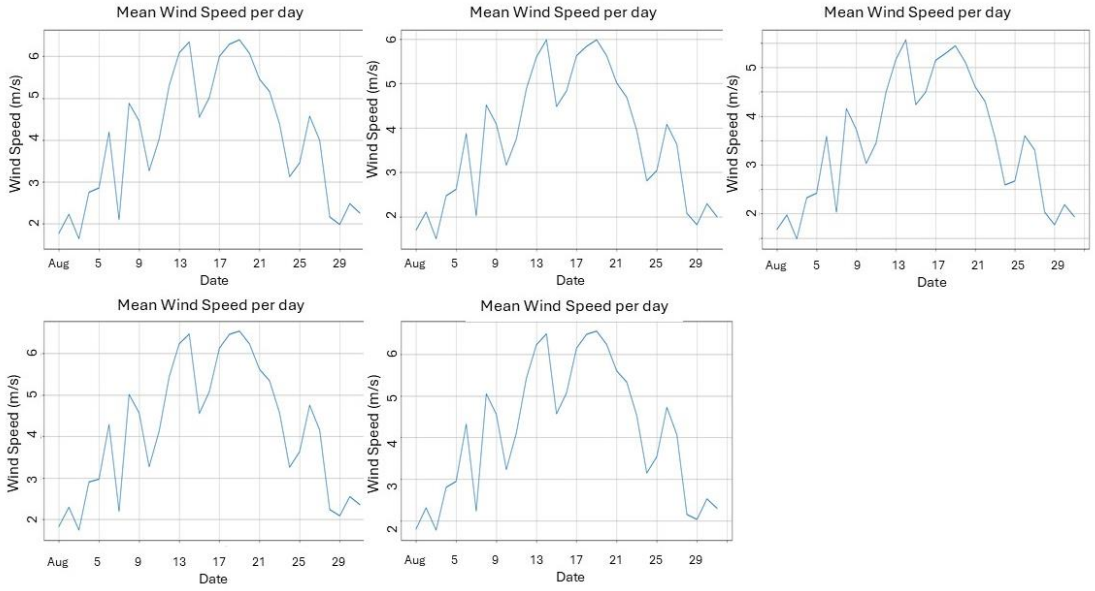

Figure 4.4. Mean Wind Speed per Day for Regions 1, 2, 3, 4 and 5, for the August-September period.

Across all five plots of mean daily wind speed (m/s) for August 2023, the evolution is essentially the same: a weak start (~1–2 m/s), a gradual strengthening through the first half of the month with brief oscillations, and two main peaks—around 14–16 Aug and 20–23 Aug—reaching roughly 5.5–6 m/s. After 24–25 Aug there is a clear weakening toward 2–3 m/s, with a small temporary rebound at the very end of the month (30–31 Aug). Differences between the five series are limited to minor phase shifts (up to ~1 day) and amplitude variations of about 0.5–1 m/s, especially near the second peak. Overall, the timing of the strengthening/weakening is consistent across plots.

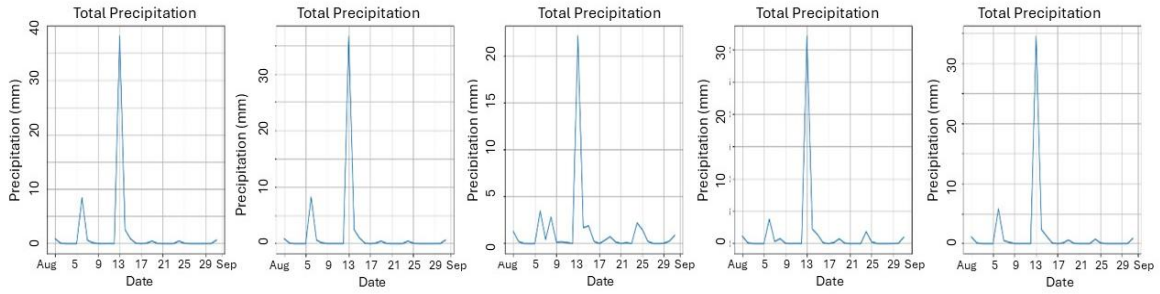

Figure 4.5. Total Precipitation for Regions 1, 2, 3, 4 and 5, for the August-September period.

Across all five plots of daily total precipitation for August 2023, the baseline is essentially dry, with near-zero values for most days. There is a minor early event around 6–7 Aug and a clear, common main event on 12–13 Aug (the strongest of the month), followed by a rapid decay and residual amounts on 14–16 Aug. Thereafter the curves remain very low, with sporadic, very small blips around 23–26 Aug and toward the end of the month (31 Aug–1 Sep). Differences among the five series are mainly in the magnitude of the mid-month peak and small phase shifts (up to ~1 day). Overall, the plots agree that August was predominantly dry, punctuated by a single dominant rainfall episode in mid-month.

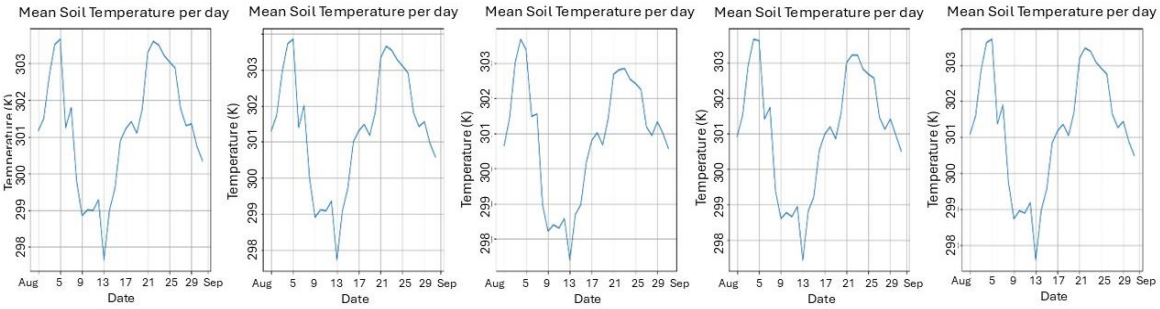

Figure 4.6. Mean Soil Temperature per Day for Regions 1, 2, 3, 4 and 5, for the August-September period.

All five plots show the same pattern: a moderate start around 300–301 K, a pronounced early peak on 4–6 Aug (~303–304 K), a clear cool spell on 8–11 Aug (minima ~298–299 K), a gradual rebound on 13–18 Aug (~301–302 K), and a second, broader peak on 21–23 Aug (~303–304 K), followed by a decline toward month's end (~300–301 K). Differences across series are limited to minor phase shifts (up to ~1 day) and amplitude of about 0.5–1.0 K. The total intra-monthly range is ~5–6 K. Compared to air temperature, the soil curves are smoother, as expected from thermal inertia.

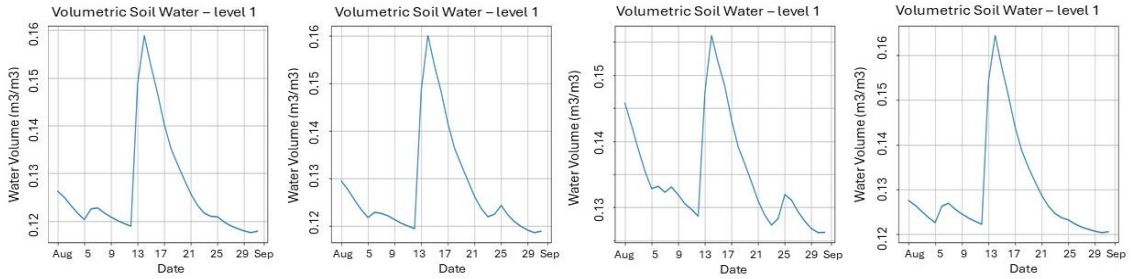

Figure 4.7. Volumetric Soil Water-level 1 for Regions 1, 2, 3 and 4, for the August-September period.

Across all four plots for the topsoil layer (0–7 cm) the pattern is the same: gradual early-month drying (down to ~0.120–0.125), a sharp spike on 13–14 Aug reaching ~0.155–0.165—consistent with the main rainfall event—followed by rapid, drainage/evaporation-type decay through ~18–20 Aug and a slower decline toward month's end to ~0.118–0.122. Minor secondary wiggles appear around 24–26 Aug but do not alter the prevailing dry trend. Differences between plots are limited to small phase shifts (<~1 day) and peak amplitude (range ~0.010–0.015 in volumetric fraction). Overall, timing and shape are consistent, indicating prompt wetting after rainfall and a quick return to dry conditions.

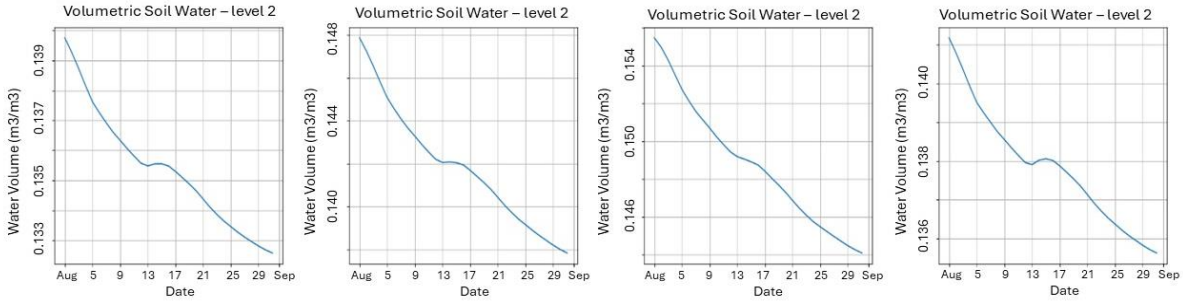

Figure 4.8. Volumetric Soil Water-level 2 for Regions 1, 2, 3 and 4, for the August-September period.

Across all four diagrams for the 7–28 cm layer there is a monotonic drying throughout the month, declining from about 0.140–0.156 at the start to 0.133–0.144 by the end. Around 13–15 Aug only a modest slowdown, consistent with a muted response of the deeper soil to the mid-month rainfall. After 16–18 Aug the downward trend resumes smoothly with no major oscillations. Differences between plots mainly reflect different initial moisture levels and the magnitude of the total drop (~0.006–0.012 in volumetric fraction), while the curve shape is highly consistent. Overall, Layer 2 exhibits a slower, more inert behaviour than the topsoil, with limited impact from the mid-month rain.

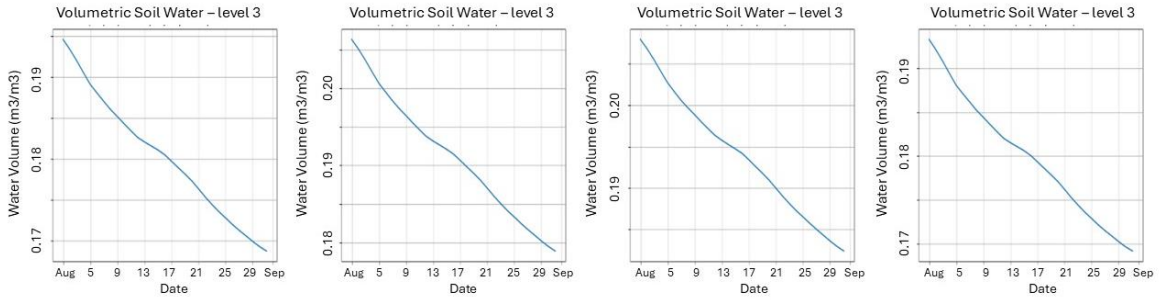

Figure 4.9. Volumetric Soil Water-level 3 for Regions 1, 2, 3 and 4, for the August-September period.

Across all four plots for the deeper layer (28–100 cm) there is an almost linear, monotonic drying throughout the month: from initial values of ~0.195–0.207 down to ~0.170–0.180 by the end. No clear response to the mid-month rainfall is evident, indicating strong hydraulic/thermal inertia at depth and limited downward percolation on day-to-week timescales. Differences between diagrams mainly reflect different initial levels and the magnitude of the total decline (~0.018–0.028 in volumetric fraction), while day-to-day

oscillations are negligible. Overall, Layer 3 shows steady drainage/consumption of soil moisture, with no short-term rebounds.

4.3 Analysis of climatic parameters – ERA5

In this section, the four meteorological variables that constitute the inputs of the Fire Weather Index (FWI) are examined: 2 m air temperature (°C), relative humidity (%), 10 m wind speed (km/h), and daily precipitation (mm/24 h). The first three are evaluated at noon (12:00 local time, 10 UTC), in order to approximate the most unfavorable part of the diurnal cycle, while precipitation is used as a daily accumulation per hour because it cumulatively affects fuel moisture. The focus is on their co-evolution during the fire season and on how combinations of high temperature, low humidity, and strong wind under conditions of absence of recent rainfall create windows of high risk.

The data were retrieved from the Copernicus Climate Data Store (CDS) (ERA5 reanalysis, surface levels) for the long period 1940–2024, at coordinates considered representative of the burned area (N: 41.14°, S: 40.86°, W: 25.72°, E: 26.18°). Since the spatial unit is a grid cell (square on the ground), a spatial mean was first calculated over the intersecting pixels, so that one value per variable per day was obtained. Then, for the months of July, August, and September, basic statistics were produced (minimum, maximum, mean, 25th–75th percentile). For the study of these parameters, one plot was created for each variable, in which the statistics of this period are shown, along with the corresponding values of 2023 when the event occurred. On the plots, the fire period is highlighted with an orange background. Processing and visualization were performed in Python. In the following plots, a stepwise interpretation of the variations of each variable is provided, as a short climatological depiction of the region.

<u>2 m air temperature:</u>

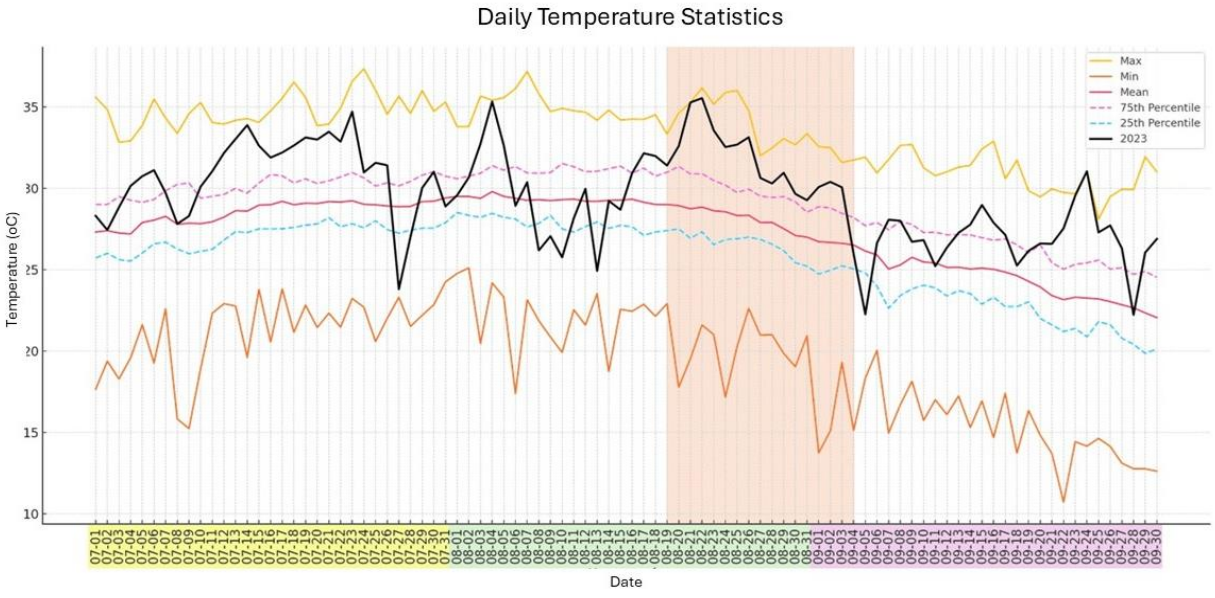

Figure 4.10. Daily temperature statistics for July–September (1940–2024) based on ERA5 reanalysis.
The yellow and orange lines represent the historical maximum and minimum daily values, respectively, while the red line shows the average. The dashed magenta and blue lines correspond to the 75th and 25th percentiles of the climate distribution, and the solid black

line represents the daily values for the year 2023. The shaded orange area highlights the fire period in August–September 2023.

In the climatic background of July–September, daily means range approximately from 22 to 30 °C (mean value 24.4 °C), the 25th percentile ranges around 20–28.5 °C (mean value = 27.8 °C), and the 75th percentile is between 24.5 and 31.5 °C (mean value = 29 °C). The corresponding daily extremes (per date) are typically in the range of 11–25 °C for minima and 28–37 °C for maxima. Across the entire period, all curves of the climatic statistics show a mild increase from mid-July towards mid-August and a gradual decrease until the end of September.
The 2023 curve of the noon 2 m air temperature in the quarter 01/07–30/09 shows a clear seasonal course with pronounced intramonthly variability. In July it starts close to the climatic mean and, as the month progresses, it shows a mild upward trend. It is often located between the mean and the 75th percentile, and by the end of July it exceeds the upper climatic zone (≥75th percentile). In early August it remains warm, but around 8–10/8 a sudden drop occurs, where the curve briefly falls close to or below the 25th percentile. This drop is short-lived, as immediately afterward the series recovers rapidly and from mid to late August a continuous warm episode develops, with the 2023 curve persistently above the mean and on most days above the 75th percentile, reaching the maximum temperature of the season during the peak around 21–22/8. At the end of August a gradual decline is recorded, though without leaving the upper climatic zone. Entering September, the temperature initially remains high (still in the ≥75th percentile zone in the first days), but then shifts into a lower thermal regime. In the first ten days a more notable drop is recorded, with values moving close to the mean or within the 25th–75th percentile zone (at times approaching the lower quartile). From mid to late September a moderated recovery appears (fluctuations around or slightly above the mean), while at the very end of the month the series follows the seasonal declining course, closing close to the climatic mean for the season.
More specifically, during the fire period (19/8–3/9), the temperature followed this course: On 19/8 (31.40 °C) the warm episode begins. The value is marginally above the 75th percentile and higher than the previous week, indicating that the warming is established. On 20/8 (32.60 °C) a further increase is observed compared to the previous day and the temperature is clearly above the 25th–75th zone. The curve is firmly placed in the upper climatic spectrum. The next two days show a sharp step upwards, reaching the maximum for the season on 21/8 (35.3 °C), while on 22/8 the maximum temperature for 2023 is reached (35.55 °C), remaining clearly above the 75th percentile. On 23 and 24/8 a mild decrease follows (33.56 °C and 32.54 °C respectively), reaching stabilization on 25/8 (32.69 °C) with a slight increase on 26/8 (33.14 °C). A clear drop follows on 27/8 (30.64 °C), while in the next two days the temperature remains relatively stable (28/8 – 30.30 °C, 29/8 – 30.95 °C). Another slight drop is observed on 30/8 (29.66 °C), and on 31/8 the local minimum of the period is recorded (29.27 °C). On the first two days of September there is a small increase (1/9 – 30.08 °C, 2/9 – 30.40 °C). On the last day of the fire (3/9 – 30.06 °C) the temperature begins to decrease, which becomes more pronounced in the following days. The entire fire period remains very warm and above the 75th percentile.
In summary, from 19 to 26/8 a continuous and intense warm episode is recorded (peaks 21–22/8), followed by a mild–gradual decline 27–31/8 with a local low on 31/8, and finally a new increase 1–3/9, when noon temperatures remain higher than the upper climatic zone.

10 m wind speed:

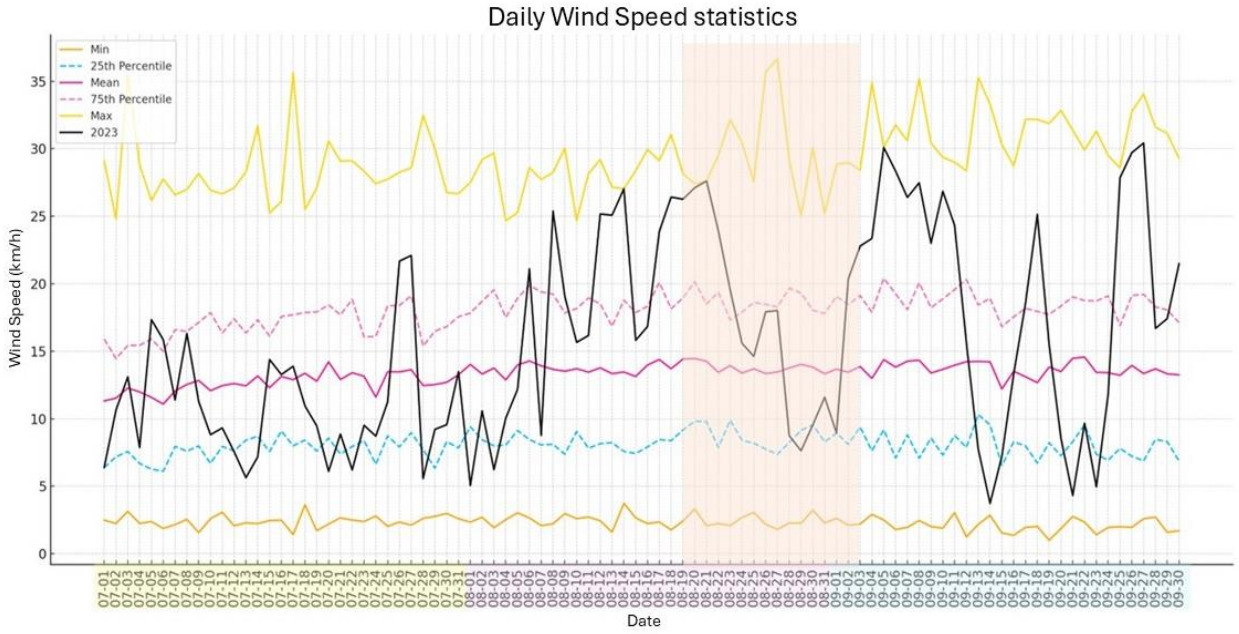

Figure 4.11. Daily Wind Speed Statistics for July–September (1940–2024) based on ERA5 reanalysis.
The yellow and orange lines represent the historical maximum and minimum daily values, respectively, while the purple line shows the average. The dashed magenta and blue lines correspond to the 75th and 25th percentiles of the climate distribution, and the solid black line represents the daily values for the year 2023. The shaded orange area highlights the fire period in August–September 2023.

In the climatic background, the daily mean wind speed ranges approximately from 11 to 14.5 km/h (mean of the quarter about 13 km/h), the 25th percentile lies between 6–10 km/h (mean = 8 km/h), and the 75th percentile between 14.5–20.5 km/h (mean = 18 km/h). The daily minima per date range 1–3.7 km/h, while the daily maxima reach about 24.5–36.5 km/h. In general, during this quarter the curves of the statistics show relative stability in wind speed.
The 2023 curve starts in July around the climatic mean and often moves between the mean and the 75th percentile. In practice, values of ~10–16 km/h are seen in most of the month, with sporadic increases towards 17–22 km/h near the end. In early August the profile remains moderate, but from mid-August a clear escalation is recorded. The line steadily rises into the upper zone (≥75th percentile) and on 21–24/8 reaches ~24–27 km/h. A late August decline follows, before a mild recovery. Entering September a second peak is observed, again above the 75th percentile. The rest of September is variable, with alternations of mild days (<10–12 km/h) and strong episodes reaching ~24–31 km/h, closing the month at mid–upper levels (~17–21 km/h).
More specifically, during the fire period (19/8–3/9), the wind speed behaved as follows: On 19/8 it reaches 26.26 km/h, well above the 75th percentile. On 20/8 it strengthens to 27.12 km/h, remaining in the upper climatic zone. The peak of the initial wave comes on 21/8 (27.61 km/h), the maximum wind speed of that day, before beginning a gradual decline in the following four days (22/8 – 23.92 km/h, 23/8 – 19.54 km/h, 24/8 – 15.59 km/h, 25/8 – 14.62 km/h), with values within the 25th–75th zone. On 26–27/8 a small recovery is observed (17.92 and 18.01 km/h), again within the 25th–75th zone. A sharp

drop follows on 28/8 (8.75 km/h) and a local minimum on 29/8 (7.63 km/h), clearly below the 25th percentile. Wind speed recovers mildly on 30/8 (9.55 km/h) and 31/8 (11.59 km/h), remaining within the 25th–75th. Entering September, a brief stabilization at moderate levels is observed (8.94 km/h on 1/9), followed by a second peak on 2 and 3/9 (20.36 km/h and 22.79 km/h respectively), again above the 75th percentile.
In other words, the 2023 curve presents a double phase: a strong reinforcement episode 19–21/8 (26.3–27.6 km/h), a decline 24–31/8 culminating in the low of 7.63 km/h on 29/8, and a new increase 2–3/9 (20.36–22.79 km/h). Throughout 19/8–3/9, values alternate above the 75th zone (19–23/8), within the 25th–75th (24–28/8, 30–31/8, 1/9), and below the 25th (29/8), clearly depicting the wind fluctuations during the event.

Precipitation:

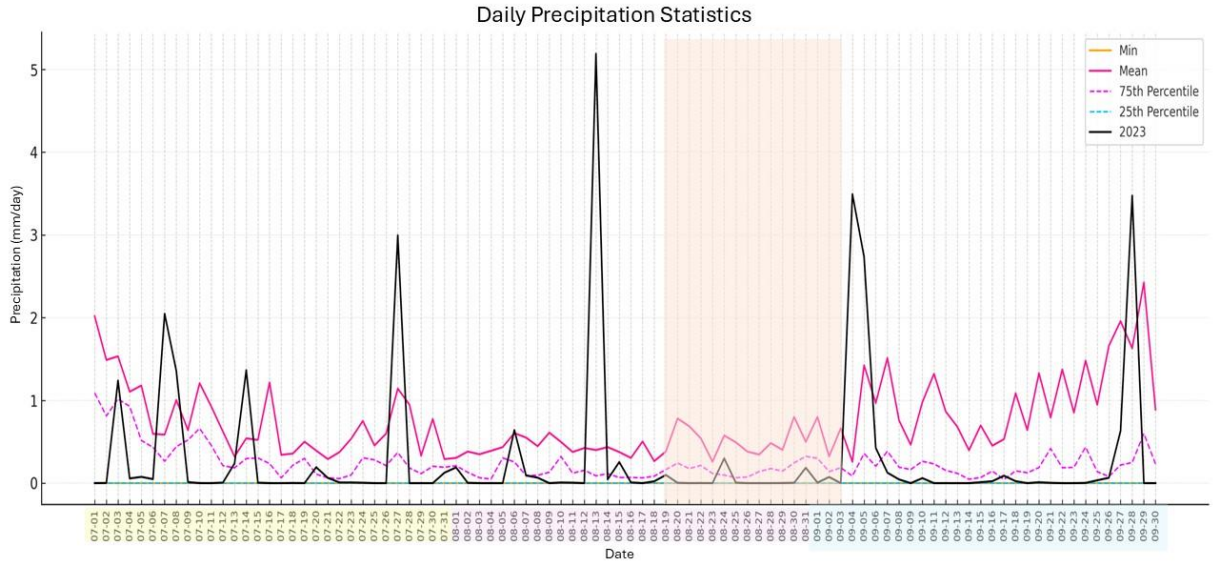

Figure 4.12. Daily Precipitation Statistics for July–September (1940–2024) based on ERA5 reanalysis.
The orange line represent the historical minimum daily values, respectively, while the magenta line shows the average. The dashed magenta and blue lines correspond to the 75th and 25th percentiles of the climate distribution, and the solid black line represents the daily values for the year 2023. The shaded orange area highlights the fire period in August–September 2023.

The months July–September are climatically dry in the study area. In the series statistics (daily climatic indices per date of the quarter), the daily mean is approximately 0.26–2.43 mm/day (mean = 0.7), the 25th percentile is practically zero, while the 75th percentile remains low, about 0.04–1.09 mm/day (mean = 0.2) and daily minima are 0.0 mm/day. Therefore, most summer days are dry or with traces of rainfall, with sporadic storm peaks. In 2023 the precipitation curve shows few, well-defined wet days within long dry intervals. In July small episodes occur on 3/7 (1.24 mm), 7/7 (2.05 mm), 8/7 (1.36 mm), 14/7 (1.37 mm), and 27/7 (~3.00 mm). In August, apart from small amounts on 1/8 (0.19 mm) and 6/8 (0.64 mm), 13/8 stands out with 5.19 mm, the largest value of the quarter. In September, a three-day episode follows on 04/09 (3.49 mm), 5/9 (2.73 mm), and 6/9 (0.43 mm), along with late-month peaks (27/9: 0.63 mm, 28/9: 3.48 mm, 30/9: 3.17 mm). On the remaining days records are 0–0.1 mm/day, meteorologically negligible.

During the critical period, daily rainfall accumulation is very low and discontinuous. Indicatively: 19/8 – 0.10 mm, 20/8 – 0.004 mm, 22/8 – 0.001 mm, 24/8 – 0.299 mm (the only value exceeding the corresponding 75th percentile of the day), 25/8 – 0.006 mm, 26–27/8 – 0.000 mm, 28/8 – 0.0001 mm, 29/8 – 0.0011 mm, 30/8 – 0.0043 mm, 31/8 – 0.186 mm, 1/9 – 0.006 mm, 2/9 – 0.074 mm, 3/9 – 0.000 mm. All values are clearly below 1 mm/day, without hydrological significance, except for 24/8 and 31/8 where a small increase in rainfall is observed (<0.3 mm/day). Meteorologically, the period remains dry, consistent with the summer climate of the region and with the climatic statistics of the season.

Relative humidity:

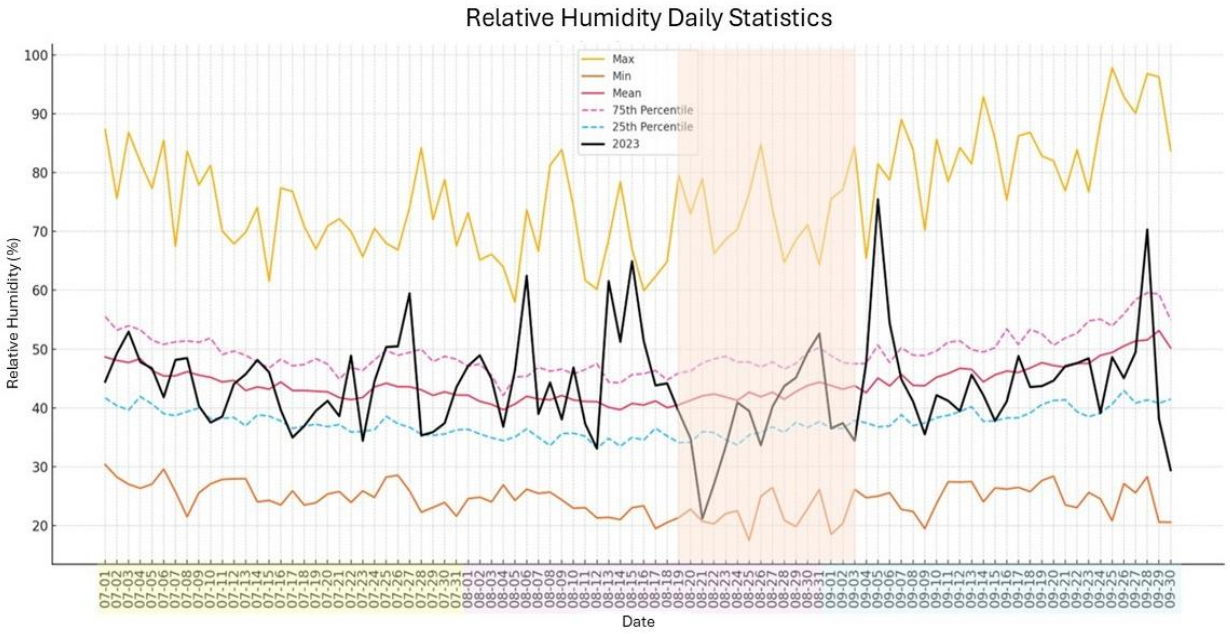

Figure 4.13. Relative Humidity Daily Statistics for July–September (1940–2024) based on ERA5 reanalysis.
The yellow and orange lines represent the historical maximum and minimum daily values, respectively, while the red line shows the average. The dashed magenta and blue lines correspond to the 75th and 25th percentiles of the climate distribution, and the solid black line represents the daily values for the year 2023. The shaded orange area highlights the fire period in August–September 2023.

In the climatic background 1/7–30/9, the ranges of relative humidity statistics are as follows: the daily climatic mean ranges 40–53% (mean = 44%), the 25th percentile 33–43% (mean = 37.5%), the 75th percentile 42–59.5% (mean = 49%), while daily minima are 17.5–30.5% and daily maxima 58–98%. Based on the statistical curves, a mild decrease of relative humidity is observed from early July to mid-August, while afterwards until the end of September a mild increase follows.
The 2023 line follows the seasonal course but with clear intramonthly variability. In July it moves around the climatic mean, in early–mid August it records a downward trend and falls below the 25th–75th zone on certain peak dryness days, while from the last ten days of August it tends to gradually recover, with the line returning within or even above the middle climatic zone, and strengthening in early September.
More specifically, during the fire period (19/8–3/9), relative humidity evolved as follows: On 19/8 (39.3%) the 2023 line is slightly below the mean and trending downward. On 20–

22/8 the driest part of the period is recorded (34.8%, 21.2%, 27%), with 21/8 showing the lowest value for that day. The 2023 curve plunges below the 25th percentile, that is, a state of intense dryness for noon values. On 23–24/8 (33.4%, 40.9%) the 2023 line begins a mild recovery, moving from the low zone towards the 25th–50th. From 25/8 to 31/8 (39.5%, 33.6%, 40.2%, 43.7%, 45.2%, 49.4%, 52.7%) the picture stabilizes at higher levels. The 2023 curve rises stepwise, generally remaining within the middle zone (25th–75th), with small local oscillations around the daily means. Entering September, a clearer strengthening of humidity is observed. On 1–2/9 (36.5%, 37.4%) the 2023 line continues upward, approaching or even surpassing the climatic mean. On 3/9 (34.4%) it shows a peak (visually near the upper quartile, even higher), closing the period with clear moistening compared to the extremely dry mid-August.
In summary, the interval starts with intense dryness around 20–22/8, when noon 2023 values fall below the 25th percentile (climatically ~36–38%). From 25–31/8 a gradual recovery is observed with values within the 25th–75th zone (~35–49%), while on 1–3/9 humidity strengthens and approaches or surpasses the climatic mean, at times reaching the upper quartile (~50%+). In other words, from a very dry mid-August the field steadily moistens towards early September.

4.4 Fire Weather Index (FWI) using data from the Copernicus Climate Data Store

In this subsection, the Fire Weather Index (FWI) was calculated for the study area on a daily basis for the entire period 1940–2024, using MATLAB. The meteorological inputs (2 m air temperature, relative humidity, 10 m wind speed) were taken at noon values (≈12:00 local time), while precipitation was used as a 24 h daily total. The data were obtained from the Copernicus Climate Data Store (CDS) and preprocessed to spatially represent the area under study.

The total population of daily FWI values (1940–2024) is strongly right-skewed. Most days accumulate at low to medium values and a smaller but significant fraction extends into high and extreme values.

Table 4.1. FWI Statistics ERA5

Average	Min	Max	25th percentile (P25)	75th percentile (P75)	90th percentile (P90)	95th percentile (P95)
12.14	1.73e-08	87.16	0.57	19.89	35.42	43.68

In operational terms, this means that FWI > ~35 (90th) and especially FWI > ~44 (95th) correspond to days of high or very high fire danger.

Based on the above, the following analysis does not rely solely on the simple mean, but focuses on the shape of the distribution (histograms), the change between climatic periods (decadal comparison), the evolution of exceedance days above the 90th and 95th percentiles per year, and the July–September season through a plot where 2023 is placed on top of the climatic frame. This arrangement helps to connect the long-term picture with the most recent conditions in the Mediterranean and in Greece.

For a more complete understanding of the index, an initial histogram of all available daily FWI values (1940–2024) is presented. The distribution is strongly right-skewed: the largest number of days is concentrated at low values (bin 0–5 with ~15,000 days), while frequency decreases rapidly as the index increases and extends up to about 85–90. The

descriptive statistics of the full period confirm that days of high and very high fire danger (≥P90, ≥P95) constitute a small but substantial portion of the record.

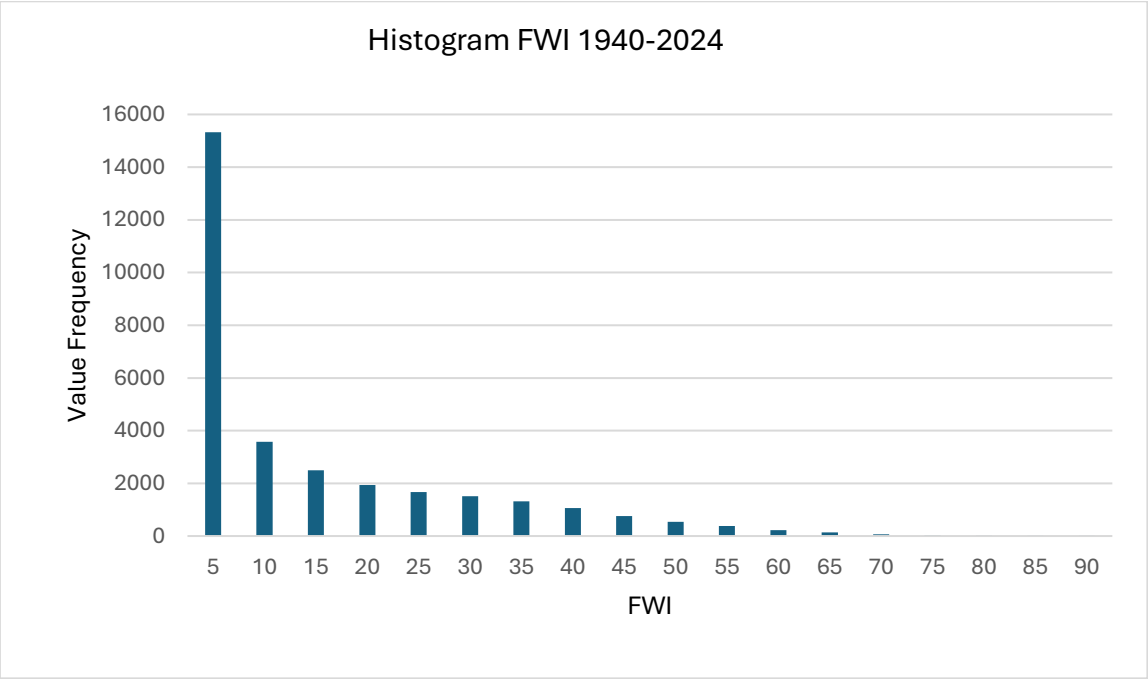

Figure 4.14. Histogram FWI 1940-2024, ERA5

4.4.1 Evolution of FWI exceedance days (90th and 95th percentiles)

As a continuation of the overall depiction of FWI, the number of days per calendar year (1940–2024) with FWI above two reference thresholds was calculated: the 90th and 95th percentiles of the climatic distribution. The choice of these thresholds follows international practice, where the 95th is widely used as “very high or extreme fire danger days”, while in analyses specifically for Greece and the Eastern Mediterranean the 90th has also been employed to better capture persistent hot and dry summer episodes. The article *State of Wildfires 2023–2024* depicts Greece with a 90th percentile threshold in August 2023, while for other regions it examines the 95th [Jones et al., 2024].

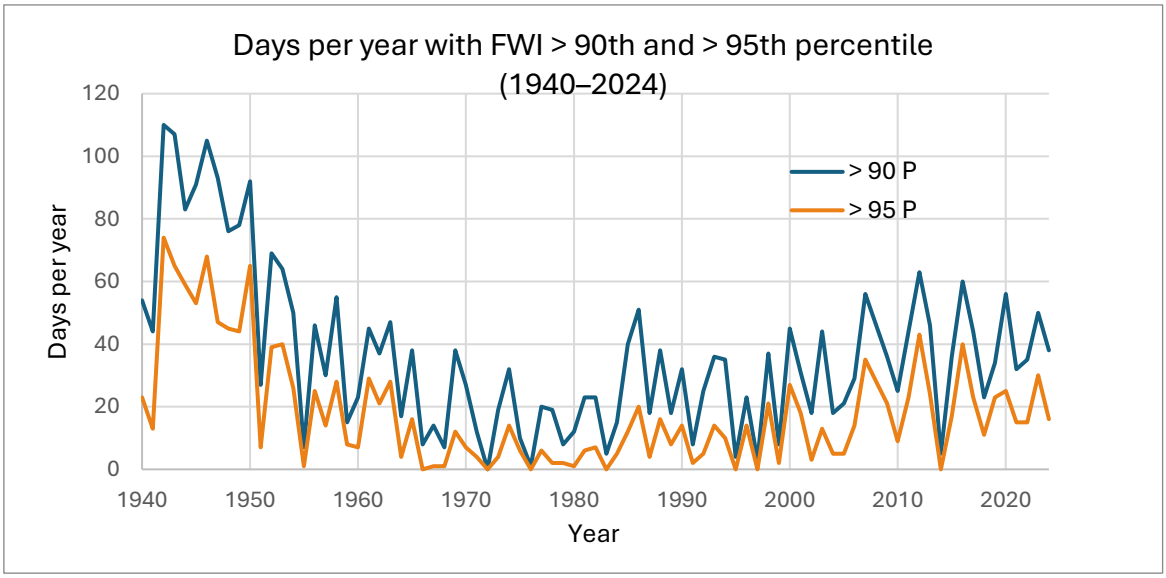

Figure 4.15. Days per Year with FWI > 90th and 95th percentile (1940-2024), ERA5

Table 4.2. Decadal statistics of FWI exceedances above the 90th and 95th percentiles (1940–2024), ERA5

Period	Years	Average days >90p	Average days >95p	Max >90p (year)	Max >95p (year)	% years with ≥30 days >90p	% years with ≥15 days >95p
1940–1959	20	64.8	37.2	110 (1942)	74 (1942)	85%	75%
1960–1979	20	21.1	8.2	47 (1963)	29 (1961)	30%	20%
1980–1999	20	22.7	8.0	51 (1986)	21 (1998)	35%	15%
2000–2009	10	34.4	16.9	56 (2007)	35 (2007)	60%	50%
2010–2019	10	38.0	21.3	63 (2012)	43 (2012)	70%	70%
2020–2024	5	42.2	20.2	56 (2020)	30 (2023)	100%	100%
1940–2024	85	36.6	18.3	110 (1942)	74 (1942)	56%	46%

The plot shows a very high frequency of exceedances at the beginning of the time series (early–mid 1940s), with >90th visually exceeding ~100 days per year and >95th reaching up to ~70 days per year. This is followed by a strong decline from the mid-1950s to the late 1970s, when exceedances drop to low or very low levels (often only a few or even zero days per year for >95th). From the mid–late 1980s and especially after 2000, a gradual recovery is evident. The >90th frequently reaches dozens of days per year, while the >95th shows systematic but clearly fewer exceedances. In the 2010s and early 2020s there are peaks, with 2023 recording an increased number of exceedances at both thresholds, though not at the absolute maximum of the series.

The time series of days per year above the 90th and 95th percentiles shows pronounced interannual variability but also an upward trend from the late 1990s onwards. The two signals (90p and 95p) evolve together, when days >90p increase, days >95p usually increase as well, simply in smaller absolute numbers, as expected from the definition of the thresholds. The period 2007–2023 stands out with more frequent exceedances and higher peaks compared to previous decades, which is consistent with the warmer and drier summer climatology documented for the Mediterranean. It is important to note that decades before 1979 have higher uncertainty due to sparser observations in the fields feeding into the FWI. Therefore, emphasis in comparisons should be given to the more recent decades.

4.4.2 Comparison of FWI distributions: 1961–1990 vs 1991–2020

The comparison of the two 30-year periods with identical bins of 5-unit width (FWI → 5–90) shows a clear shift of the distribution toward higher FWI values in the more recent period (1991–2020). This is visible both in the double histogram and in the “difference” plot (1991–2020 minus 1961–1990).

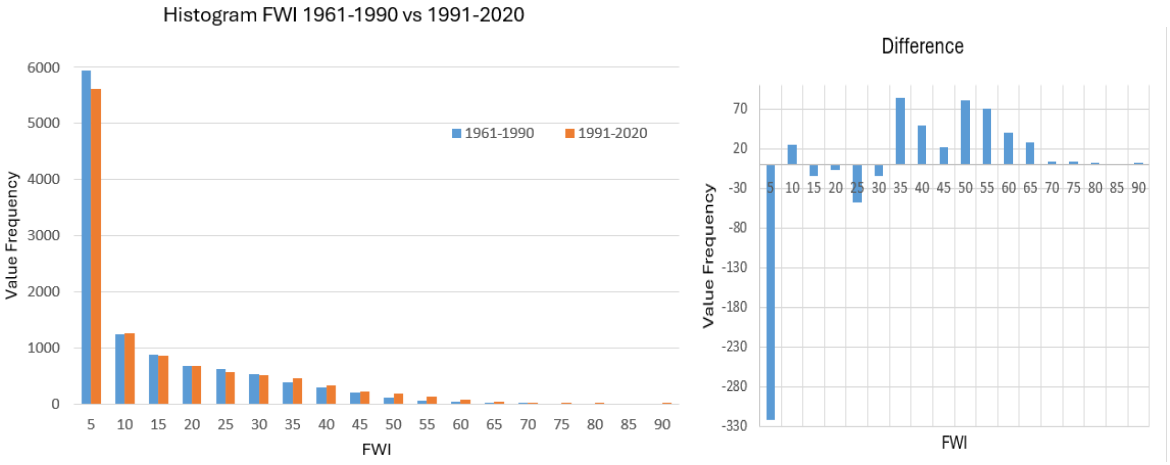

Figure 4.16. Histogram Compariton FWI: 1961–1990 vs 1991–2020 and Difference figure

From these plots it appears that low bins decrease, while middle–high bins increase. In bin FWI=5 the counts decrease by 322 days (5,940 → 5,618, ~–5.4%). Small negative changes are also recorded at 15–30 (for example bin 25: –48, ~–7.8%). At higher values (≥35) the increases become clear and consistent. Very high and extreme values (≥70) in the older 30-year period are practically absent, while in the newer they appear (for example bin 75: 0→3, 80: 0→2, 85: 0→2, 90: 0→1). That is, FWI levels that essentially did not occur in 1961–1990 now appear, even if rarely. Overall, the probability of days with high to very high FWI (≥50) is significantly greater in 1991–2020 compared with 1961–1990, indicating increased likelihood of days conducive to high-intensity wildfires.

Table 4.3. Absolute and relative changes in the frequency of FWI ≥35 events between 1961–1990 and 1991–2020, ERA5

FWI bin	1961–1990 (count)	1991–2020 (count)	Δ count	Δ %
35	379	462	+83	+21.90%
40	289	338	+49	+16.96%
45	202	224	+22	+10.89%
50	104	185	+81	+77.88%
55	58	128	+70	+120.69%
60	29	69	+40	+137.93%
65	10	37	+27	+270.00%
70	4	4	0	0.00%

FWI bin	1961–1990 (count)	1991–2020 (count)	Δ count	Δ %
75	0	3	+3	From zero base
80	0	2	+2	From zero base
85	0	2	+2	From zero base
90	0	1	+1	From zero base

Note: For bins 75–90 no percentage change is computed because in the first period frequency is zero (emergence of new values in the second period).

4.4.3 Daily evolution of the FWI (July–September) and analysis of the 19/8–3/9/2023 episode

Similar to the plots of climatic parameters in section 4.3, the behavior of the FWI is analyzed for the July–September period.

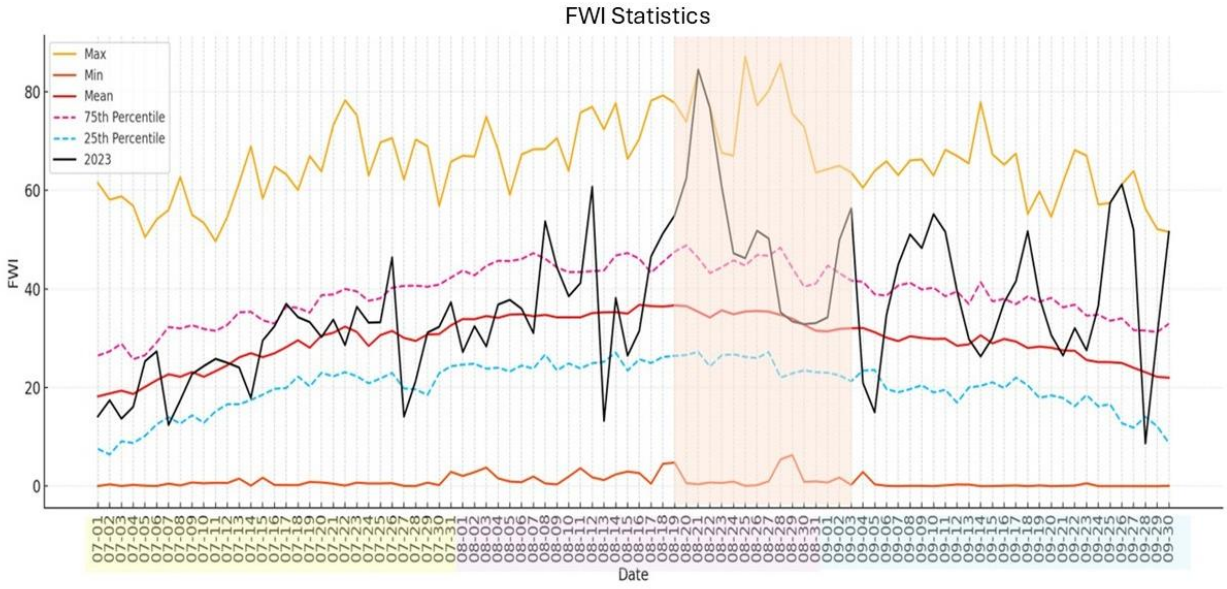

Figure 4.17. FWI Statistics July–September (1940–2024) based on ERA5 reanalysis. The yellow and orange lines represent the historical maximum and minimum daily values, respectively, while the red line shows the average. The dashed magenta and blue lines correspond to the 75th and 25th percentiles of the climate distribution, and the solid black line represents the daily values for the year 2023. The shaded orange area highlights the fire period in August–September 2023.

In the climatic statistics of this season, the daily mean FWI ranges approximately from 18.2 to 36.8 (mean value of the period=29.8). The 25th percentile ranges from 6.4 to 27.3 (mean=20.3), while the 75th percentile from 25.7 to 48.9 (mean=39.2). The corresponding daily extremes (per date) are typically 0.0–6.3 for minima and 49.7–87.2 for maxima. As a seasonal trajectory, the climatic curves show a mild rise from mid-July to late August and a gradual decline toward late September.

The 2023 series starts in July with values close to the seasonal mean (within the 25–75 percentile range) and gradually increasing, often lying above the climatic mean and on many days entering the ≥75th percentile zone. The mean of the series for the entire three-month period is 36.4, that is about +6.5 units higher than the seasonal climatic mean (29.8). Throughout July–September, roughly one-third of days are above the 75th percentile, confirming that summer 2023 generally had a high danger index, with a strong peak toward late August.

Against the climatic background described above, the period 19/8–3/9 shows a continuous sequence of very high FWI values with a clear peak followed by decline. Specifically, on 19/08 the series opens at 54.9, already above the 75th percentile of the day (42.2). On 20/08 it rises further to 62.5, peaking on 21/08 at 84.5, a value close to the historical maximum, which also occurs on 22/08 at 76.7, while on 23/08 the value decreases but remains very high (60.8). On 24/08 and 25/08 the curve is lower (47.2 and 46.2), before returning above the 75th percentile zone on 26/08 (51.8) and 27/08 (50.2). A clear decline follows over the next days (28/08–35.3, 29/08–33.4, 30/08–32.9, 31/08–33.1). Entering September, a small recovery is observed (01/09–34.25), while on 2/9 (49.9) and 3/9 (56.4) the series rises again above the 75th percentile. Overall, the episode extends from 19 to 27/08 with a peak on 21–22/08, followed by a four-day decline 28–31/08 and then renewed strengthening 1–3/09.

In terms of interpretation, FWI values on the scale widely used in Europe are referenced in Table 2 of section 1.4. Within this framework, the period 19/8–3/9 is dominated by Very High to Extreme danger days: 8 days (19–23/08, 26–27/08, 03/09) exceed 50 (Extreme), two more lie just below this (24–25/08 ~46–47), while the four-day “pause” 28–31/08 falls in the mid–high range 33–35. The peaks on 21/08 (84.53) and 22/08 (76.70) are not only well above the 75th percentile of their respective dates, but reach the historical maxima for the season, marking this period as one of the most intense “windows” of favorable spread conditions within the summer quarter.

4.5 Analysis of the FWI using ISIMIP3a data

In correspondence with section 4.2, this part examines the four meteorological variables that constitute the inputs of the FWI index: 2 m air temperature (°C), relative humidity (%), 10 m wind speed (km/h), and daily precipitation (mm/24 h). The first three are evaluated at local noon time (12:00 local, 10 UTC).

The data were retrieved from the ISIMIP3a program (Input Data → Climate related forcing → Atmospheric forcings), using the GSWP3–W5E5 dataset, for the period 1941–2019, at slightly different coordinates that were deemed representative of the burned area for the model’s needs (N: 41.34°, S: 40.84°, W: 25.70°, E: 26.20°). For this study two different scenarios were examined: obsclim (observed climate, with anthropogenic influences) and counterclim (counterfactual climate, without anthropogenic influences). Since the spatial unit is a grid cell, a spatial average was first computed across intersecting pixels so that there is one value per variable per day. Subsequently, for July, August, and September, basic statistics were produced (minimum, maximum, mean, 25th–75th percentile). For this purpose a plot was generated for each variable in which the statistics of this period are displayed (without the corresponding 2023 values since they are not included in the data). Processing and visualization were performed in Python.

4.5.1 Obsclim scenario

The following plots provide a stepwise interpretation of the variability of each variable as a brief climatological depiction of the area.

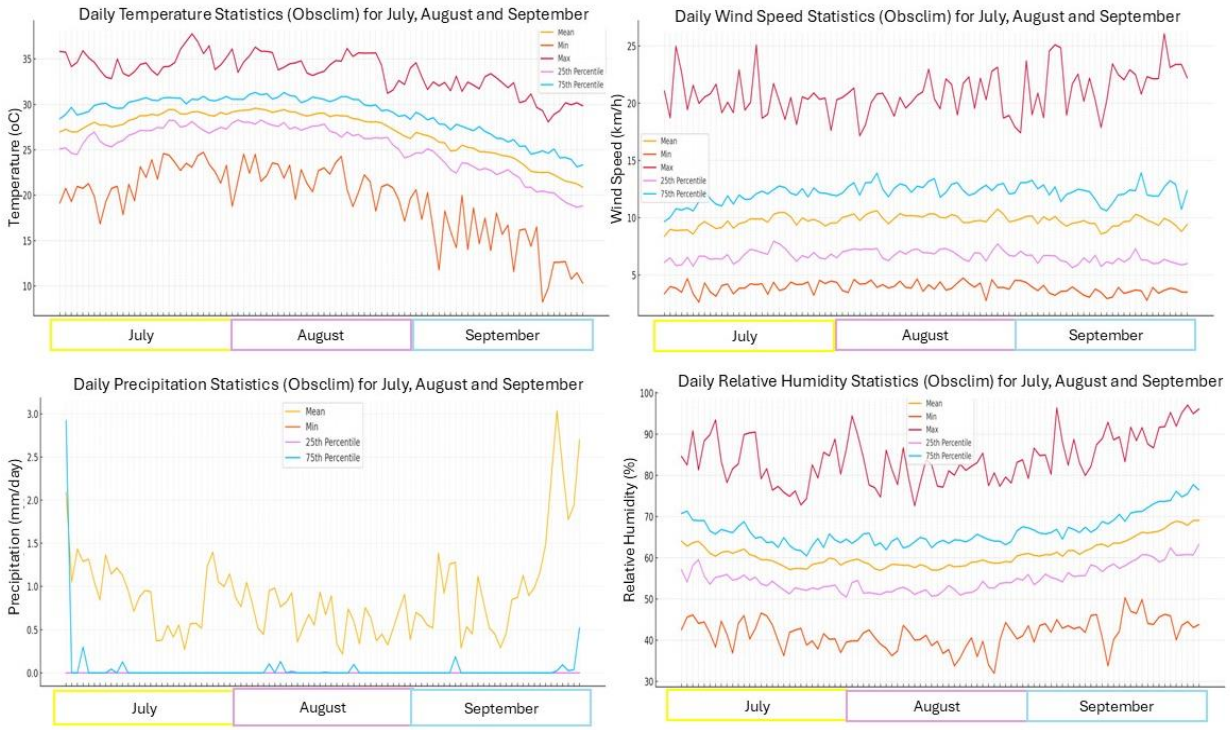

Figure 4.18. FWI Parameters Statistics for July-September period based on Obsclim scenario, (a) Temperature, (b) Wind Speed, (c) Precipitation, (d) Relative Humidity. The red and orange lines represent the historical maximum and minimum daily values, respectively, while the yellow line shows the average. The dashed blue and magenta lines correspond to the 75th and 25th percentiles of the climate distribution. The shaded orange area highlights the fire period in August–September 2023.

Temperature (°C): In the climatic background of July–September, daily means range approximately from 20.9 to 29.6 °C (mean value 27.0 °C), the 25th percentile ranges around 18.7–28.3 °C (mean value 25.3 °C) and the 75th percentile is approximately 23.1–31.3 °C (mean value 28.9 °C). The corresponding daily extremes (per date) are typically in the range 8.2–24.7 °C for minima and 28.1–37.8 °C for maxima. Over the period as a whole the curves show a mild rise from mid July toward early–mid August and a gradual decline toward late September.

Wind speed (km/h**):** Daily means range approximately from 8.4 to 10.8 km/h (mean value 9.73 km/h), the 25th percentile is 5.6–8.0 km/h (mean value 6.64 km/h) and the 75th percentile is 9.7–13.9 km/h (mean value 12.2 km/h). Daily extremes are usually in the range 2.6–4.8 km/h for minima and 17.2–26.1 km/h for maxima. The seasonal picture shows a mild strengthening until mid August and a slight weakening toward late September with transient peaks.

Precipitation (mm/day): Daily means range approximately from 0.2 to 3.0 mm/day (mean value 0.90 mm/day), the 25th percentile is practically 0 mm/day for most of the period (mean value 0.00), while the 75th percentile ranges 0.00–2.9 mm/day (mean value 0.05 mm/day), reflecting the dry summer regime and daily extremes are 0 mm/day for minima. Overall, dryness prevails in July–August with a higher likelihood of episodes toward the end of the season.

Relative humidity (%): Daily means range approximately from 57 to 69.1% (mean value 60.9%), the 25th percentile is 50.4–63.3% (mean value 54.9%) and the 75th percentile is 60.4–77.8% (mean value 66.6%). Daily extremes are usually in the range 32–50.4% for

minima and 72.6–97.1% for maxima. The seasonal behavior shows a mild decrease from mid July to mid August and a gradual recovery of humidity toward late September.

4.5.1.1 FWI using ISIMIP3a obsclim data

The Fire Weather Index (FWI) was then calculated for the study area on a daily basis for the period 1941–2019, using the obsclim data of the ISIMIP3a program (GSWP3–W5E5 dataset). The meteorological inputs (2 m air temperature, relative humidity, 10 m wind speed), as already noted, were taken at noon values (≈12:00 local time), while precipitation was used as a 24 h daily total. The analysis focuses on the summer period July–September. It is noted that decades before 1979 carry higher uncertainty due to sparser observations in the fields that feed into the FWI.

The total population of daily FWI values (1941–2019) shows pronounced right skewness. Most days are concentrated at low to medium values, while a small but significant fraction extends to high or extreme values. In summary, the descriptive statistics for the full period are:

Table 4.4. FWI Statistics, Obsclim

Anerage	Min	Max	25th percentile (P25)	75th percentile (P75)	90th percentile (P90)	95th percentile (P95)
5.97	4.49e-09	51.80	0.22	9.41	19.08	23.68

In operational terms, days with FWI > ~19 (90th) and especially FWI > ~24 (95th) correspond to high or very high danger relative to the climatic background of 1941–2019.

The analysis does not limit itself to simple averages but focuses on the overall shape of the distribution and on the statistical properties of daily values. In the histogram of all days of 1941–2019 the distribution appears strongly right-skewed. The largest number of days is concentrated at low index values (0–5), with more than 18,000 days in this range, while frequency decreases rapidly as the index increases. Nevertheless, there are numerous days with FWI > 25–30, reaching up to approximately 52, which reflects the presence of episodes of high to extreme danger.

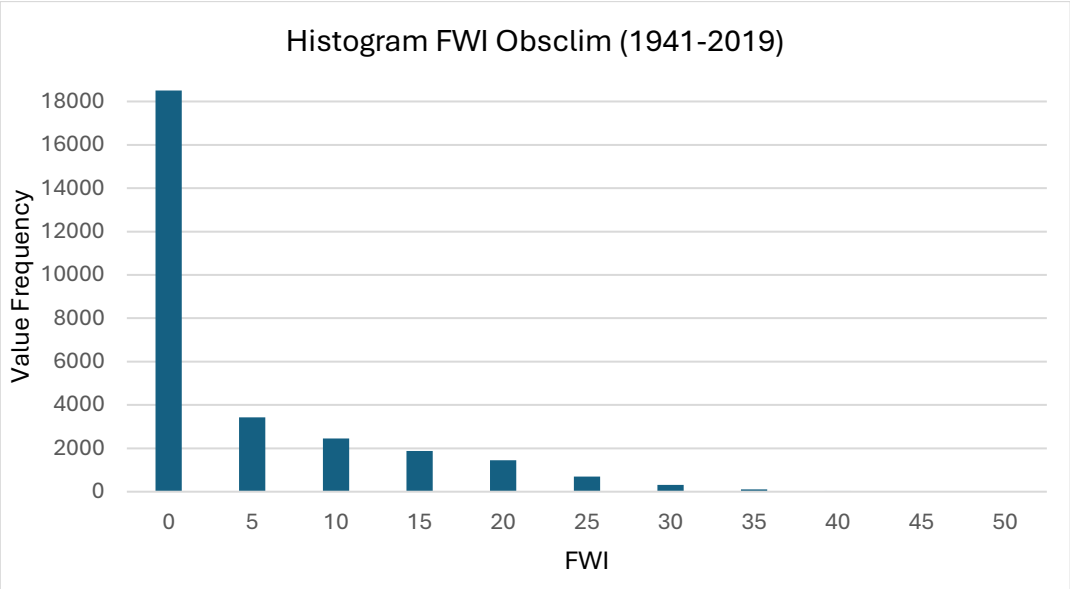

Figure 4.19. Histogram FWI (1941-2019) Obsclim

The 90th and 95th thresholds define the upper tail of the distribution where days with the most significant impact are found. Thus, although the majority of summer days correspond to low to moderate danger, the long right tail of the distribution highlights a small but critical share of days with conditions that favor ignition and rapid wildfire spread.

4.5.1.2 Evolution of FWI exceedance days (90th and 95th percentile)

As a continuation of the overall depiction of the FWI, for each calendar year of 1941–2019 the number of days with FWI higher than two reference thresholds was calculated: the 90th and the 95th percentile of the climatic distribution. The choice of these thresholds follows international practice, where the 95th is widely used as an indication of very high or extreme danger days, while the 90th is often used for the Eastern Mediterranean and Greece, as it better captures persistent hot and dry summer periods.

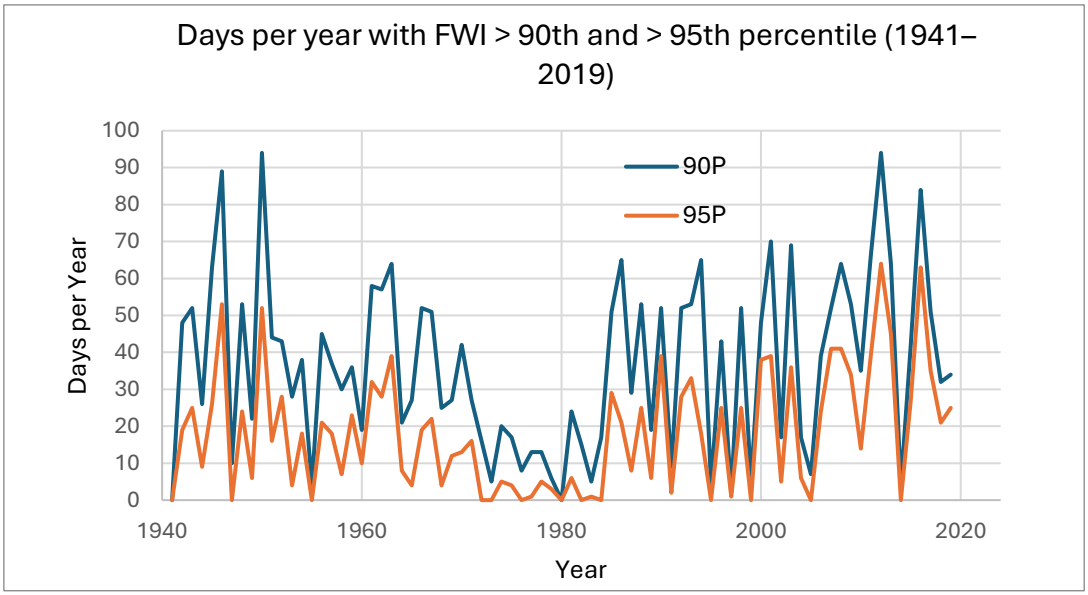

Figure 4.20. Days per Year with FWI > 90th and >95th percentile (1941-2019), Obsclim

Visually, the plot shows intense exceedance frequency at the beginning of the series, particularly in the 1940s, with values exceeding 50–90 days per year for >90th and respectively 20–60 days per year for >95th. Subsequently, from the mid 1950s to the late 1970s, exceedances decrease to low levels, with >95th showing few or even zero days per year. From the mid–late 1980s and especially after 2000 a clear rebound is observed, with >90th more frequently recording dozens of days per year and >95th showing steadily increased but smaller in number exceedances. The decade 2010–2019 stands out with numerous exceedance episodes for both thresholds, recording the highest average values compared to all previous periods.

Table 4.5. Decadal statistics of FWI exceedances above the 90th and 95th percentiles (1941–2019), Obsclim

Period	Years	Average Days >90p	Average Days >95p	Max >90p (year)	Max >95p (year)	% years with ≥30 days >90p	% years with ≥15 days >95p
1941–1959	19	25.6	13.1	63 (1945)	53 (1946)	42%	37%
1960–1979	20	20.0	13.6	64 (1963)	39 (1961)	30%	20%
1980-1999	20	13.6	6.5	65 (1986)	39 (1990)	15%	10%
2000–2009	10	36.4	21.5	70 (2001)	41 (2007)	60%	50%
2010–2019	10	49.6	31.4	94 (2012)	64 (2012)	80%	70%
1941-2019	79	29.0	17.2	94 (2012)	64 (2012)	45%	37%

Overall, the time series of days per year with FWI >90th and >95th percentile depicts high interannual variability but also a clear upward trend from the late 1990s onward. The period 2000–2019 is characterized by distinctly more frequent exceedances compared to previous decades, which is consistent with the warmer and drier summer climatology documented for the Mediterranean. It is emphasized that data before 1979 carry higher uncertainty due to limited observations in the input fields of the index.

4.5.1.3 Daily evolution of the FWI (July–September 2023)

For a comprehensive understanding of the FWI, a plot was created in Python for July, August, and September in which the statistics of this period are displayed (minimum, maximum, mean, 25th–75th percentile). In the plots the wildfire period is highlighted with an orange background.

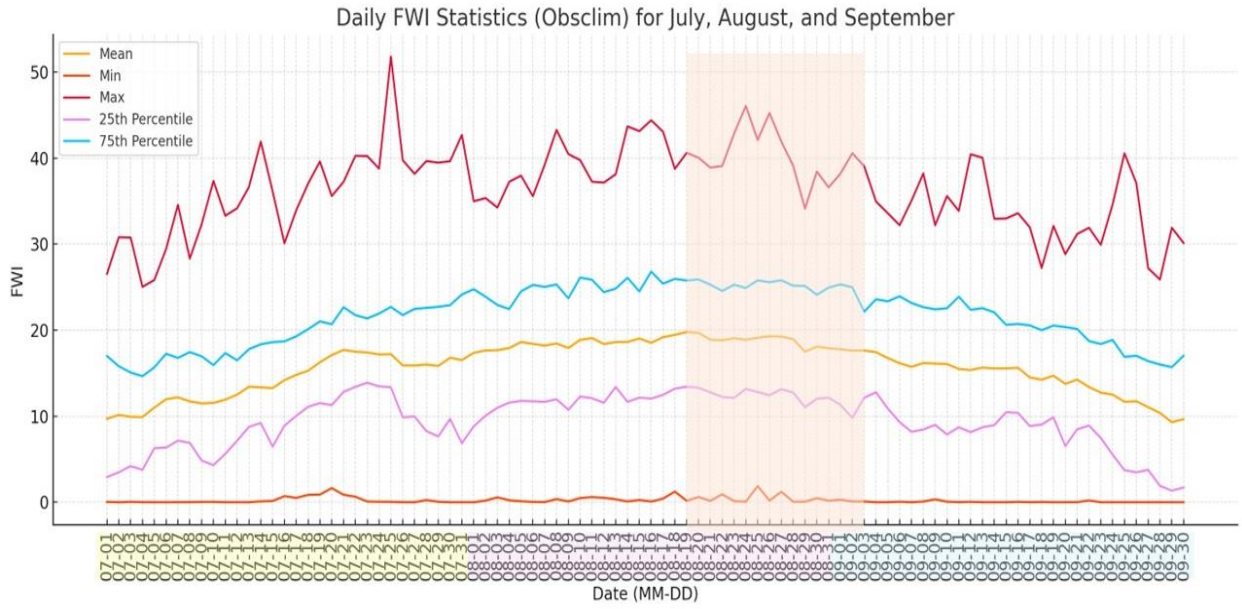

Figure 4.21. FWI Statistics for July–September (1941–2019) based on the obsclim scenario.
The red and orange lines represent the historical maximum and minimum daily values, respectively, while the yellow line shows the average. The blue and purple lines correspond to the 75th and 25th percentiles of the climate distribution. The shaded orange area highlights the fire period in August–September 2023.

In the climatic background of July–September, daily means range approximately from 9.3 to 19.8 (mean value 15.7), the 25th percentile from about 1.3 to 13.9 (mean value 9.4) and the 75th percentile from 14.6 to 26.8 (mean value 21.7). Daily extremes are usually in the range about 0.0–1.9 for minima and 25.0–51.8 for maxima. Overall, the curves increase gradually from July toward mid August and a mild decline follows toward late September. In addition, during 19/8–3/9 the most intense phase of the period is recorded, with the daily mean around 18.6 (range 17.5–19.8), the 75th percentile stabilizing near 25.0 (range 22.1–25.9) and maxima ranging about 34–46, indicating elevated danger.

4.5.2 Counterclim scenario

In the following plots a stepwise interpretation is provided for the variability of each variable that serves as an input to the wildfire danger index, as a brief climatological depiction of the area under this scenario.

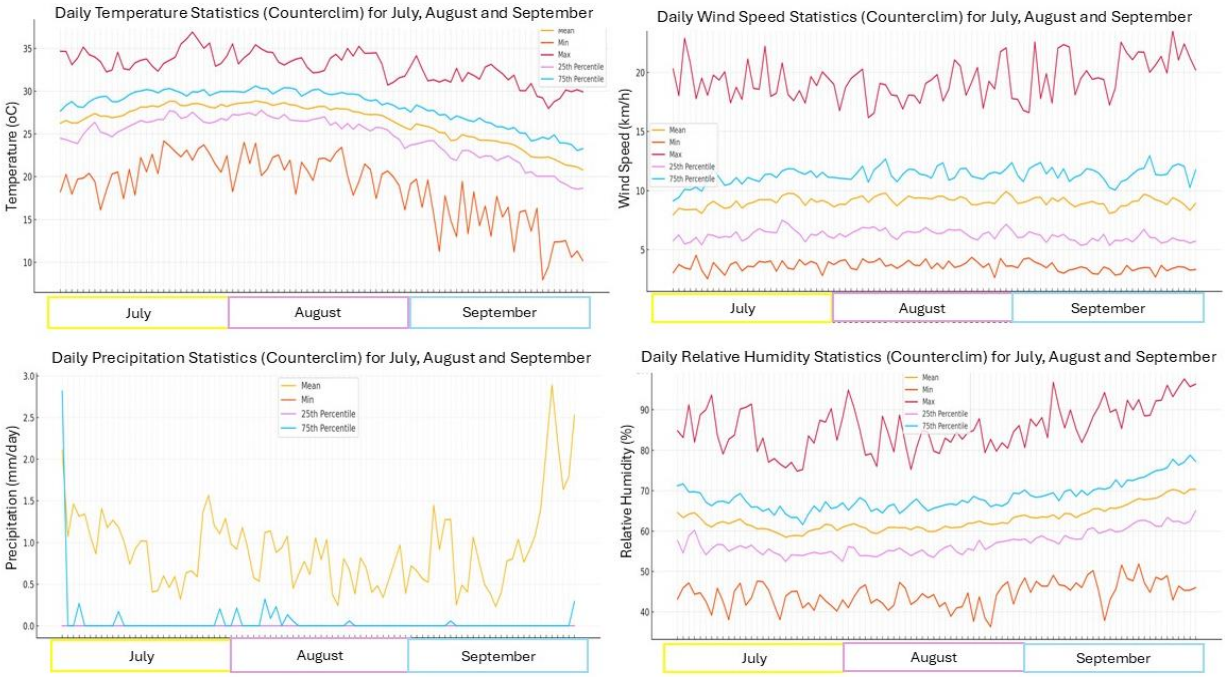

Figure 4.22. FWI Parameters Statistics for July-September period based on Counterclim scenario, (a) Temperature, (b) Wind Speed, (c) Precipitation, (d) Relative Humidity . The red and orange lines represent the historical maximum and minimum daily values, respectively, while the yellow line shows the average. The dashed blue and magenta lines correspond to the 75th and 25th percentiles of the climate distribution. The shaded orange area highlights the fire period in August–September 2023.

Temperature (°C): Daily means range approximately from 20.8 to 28.9 °C (mean value 26.4 °C), the 25th percentile lies at 18.5–27.8 °C (mean value 24.6 °C) and the 75th percentile at 23.1–30.6 °C (mean value 28.3 °C). Daily extremes span 7.95–24.18 °C for minima and 27.96–36.91 °C for maxima. Over the full period there is a mild rise toward early–mid August and a gradual decline to late September, with thermal peaks of limited duration.

Wind (km/h): Daily means range approximately from 7.9 to 9.9 km/h (mean value 9.1 km/h), the 25th percentile at 5.4–7.5 km/h (mean value 6.2 km/h) and the 75th percentile at 9.1–13.0 km/h (mean value 11.3 km/h). Daily extremes are typically 2.5–4.5 km/h for minima and 16.2–23.5 km/h for maxima. The seasonal course shows slight strengthening during August and smooth weakening toward late September, with sporadic surges.

Precipitation (mm/day): Daily means range approximately from 0.2 to 2.9 mm/day (mean value 0.9 mm/day), the 25th percentile is practically 0 mm/day for most of the quarter (mean value 0.00), while the 75th percentile ranges 0.00–2.8 mm/day (mean value 0.05 mm/day) and daily extremes are 0 mm/day for minima.

Relative humidity (%): Daily means range approximately from 58.5 to 70.4% (mean value 62.9%), the 25th percentile at 52.5–65.0% (mean value 57.0%) and the 75th percentile at 61.6–78.8% (mean value 68.5%). Daily extremes span 36.4–51.9% for minima and 74.8–97.6% for maxima. Overall, there is a decreasing tendency from mid July to mid August and a recovery of humidity toward September, consistent with the easing of summer dry–hot conditions.

4.5.2.1 FWI using ISIMIP3a counterclim data

The Fire Weather Index (FWI) was then computed for the study area on a daily basis for

1941–2019, using the counterclim data of the ISIMIP3a program (GSWP3–W5E5 dataset).

The total population of daily FWI values (1941–2019) exhibits a strongly right-skewed distribution. Most days cluster at low values (0–5), with more than 18,000 days in this range, while frequency declines rapidly as the index increases. Despite the dominance of low values, there are non-negligible numbers of days with FWI reaching 40–45 units, reflecting episodes of high to extreme danger. In summary, the descriptive statistics for the period are:

Table 4.6. FWI Statistics, Counterclim

Average	Min	Max	25th percentile (P25)	75th percentile (P75)	90th percentile (P90)	95th percentile (P95)
5.31	3.14e-09	44.96	0.18	8.47	17.27	21.21

In operational terms, days with FWI > ~17 (90th) and especially > ~21 (95th) correspond to high or very high danger within the climatic frame 1941–2019.

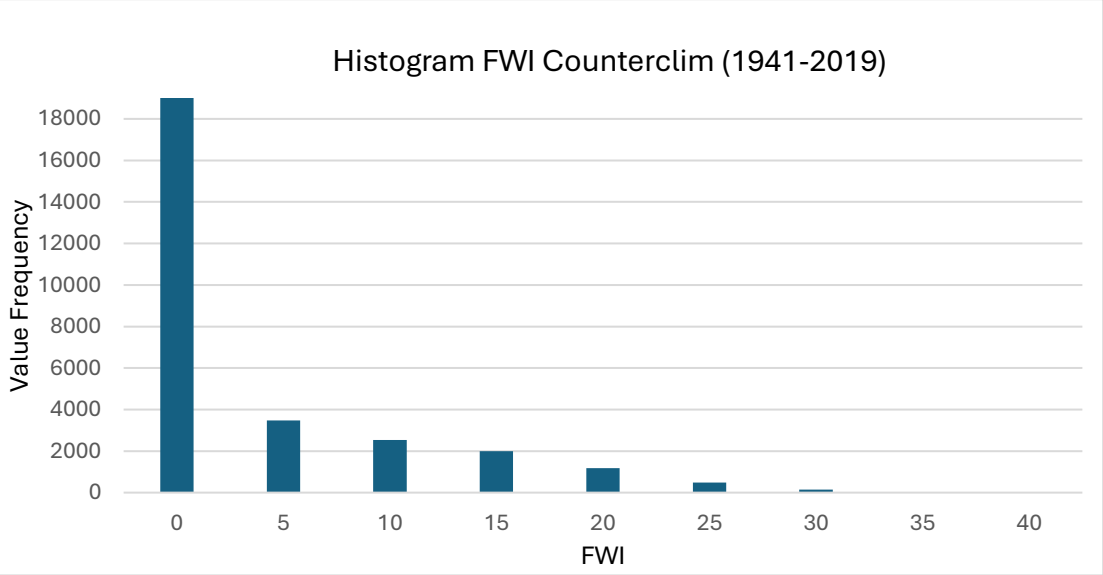

Figure 4.23. Histogram FWI (1941-2019), Counterclim

The presence of a long right tail in the distribution means that, although the majority of days are low danger, there exists a small but critical share of days with very high values that is particularly important for understanding and anticipating large wildfire episodes.

4.5.2.2 Evolution of FWI exceedance days (90th and 95th percentile)

As a continuation of the overall depiction, for each calendar year (1941–2019) the number of days with FWI greater than the 90th and 95th percentile thresholds was calculated. The choice of these thresholds follows international practice, where the 95th is widely used as an indicator of very high or extreme danger days, while the 90th is often useful for the Eastern Mediterranean, capturing more effectively the prolonged hot and dry episodes.

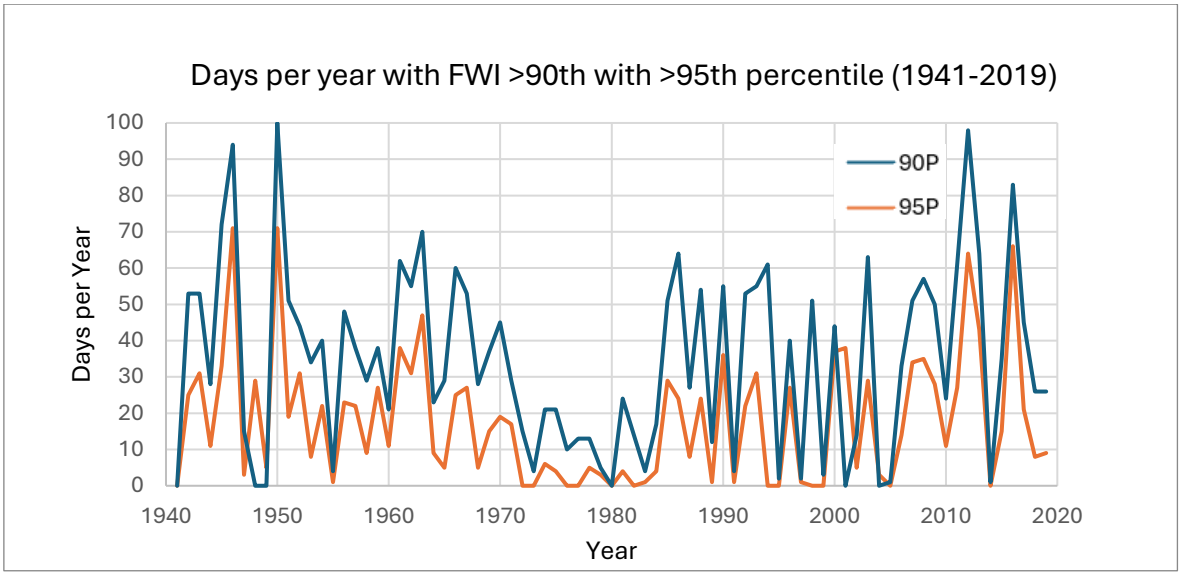

Figure 4.24. Days per Year with FWI > 90th and >95th percentile (1941-2019), Counterclim

The plot highlights high exceedances in the early years of the series, particularly in the 1940s, with >90th reaching above 70–100 days per year and >95th up to 70 days per year (1946–1950). Subsequently, from the mid 1950s to the late 1970s, exceedances drop sharply, with >95th often recording zero or very few days per year. From the mid 1980s a clear rebound appears, peaking in the 2010s, where the mean values of both thresholds are the highest of the series (for example 2012, 2016).

Table 4.7. Decadal statistics of FWI exceedances above the 90th and 95th percentiles (1941–2019), Counterclim

Period	Year	Average Days >90p	Average Days >95p	Max >90p (year)	Max >95p (year)	% Years with ≥30 days >90p	% Years with ≥15 days >95p
1941–1959	19	34.7	19.5	100 (1950)	71 (1950)	63%	53%
1960–1979	20	20.5	11.6	64 (1963)	38 (1961)	30%	25%
1980–1999	20	19.3	8.9	65 (1986)	39 (1990)	28%	18%
2000–2009	10	32.2	19.6	70 (2001)	41 (2007)	55%	45%
2010–2019	10	44.0	28.5	98 (2012)	64 (2012)	75%	70%
1941–2019	79	30.1	16.4	100 (1950)	71 (1950)	49%	42%

Overall, the time series reveals high interannual variability and an upward trend after 2000, with 2010–2019 standing out for the greatest frequency and intensity of exceedances. The two signals (90p and 95p) follow a parallel trajectory, years with high >90p exceedances are almost always accompanied by corresponding >95p exceedances, but in smaller absolute numbers, as expected. As in previous sections it is noted that data prior to 1979 carry higher uncertainty due to limited observations in the input fields of the index.

4.5.2.3 Daily evolution of the FWI (July–September)

For a comprehensive understanding of the FWI, a plot was created in Python for July, August, and September in which the statistics of this period are displayed (minimum, maximum, mean, 25th–75th percentile). In the plots the wildfire period is highlighted with an orange background.

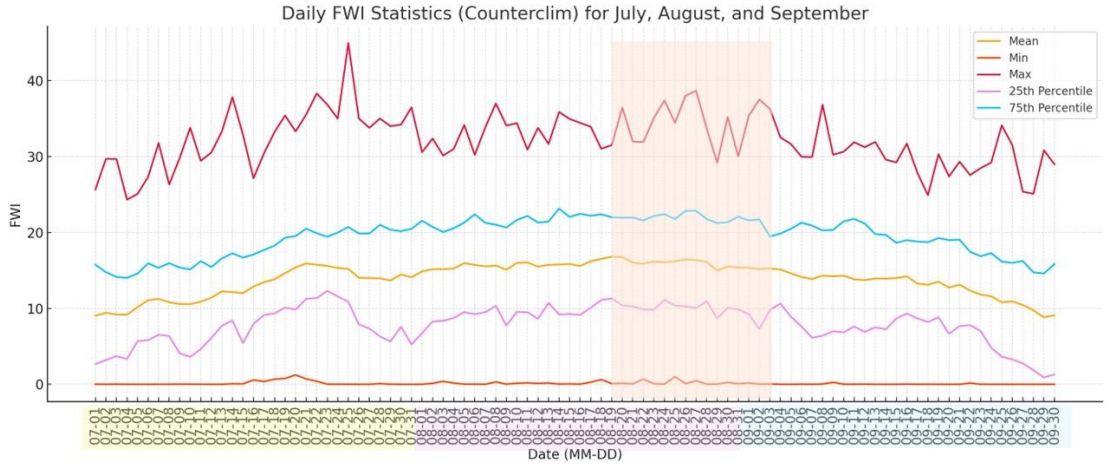

Figure 4.25. FWI Statistics for July–September (1941–2019) based on the counterclim scenario.
The red and orange lines represent the historical maximum and minimum daily values, respectively, while the yellow line shows the average. The blue and purple lines correspond to the 75th and 25th percentiles of the climate distribution.The shaded orange area highlights the fire period in August–September 2023.

In the July–September climatic background, daily means range approximately from 8.8 to 16.8 (mean value 13.9), the 25th percentile from 0.9 to 12.3 (mean value 7.8) and the 75th percentile from 14.0 to 23.2 (mean value 19.5). Daily extremes lie in the range about 0.0–1.2 for minima and 24.3–45.0 for maxima, with clear day-to-day variability. Overall, the course shows a gradual increase from July toward mid August and a mild decline toward late September. During 19 August – 3 September the highest mean values of the period are observed (about 15–17), with the 75th percentile stabilizing near 20–23 and maxima ranging 29–39, depicting a phase of elevated wildfire danger.

4.5.3 Comparison of FWI distributions: obsclim vs counterclim (1941–2019)

The comparison of the two scenarios using identical 5-unit bins (FWI → 5–55) shows a clear shift of the distribution toward higher values in obsclim relative to counterclim. This is evident both in the double histogram and in the “difference” plot (obsclim minus counterclim): low bins (FWI ≤ 20) are more frequent in counterclim, while from FWI = 25 and above obsclim consistently exhibits more days.

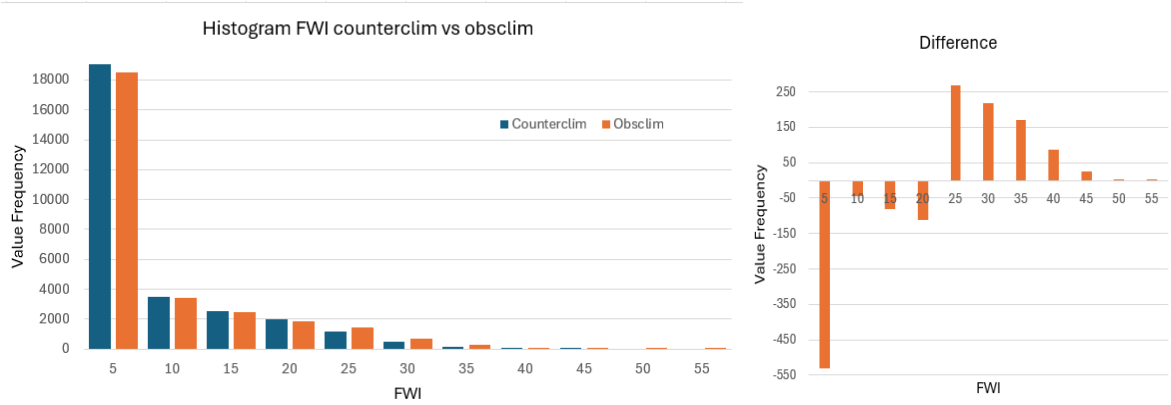

Figure 4.26. Histogram Compariton FWI: Counterclim vs Obsclim (1941-2019) and Difference figure

From the plots it follows that in the low bins counts are higher in counterclim (for example FWI = 5: 19,036 versus 18,504 → obsclim − counterclim = −532 days, FWI = 15: −81 days, FWI = 20: −112). In contrast, from bin 25 upward the differences become positive in favor of obsclim and increase systematically with FWI level: FWI = 25: +269 days, FWI = 30: +217, FWI = 35: +170. At very high values the difference is striking: FWI = 40: +86 days (obsclim ≈ 4.6× counterclim), FWI = 45: +25, while occurrences at FWI = 50–55 are recorded only in obsclim (counterclim = 0, appearance from a zero base). Overall, obsclim strengthens the mid–high bins and extends the right tail of the distribution, which implies a greater probability of high and very high danger days.

Table 4.8. Absolute and relative changes in the frequency of FWI ≥35 events between Obsclim and Counterclim

FWI bin	Counterclim (count)	Obsclim (count)	Δ count	Δ %
25	1 175	1 444	+269	+22.9%
30	477	694	+217	+45.5%
35	140	310	+170	+121.4%
40	24	110	+86	+358.3%
45	1	26	+25	+2500%
50	0	2	+2	From zero base
55	0	1	+1	From zero base

(Δcount = Obsclim − Counterclim, Δ% relative to Counterclim, for zero base the percent is not defined)

The FWI distribution in obsclim is clearly shifted toward higher values compared with counterclim, fewer very low-index days and more days in mid–high and very high bins (≥25). This enhancement of high bins, especially from 35 and above, documents increased frequency of hazardous fire-weather conditions in obsclim, fully consistent with

the expected difference between a scenario with anthropogenic influences (obsclim) and one without them (counterclim).

4.6 Shift of FWI percentiles during the Evros wildfire

For the days of the Evros wildfire (19/8–3/9/2023), the corresponding FWI values from Copernicus (ERA5) were extracted. Each value was placed in the historical distribution (1940–2024) to identify its percentile rank. Then, for the same percentile the equivalent FWI value was retrieved from the obsclim scenario (with anthropogenic influences). Finally, this value was mapped to the counterclim distribution (without anthropogenic influences) to assess how rare the same conditions would have been in a "hypothetical" climate without human-induced warming.

Table 4.9. Calculation of FWI percentiles for the wildfire days in Evros (19/8-3/9/2023) based on Copernicus, Obsclim, and Counterclim.

Date	FWI Copernicus	Copernicus Percentile	Equivalent FWI value in Obscilm	Counterclim Percentile
19/8/2023	54.917	0.985	30.020	0.994
20/8/2023	62.490	0.995	34.787	0.999
21/8/2023	84.535	0.999	46.061	>1
22/8/2023	76.695	0.999	42.059	0.999
23/8/2023	60.793	0.993	33.736	0.998
24/8/2023	47.242	0.963	25.377	0.979
25/8/2023	46.239	0.960	24.859	0.977
26/8/2023	51.813	0.978	28.036	0.989
27/8/2023	50.240	0.973	27.600	0.987
28/8/2023	35.282	0.899	18.948	0.921
29/8/2023	33.405	0.884	17.801	0.907
30/8/2023	32.863	0.880	17.455	0.902
31/8/2023	33.085	0.881	17.576	0.904
1/9/2023	34.247	0.891	18.321	0.913
2/9/2023	49.945	0.972	26.893	0.986
3/9/2023	56.350	0.987	30.914	0.996

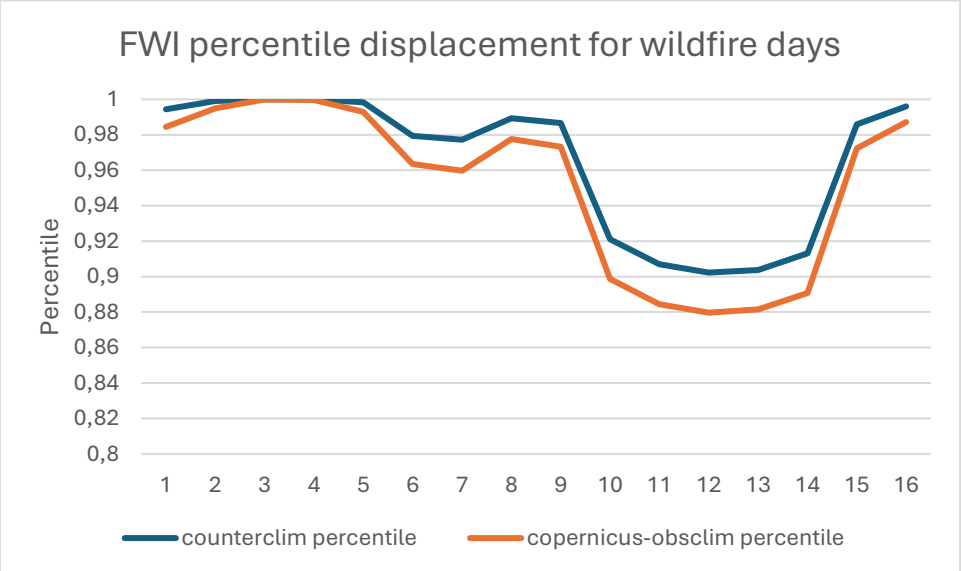

Figure 4.27. FWI percentile displacement for wildfire days.
The orange line represents the obsclim percentiles for the days of the event and the blue line the counterclim percentiles.

The analysis shows that during the wildfire all daily FWI values were located at the upper tail of the historical distribution. Within the observed (obsclim) climate these values correspond to percentiles from about 0.88 to 0.99, already classified as very high or extreme. However, when the same values are “translated” into the counterclim, their rarity increases even further. On at least six out of the sixteen days the values reach the ≥99th percentile, with notable examples on 22/8, where the value touches the absolute edge of the distribution, and on 21/8, where it even exceeds it. Even the “lowest” values of the period (for example 28/8–31/8) remain above the 88th–90th percentile, confirming that there was not a single day with moderate or low danger.

The percentile shift plot clearly illustrates this transformation. The counterclim curve is consistently higher than the obsclim one, with the largest gap occurring in the middle of the episode (24–30/8). This means that the same physical FWI values, which under the current climate framework appear as “very high,” would be nearly absent or impossible under the hypothetical no-anthropogenic scenario.

The comparison demonstrates that the extreme conditions prevailing in Evros in August–September 2023 cannot be explained solely by natural climate variability. On the contrary, anthropogenic climate change has shifted the FWI distribution toward higher values, making conditions highly probable that under “counterclim” would fall within the upper 1% or even the absolute maximum. In other words, without human influence, the occurrence of such values would have been extremely rare, if not practically impossible. This substantiates that anthropogenic warming was a critical factor that amplified and enabled the onset and intensity of the specific episode.

5. Conclusion

This thesis aimed to investigate the major wildfire that occurred in Evros in 2023 and to assess its relationship with climate change, using both satellite and climate datasets. The analysis was based on ERA5 data from the Copernicus Climate Data Store, the ISIMIP3a datasets (obsclim and counterclim), as well as burned area products such as MODIS MCD64A1, Copernicus EMS Rapid Mapping, and EFFIS/GWIS. In addition, official data from the Hellenic Fire Service and reports from European and international organizations were incorporated.

The results highlight several critical findings. First, the Evros wildfire was the largest recorded event in the European Union, with a burned area exceeding 94,000 ha, a duration of at least 16 days, and severe socio-economic and environmental impacts. The spatial and temporal mapping through Rapid Mapping products illustrated the progressive expansion of the fire front and its successive phases of spread, confirming the multifactorial character of the disaster.

The analysis of the Fire Weather Index (FWI) demonstrated that during the wildfire period, daily values consistently reached the highest risk categories, far exceeding historical percentiles (>90p and >95p). These values were directly linked to extreme weather conditions, such as high temperatures, low humidity, and strong winds. This confirms that

the episode constitutes a typical example of “high fire danger conditions” as defined in the international literature.

When examining the long-term series of FWI (1940–2024), the comparison between the two reference periods 1961–1990 and 1991–2020 revealed a clear upward shift in the distribution. Lower values became less frequent, while medium to high bins gained prominence. Importantly, very high or extreme FWI levels that were practically absent in the earlier 30-year period appeared systematically in the more recent one. This transition confirms that high-risk fire days have become more likely in the current climate.

The time series of exceedance days above the 90th and 95th percentiles provided further evidence. The early part of the record showed extremely high values, but a significant decline followed until the 1970s. Since the 1980s, and especially after 2000, exceedance days have increased again, with frequent peaks after 2010. This demonstrates not only the variability of the Mediterranean climate but also a consistent upward trend in recent decades, consistent with warming and drying conditions.

The comparison between the ISIMIP3a obsclim and counterclim scenarios further strengthened these findings. The obsclim simulations, which incorporate anthropogenic influence, consistently produced more days with FWI in the high and very high bins, while counterclim remained concentrated in lower values. Particularly at thresholds above 35 or 40, the differences were striking, with obsclim showing appearances of values that were virtually absent in counterclim. This highlights the role of human-induced warming in shifting the entire FWI distribution toward higher risks.

Finally, the analysis of percentile shifts during the fire episode in Evros (19 August–3 September 2023) offers the most compelling attribution evidence. Daily FWI values from Copernicus were already among the highest of the historical record, often above the 90th and 95th percentiles. However, when these values were translated into the counterclim scenario, their rarity increased dramatically, with at least six days reaching or exceeding the 99th percentile. In practical terms, conditions that are already extreme in the observed climate would have been nearly impossible without anthropogenic influence. This means that the devastating Evros wildfire cannot be explained solely by natural variability, but instead reflects a climate system where human-driven warming has made such extremes far more probable.

In conclusion, the study shows that the Evros wildfire was not an isolated or purely natural disaster. The integration of observational and modeled datasets demonstrated that anthropogenic climate change has substantially increased the likelihood and intensity of extreme fire weather conditions in Greece. Future fire seasons are expected to bring even more frequent and severe events, underscoring the need for robust adaptation strategies, enhanced prevention, and the incorporation of climate projections into civil protection planning.

6. References

[1] Balsamo, G., Albergel, C., Beljaars, A., Boussetta, S., Brun, E., Cloke, H., Dee, D., Dutra, E., Muñoz-Sabater, J., Pappenberger, F., de Rosnay, P., Stockdale, T., & Vitart, F. (2018). Satellite and ground-based observations for reanalysis evaluation: A review. *Reviews of Geophysics, 56(4),* 1034–1070. https://doi.org/10.1029/2018RG000590

[2] BirdLife International. (n.d.). *National Park of Dadia–Lefkimi–Soufli forest.* BirdLife Data Zone. https://datazone.birdlife.org/site/factsheet/national-park-of-dadia-lefkimi-soufli-forest [09/2025]

[3] Catsadorakis, G., & Källander, H. (Eds.). (2010). *The Dadia–Lefkimi–Soufli Forest National Park, Greece: Biodiversity, management and conservation.* WWF Greece.

[4] Copernicus Atmosphere Monitoring Service (CAMS). (2023). August wildfires ravage northern & central Greece. https://atmosphere.copernicus.eu/august-wildfires-ravage-northern-central-greece [09/2025]

[5] Copernicus Atmosphere Monitoring Service (CAMS). (2023). 2023: A year of intense global wildfire activity. https://atmosphere.copernicus.eu/2023-year-intense-global-wildfire-activity [09/2025]

[6] Copernicus Atmosphere Monitoring Service (CAMS). (2024). State of Wildfires 2023–24: CAMS data supports assessment. https://atmosphere.copernicus.eu/state-wildfires-2023-24-cams-data-supports-assessment [09/2025]

[7] Copernicus Climate Data Store (CDS). (n.d.). *ERA5 reanalysis: single levels — dataset page.* https://cds.climate.copernicus.eu/cdsapp#!/dataset/reanalysis-era5-single-levels [08/2025]

[8] Copernicus Emergency Management Service (CEMS). (2023). *EMSR686 — Wildfire in East Macedonia, Greece (Rapid Mapping products).* https://rapidmapping.emergency.copernicus.eu/EMSR686/download [08/2025]

[9] Copernicus Emergency Management Service (CEMS). (2023). *TECHNICAL REPORT – EMSN166: Post-Wildfire damage assessment in East Macedonia, Greece (Issue 1.0), 18 Dec 2023.* https://civilprotection.gov.gr/sites/default/files/2024-02/EMSN166_Technical_Report_v01.pdf [09/2025]

[10] Dupuy, J.-L., Fargeon, H., Martin-StPaul, N., Pimont, F., Ruffault, J., Guijarro, M., Hernando, C., Madrigal, J., Fernandes, P., & Vega, J. A. (2020). Climate change impact on future wildfire danger and activity in southern Europe: A review. *Annals of Forest Science, 77,* 35. https://doi.org/10.1007/s13595-020-00933-5

[11] ECMWF. (n.d.). *ERA5: Documentation of model description & assimilation (Knowledge Base).* https://confluence.ecmwf.int/display/CKB/ERA5 [09/2025]

[12] Encyclopaedia Britannica. (n.d.). *Maritsa River.* https://www.britannica.com/place/Maritsa-River [08/2025]

[13] European Commission — Copernicus. (n.d.). *Copernicus overview.* https://copernicus.eu [09/2025]

[14] European Environment Agency (EEA) / JRC–EFFIS. (2024). Wildfires: 2023 among the worst in the EU in this century (10 April 2024). https://joint-research-

centre.ec.europa.eu/jrc-news-and-updates/wildfires-2023-among-worst-eu-century-2024-04-10_en [08/2025]

[15] Frieler, K., Lange, S., Piontek, F., Reyer, C. P. O., Schewe, J., Warszawski, L., Zhao, F., Chini, L., Denvil, S., Emanuel, K., Geiger, T., Halladay, K., Hurtt, G., Mengel, M., Murakami, D., Ostberg, S., Popp, A., Riva, R., Stevanovic, M., … Schultze, M. (2017). Assessing the impacts of 1.5 °C global warming — simulation protocol of ISIMIP2b. *Geoscientific Model Development, 10,* 4321–4345. https://doi.org/10.5194/gmd-10-4321-2017

[16] Giorna-García, A., Lucas-Borja, M. E., Plaza-Álvarez, P. A., Gómez-Sánchez, E., González-Romero, J., & Cerdà, A. (2021). Effectiveness of post-fire soil erosion mitigation treatments: A meta-analysis. *Earth-Science Reviews, 217,* 103611. https://doi.org/10.1016/j.earscirev.2021.103611

[17] Google Earth Engine Developers. (n.d.). *ERA5-Land hourly — dataset catalog page.* https://developers.google.com/earth-engine/datasets/catalog/ECMWF_ERA5_LAND_HOURLY [08/2025]

[18] Gould, C. F., Anenberg, S. C., Balmes, J. R., Dominici, F., Liu, J. C., & Moore, R. (2023). Health Effects of Wildfire Smoke Exposure. *Annual Review of Medicine, 74,* 277–290. https://doi.org/10.1146/annurev-med-042921-013112

[19] Hempel, S., Frieler, K., Warszawski, L., Schewe, J., & Piontek, F. (2013). A trend-preserving bias correction — the ISI-MIP approach. *Earth System Dynamics, 4,* 219–236. https://doi.org/10.5194/esd-4-219-2013

[20] Hersbach, H., Bell, B., Berrisford, P., Biavati, G., Horányi, A., Muñoz-Sabater, J., Nicolas, J., Peubey, C., Radu, R., Rozum, I., Schepers, D., Simmons, A., Soci, C., Abdalla, S., Abellan, X., Balsamo, G., Bechtold, P., Bishop, C., Buontempo, C., … Thépaut, J.-N. (2020). The ERA5 global reanalysis. *Quarterly Journal of the Royal Meteorological Society, 146(730),* 1999–2049. https://doi.org/10.1002/qj.3803

[21] Johnson, M. M., & Garcia-Menendez, F. (2022). Uncertainty in Health Impact Assessments of Smoke From a Wildfire Event. *GeoHealth, 6(1),* e2021GH000526. https://doi.org/10.1029/2021GH000526

[22] Jones, M. W., Kelley, D. I., Burton, C. A., Di Giuseppe, F., Barbosa, M. L. F., Brambleby, E., Hartley, A. J., Lombardi, A., Mataveli, G., McNorton, J. R., Spuler, F. R., Wessel, J. B., Abatzoglou, J. T., Anderson, L. O., Andela, N., Archibald, S., Armenteras, D., Burke, E., Carmenta, R., Chuvieco, E., Clarke, H., Doerr, S. H., Fernandes, P. M., Giglio, L., Hamilton, D. S., Hantson, S., Harris, S., Jain, P., Kolden, C. A., Kurvits, T., Lampe, S., Meier, S., New, S., Parrington, M., Perron, M. M. G., Qu, Y., Ribeiro, N. S., Saharjo, B. H., San-Miguel-Ayanz, J., Shuman, J. K., Tanpipat, V., van der Werf, G. R., Veraverbeke, S., & Xanthopoulos, G. (2024). State of Wildfires 2023–2024. *Earth System Science Data, 16,* 3601–3685. https://doi.org/10.5194/essd-16-3601-2024

[23] Karali, A., Giannakopoulos, C., Founda, D., Hatzaki, M., Roussos, A., Papadopoulos, A., & Good, P. (2014). Sensitivity and evaluation of the Canadian Fire Weather Index in Greece. *Natural Hazards and Earth System Sciences, 14(1),* 17–33. https://doi.org/10.5194/nhess-14-17-2014

[24] Kaskaoutis, D. G., Kambezidis, H. D., Nastos, P. T., Kosmopoulos, P. G., Solomos, S., & Kontoes, C. (2024). Impact of peri-urban forest fires on air quality and aerosol

properties in Athens (Aug 2021). *Science of the Total Environment, 924,* 170140. https://doi.org/10.1016/j.scitotenv.2024.170140

[25] Katich, J. M., Murphy, D. M., Yu, P., Toon, O. B., Rollins, A. W., Bui, T. P., Dollner, M., Weinzierl, B., Schmidt, A., & Brock, C. A. (2023). Pyrocumulonimbus affect average stratospheric aerosol loading. *Science, 381(6659),* eadd3101. https://doi.org/10.1126/science.add3101

[26] Key Biodiversity Areas Partnership. (n.d.). *National Park of Dadia–Lefkimi–Soufli forest (KBA ID 987).* https://www.keybiodiversityareas.org/site/factsheet/987 [09/2025]

[27] Lange, S. (2019). WFDE5 over land merged with ERA5 over the ocean (W5E5), v1.0. *GFZ Data Services.* https://doi.org/10.5880/pik.2019.023

[28] Lange, S. (2020). ISIMIP3a bias-adjusted input data (GSWP3–W5E5). *GFZ Data Services.* https://doi.org/10.5880/PIK.2020.004

[29] Lange, S. (2021). ISIMIP3a bias-adjusted climate input data for impact modeling: a detailed description. *Earth System Science Data Discussions.* https://doi.org/10.5194/essd-2021-123

[30] Lange, S., Müller Schmied, H., Gerten, D., Glotter, M., Haddeland, I., Heinke, J., Konzmann, M., Moyer, E. J., Müller, C., Oki, T., Reyer, C. P. O., Stacke, T., Tessler, Z. D., & Warszawski, L. (2020). The Inter-Sectoral Impact Model Intercomparison Project (ISIMIP): climate input data. *Earth System Science Data, 12,* 1511–1543. https://doi.org/10.5194/essd-12-1511-2020

[31] Meteoblue. (n.d.). *Climate models and global reanalysis comparison (ERA5 overview).* https://content.meteoblue.com/en/meteoscience/era5 [09/2025]

[32] Mitsopoulos, I., Mallinis, G., Dimitrakopoulos, A., Xanthopoulos, G., Eftychidis, G., & Goldammer, J. G. (2020). Vulnerability of peri-urban and residential areas to landscape fires in Greece: Evidence by wildland–urban interface data. *Data in Brief, 31,* 106025. https://doi.org/10.1016/j.dib.2020.106025

[33] Modugno, S., Balzter, H., Cole, B., & Borrelli, P. (2016). Mapping regional patterns of large forest fires in WUI areas in Europe. *Journal of Environmental Management, 172,* 112–126. https://doi.org/10.1016/j.jenvman.2016.02.013

[34] Muñoz-Sabater, J., Dutra, E., Agustí-Panareda, A., Albergel, C., Arduini, G., Balsamo, G., Boussetta, S., Choulga, M., Harrigan, S., Hersbach, H., Martens, B., Miralles, D. G., Piles, M., Rodríguez-Fernández, N. J., Zsoter, E., Buontempo, C., & Thépaut, J.-N. (2021). ERA5-Land: A state-of-the-art global reanalysis dataset for land applications. *Earth System Science Data, 13(9),* 4349–4383. https://doi.org/10.5194/essd-13-4349-2021

[35] NCAR/UCAR Climate Data Guide. (n.d.). *ERA5: ECMWF Reanalysis v5.* https://climatedataguide.ucar.edu/climate-data/era5-reanalysis [08/2025]

[36] Osswald, T., Giannaros, T. M., Melas, D., & Zanis, P. (2023). Effects of the wildfires in August 2021 on the air quality of Athens: numerical simulation. *International Journal of Wildland Fire, 32(6),* 605–620. https://doi.org/10.1071/WF22083

[37] Poupkou, A., Melas, D., Ziomas, I. C., & Symeonidis, P. (2011). Climatology and variability of the Etesian winds over the Aegean. *Theoretical and Applied Climatology, 106(3–4),* 359–374. https://doi.org/10.1007/s00704-011-0436-5

[38] Ramsar Convention Secretariat. (n.d.). *Evros Delta (Ramsar Site No. 54).* Ramsar Sites Information Service. https://rsis.ramsar.org/ris/54 [09/2025]

[39] Ruffault, J., Curt, T., Moron, V., Trigo, R. M., Mouillot, F., Koutsias, N., Pimont, F., Martin-StPaul, N. K., Barbero, R., Dupuy, J.-L., Russo, A., Belhadj-Khedher, C., & Vincente-Serrano, S. M. (2018). Extreme wildfire events linked to global-change-type droughts in the northern Mediterranean. *Natural Hazards and Earth System Sciences, 18,* 847–856. https://doi.org/10.5194/nhess-18-847-2018

[40] Ruffault, J., Curt, T., Moron, V., Trigo, R. M., Mouillot, F., Koutsias, N., Pimont, F., Martin-StPaul, N. K., Barbero, R., Dupuy, J.-L., Russo, A., Belhadj-Khedher, C., & Vincente-Serrano, S. M. (2020). Increased likelihood of heat-induced large wildfires in the Mediterranean Basin. *Scientific Reports, 10,* 13790. https://doi.org/10.1038/s41598-020-70069-z

[41] Shakesby, R. A. (2011). Post-wildfire soil erosion in the Mediterranean: Review and future research directions. *Earth-Science Reviews, 105(1–2),* 71–100. https://doi.org/10.1016/j.earscirev.2011.01.001

[42] Soci, C., Hersbach, H., Muñoz-Sabater, J., Buontempo, C., & Thépaut, J.-N. (2024). Assessing uncertainties in early ERA5 decades using assimilation diagnostics. *Earth System Science Data* (in press).

[43] Taylor, S. W., & Alexander, M. E. (2006). Science, technology, and human factors in fire danger rating: the Canadian experience. *International Journal of Wildland Fire, 15(1),* 121–135. https://doi.org/10.1071/WF05021

[44] Tyrlis, E., & Lelieveld, J. (2013). Climatology and dynamics of the summer Etesian winds over the eastern Mediterranean. *Journal of the Atmospheric Sciences, 70(11),* 3374–3396. https://doi.org/10.1175/JAS-D-13-035.1

[45] Visit Greece (GNTO). (n.d.). *Samothrace.* https://www.visitgreece.gr/islands/north-aegean-islands/samothrace/ [09/2025]

[46] WWF Greece. (n.d.). *Dadia National Park.* https://www.wwf.gr/en/our_work/nature/terrestrial/programmes/dadia_national_park/ [09/2025]

[47] WWF Greece. (2024). *Learning from Evros Fire – Executive Summary.* https://wwfeu.awsassets.panda.org/downloads/evroslessonslearned_exsummary.pdf [09/2025]

[48] Αντωνιάδης, Γ. (2018). *Υδρογεωλογία: Θεωρία και εφαρμογές.* Εκδόσεις Τζιόλα, Θεσσαλονίκη.

[49] Βαβύλης, Δ. (2015). *Μετεωρολογία και Κλιματολογία.* Εκδόσεις Ζήτη, Θεσσαλονίκη.

[50] Γεωργίου, Α. (2017). *Δασικές Πυρκαγιές: Θεωρία και αντιμετώπιση.* Εκδόσεις Σταμούλη, Αθήνα.

[51] Δασαρχείο Σουφλίου. (2023). Ανακοίνωση σχετικά με την εξέλιξη της πυρκαγιάς στη Δαδιά. https://dasarxeio.com [08/2025]

[52] Δημητρακόπουλος, Α. (2002). *Δασική Οικολογία και Προστασία Δασών.* Εκδόσεις Ζήτη, Θεσσαλονίκη.

[53] Εθνικό Αστεροσκοπείο Αθηνών (ΕΑΑ). (2023). Αναφορά για την πυρκαγιά στον Έβρο. *meteo.gr* [09/2025]

[54] ΕΛΣΤΑΤ. (2022). *Μόνιμος πληθυσμός κατά περιφερειακή ενότητα.* https://www.statistics.gr [09/2025]

[55] ΕΜΥ. (2023). Δελτία καιρού για την περίοδο Αυγούστου 2023. https://www.emy.gr [09/2025]

[56] Κακαράς, Γ. (2021). *Κλιματική Αλλαγή και Περιβάλλον.* Εκδόσεις Σάκκουλα, Αθήνα.

[57] Καραβέλας, Γ. (2023). Ανακοίνωση WWF Ελλάς για την πυρκαγιά στον Έβρο. https://www.wwf.gr [09/2025]

[58] Κατσούλας, Χ. (2020). *Δασική Διαχείριση και Πυροπροστασία.* Εκδόσεις Παπασωτηρίου, Αθήνα.

[59] Κέντρο Προστασίας Δασών & Φυσικού Περιβάλλοντος (ΚΠΔΦΠ). (2023). Έκθεση για την πυρκαγιά στη Δαδιά. https://www.kpdf.gr [08/2025]

[60] Μανιάτης, Γ. (2019). *Μετεωρολογικοί Δείκτες και Εφαρμογές στην Πυροπροστασία.* Εκδόσεις Τζιόλα, Θεσσαλονίκη.

[61] Μηλιώνης, Ι. (2016). *Κλιματική Μεταβλητότητα στην Ελλάδα.* Εκδόσεις Σταμούλη, Αθήνα.

[62] Παπαδόπουλος, Κ. (2015). *Υδρολογία και Διαχείριση Υδατικών Πόρων.* Εκδόσεις Σταμούλη, Αθήνα.

[63] Περιφέρεια Ανατολικής Μακεδονίας–Θράκης. (2023). Σχέδιο Πολιτικής Προστασίας για την πυρκαγιά στον Έβρο. https://www.pamth.gov.gr [08/2025]

[64] Πυροσβεστικό Σώμα Ελλάδας. (2023). Ανακοίνωση για επιχειρησιακή διαχείριση της πυρκαγιάς στον Έβρο. https://www.fireservice.gr [09/2025]

[65] Σαχίνης, Π. (2020). *Δασικές Πυρκαγιές και Κλιματική Αλλαγή στην Ελλάδα.* Εκδόσεις Τζιόλα, Θεσσαλονίκη.

[66] Σκουρής, Α. (2018). *Μετεωρολογικά Συστήματα και Κλιματικές Εφαρμογές.* Εκδόσεις Ζήτη, Θεσσαλονίκη.

[67] Τσιγαρίδης, Κ. (2024). Σημειώσεις Διάλεξης για τα αερολύματα και τις πυρκαγιές. Columbia University/ΠΚ (αδημοσίευτο διδακτικό υλικό).

[68] Φιλιππίδης, Χ. (2014). *Γεωλογία της Ελλάδας.* Εκδόσεις Σταμούλη, Αθήνα.

[69] Χατζηθεοδώρου, Θ. (2022). *Υδρολογικά Συστήματα και Περιβαλλοντικές Επιπτώσεις.* Εκδόσεις Παπασωτηρίου, Αθήνα.

Appendix

Table A1. Temperature daily statistics (JAS) – ERA5 (°C) (Figure 4.10.)

Month	Day	Max	Min	Mean	25th Percentile	75th Percentile	2023
7	1	35.59487	17.65143	27.31724	25.7225	29.01274	28.30614
7	2	34.85493	19.37694	27.39951	26.00676	29.00938	27.4423
7	3	32.82935	18.27754	27.25275	25.62188	29.49252	28.84034
7	4	32.92291	19.58556	27.19894	25.53127	29.26913	30.15547
7	5	33.86667	21.61765	27.90042	26.02267	29.13807	30.74813
7	6	35.49415	19.26253	28.04955	26.5929	29.31967	31.11784
7	7	34.30927	22.59637	28.27862	26.69382	29.85553	29.71523
7	8	33.38254	15.82573	27.79301	26.26865	30.24247	27.81777
7	9	34.58899	15.23001	27.85588	25.98135	30.3287	28.29515
7	10	35.28139	18.90517	27.82683	26.12614	29.39655	30.10544
7	11	34.04704	22.31858	27.94626	26.25249	29.50983	31.04984
7	12	33.94949	22.90944	28.23293	26.81944	29.62688	32.17358
7	13	34.18341	22.76626	28.62787	27.3399	29.99921	33.03846
7	14	34.29433	19.61104	28.60252	27.28592	29.7084	33.89011
7	15	34.05777	23.78147	28.96794	27.50667	30.33395	32.62257
7	16	34.76505	20.5563	28.99533	27.49911	30.85569	31.8913
7	17	35.53872	23.81902	29.20071	27.51572	30.7701	32.20284
7	18	36.53695	21.15386	28.99461	27.60312	30.3357	32.6367
7	19	35.5937	22.82156	29.09009	27.73592	30.58445	33.12909
7	20	33.8537	21.44609	29.06809	27.81264	30.30021	32.99972
7	21	33.95323	22.33221	29.18425	28.19674	30.46802	33.48058
7	22	34.92613	21.47123	29.15847	27.62988	30.69744	32.87105
7	23	36.58157	23.22724	29.23565	27.82962	30.96609	34.7138
7	24	37.35391	22.69287	29.02289	27.57381	30.64339	30.9813
7	25	36.04198	20.58272	28.98778	28.00668	30.14326	31.57113
7	26	34.55502	22.00571	28.91991	27.46315	30.34212	31.41792
7	27	35.66261	23.30367	28.87016	27.24464	30.15099	23.80142
7	28	34.60945	21.51234	28.89303	27.43005	30.43112	27.03583
7	29	36.01054	22.19518	29.18335	27.55415	30.81314	30.02802
7	30	34.73487	22.84949	29.21249	27.55202	31.02174	31.02174
7	31	35.30979	24.25476	29.40914	27.89278	30.74786	28.89117
8	1	33.79273	24.76804	29.50458	28.50795	30.59264	29.58061
8	2	33.79804	25.10773	29.50235	28.34113	30.75418	30.67268
8	3	35.67598	20.46339	29.38489	28.22005	30.93227	32.74132
8	4	35.41875	24.18774	29.79725	28.46573	31.3907	35.33552
8	5	35.57601	23.31533	29.50545	28.22365	31.1201	32.62983
8	6	36.13387	17.37427	29.38721	28.11257	31.34071	28.93033
8	7	37.18665	23.15248	29.26426	27.62595	30.95135	30.37683
8	8	35.82126	21.86518	29.30151	27.84783	30.93301	26.18676
8	9	34.721	20.85989	29.24904	28.32913	30.97367	27.05972
8	10	34.92059	19.90959	29.30243	27.51048	31.52542	25.75816

8	11	34.77177	22.53915	29.33777	27.315	31.32856	28.16614
8	12	34.68506	21.59604	29.2075	27.65067	31.01797	29.97433
8	13	34.18546	23.52841	29.20031	27.92905	31.05584	24.9276
8	14	34.81145	18.73027	29.26669	27.54199	31.21011	29.23335
8	15	34.20456	22.56772	29.27618	27.72202	31.36251	28.68465
8	16	34.26183	22.44196	29.33042	27.6381	30.93379	30.93379
8	17	34.23915	22.87361	29.1481	27.11868	31.24461	32.15598
8	18	34.52305	22.13861	29.00981	27.31495	30.74976	31.98852
8	19	33.34206	22.9166	29.00665	27.40206	30.99337	31.40129
8	20	34.62793	17.77005	28.93782	27.50768	31.34704	32.60095
8	21	35.27998	19.52927	28.74408	26.93195	30.88922	35.27998
8	22	36.17636	21.60517	28.84618	27.328	30.89907	35.54665
8	23	35.16695	21.00631	28.62443	26.53742	30.48294	33.56341
8	24	35.89372	17.15925	28.55894	26.85835	30.2015	32.53931
8	25	36.01907	20.25305	28.3262	26.89597	29.74347	32.68658
8	26	34.78155	22.61745	28.34644	27.00161	29.95399	33.14057
8	27	32.00718	20.97629	27.90127	26.86243	29.52006	30.64049
8	28	32.48351	21.00053	27.90685	26.56283	29.43964	30.30025
8	29	33.06038	19.85146	27.51997	26.17735	29.49426	30.9547
8	30	32.67507	19.03765	27.10247	25.42806	29.17082	29.65795
8	31	33.36504	20.9415	27.00054	25.21894	28.52997	29.27074
9	1	32.56224	13.73328	26.72128	24.73305	28.87136	30.08138
9	2	32.50355	15.08969	26.67239	24.95998	28.79802	30.3979
9	3	31.5914	19.3005	26.62371	25.23994	28.45911	30.06333
9	4	31.74251	15.11771	26.51043	25.04151	28.20403	25.95657
9	5	31.91804	18.33659	26.14491	24.81194	27.70502	22.25964
9	6	30.95294	20.04082	25.90817	23.98265	27.89719	26.63824
9	7	31.78157	14.96195	25.04071	22.6322	27.45402	28.07068
9	8	32.64407	16.69469	25.29068	23.40658	27.9803	28.00843
9	9	32.6925	18.1464	25.76085	23.8186	27.77782	26.71693
9	10	31.26131	15.73137	25.47192	24.04471	27.28291	26.81827
9	11	30.78045	17.00121	25.41196	23.88652	27.30087	25.21621
9	12	31.01987	16.08658	25.13796	23.38308	27.14516	26.36507
9	13	31.30453	17.23534	25.14876	23.71342	27.15586	27.269
9	14	31.41306	15.29864	25.0423	23.52557	27.13711	27.76888
9	15	32.42225	16.93867	25.09431	22.87643	26.9678	28.97749
9	16	32.90306	14.67139	25.02225	23.30759	26.81112	27.8864
9	17	30.58827	17.40022	24.85115	22.73091	26.88801	27.14356
9	18	31.7303	13.72235	24.63174	22.72597	26.5312	25.25572
9	19	29.85249	16.34791	24.28098	23.02348	26.04332	26.15891
9	20	29.47952	14.81819	23.9385	22.00249	26.5246	26.61097
9	21	29.96655	13.70055	23.40571	21.60387	25.42616	26.58766
9	22	29.74741	10.70892	23.15663	21.20071	25.03082	27.54011
9	23	29.66505	14.42375	23.30692	21.38832	25.33099	29.54688
9	24	31.05246	14.1505	23.25487	20.87476	25.41982	31.05246
9	25	28.11209	14.62769	23.20271	21.79811	25.58576	27.29182

9	26	29.49235	14.13349	23.03676	21.61795	25.04079	27.72088
9	27	29.94487	13.10133	22.84339	20.78033	25.11255	26.31317
9	28	29.92747	12.75866	22.65415	20.41543	24.71783	22.22519
9	29	31.93618	12.75938	22.34267	19.8563	24.89024	26.05254
9	30	31.0084	12.60852	22.05306	20.11806	24.52836	26.89069

Table A2. Wind Speed daily statistics (JAS) – ERA5 (km/h) (Figure 4.11.)

MONTH	DAY	Max	Min	Mean	25th Percentile	75th Percentile	2023
7	1	29.10142	2.482131	11.31732	6.389018	15.90354	6.389018
7	2	24.79768	2.244829	11.52449	7.178922	14.45434	10.6431
7	3	35.52441	3.134159	12.26573	7.567568	15.43073	13.10274
7	4	28.82932	2.244593	11.99075	6.68204	15.43981	7.865001
7	5	26.14777	2.380157	11.58016	6.270252	15.90307	17.33842
7	6	27.77514	1.861885	11.0845	6.109427	14.98757	15.85606
7	7	26.58121	2.154696	12.05775	7.945832	16.59245	11.38429
7	8	26.98368	2.544221	12.5355	7.595892	16.46856	16.31793
7	9	28.16132	1.563956	12.8332	7.980213	17.13286	11.27763
7	10	26.91899	2.594622	12.07898	6.686618	17.86384	8.813918
7	11	26.66183	3.070728	12.45169	7.944934	16.35218	9.316757
7	12	27.10162	2.065342	12.60565	7.615752	17.4041	7.553485
7	13	28.29133	2.289899	12.4379	8.410846	16.35507	5.630154
7	14	31.70599	2.222276	13.16689	8.695499	17.33176	7.178635
7	15	25.23875	2.458777	12.30139	7.566441	16.11775	14.38703
7	16	26.08595	2.480885	13.12599	9.096684	17.56634	13.27252
7	17	35.62736	1.415377	12.8955	7.996407	17.69963	13.88769
7	18	25.50934	3.618374	13.3649	8.416851	17.86565	10.94842
7	19	27.08587	1.703154	12.77795	7.599566	17.90878	9.462339
7	20	30.57558	2.196771	14.21301	8.56666	18.42545	6.093717
7	21	29.08452	2.653536	12.90882	7.386004	17.69193	8.865625
7	22	29.11009	2.490618	13.40615	7.941807	18.83913	6.203385
7	23	28.34499	2.388464	13.14828	8.379768	16.05605	9.509853
7	24	27.41587	2.78612	11.6012	6.632052	16.09959	8.71004
7	25	27.73587	2.028676	13.47672	8.723984	18.35855	11.24588
7	26	28.26067	2.344442	13.4722	7.909412	18.39623	21.67626
7	27	28.58127	2.116576	13.6281	8.96665	19.11125	22.09909
7	28	32.4865	2.614274	12.4595	7.716203	15.38541	5.565373
7	29	30.00598	2.767353	12.52792	6.331809	16.48796	9.212652
7	30	26.75521	2.980229	12.69514	8.301655	16.82089	9.556863
7	31	26.67313	2.58988	13.26159	7.837201	17.56462	13.48635
8	1	27.5022	2.339675	14.02387	9.403561	17.8256	5.051337
8	2	29.20256	2.701083	13.31426	8.442148	18.69996	10.58274
8	3	29.68769	1.924315	13.75399	7.992497	19.54808	6.220704
8	4	24.65925	2.521153	12.87608	8.050803	17.50192	10.04006

8	5	25.28272	3.021331	13.98449	9.124	18.9286	12.18032
8	6	28.61416	2.651017	14.27522	8.457281	19.87308	21.11117
8	7	27.72765	2.081118	13.9214	8.064222	19.39896	8.765492
8	8	28.24618	2.208476	13.66041	8.103036	19.22661	25.38994
8	9	30.05014	2.977334	13.5166	7.37783	17.83057	19.06714
8	10	24.66489	2.595776	13.70526	9.053451	18.16901	15.65961
8	11	28.14653	2.716138	13.45115	7.818775	18.94789	16.16178
8	12	29.19692	2.441832	13.76815	8.150482	18.50895	25.17116
8	13	27.15758	1.594398	13.33943	8.226035	16.84267	25.07975
8	14	27.03751	3.730229	13.46011	7.575181	18.78395	27.03751
8	15	28.36391	2.651123	13.1316	7.42204	17.86946	15.80442
8	16	29.94386	2.232438	13.97738	7.909315	18.33088	16.83131
8	17	29.11799	2.349175	14.38298	8.452785	20.09988	23.87141
8	18	31.07644	1.764699	13.70547	8.375132	18.1446	26.42158
8	19	28.16782	2.413261	14.41775	9.160716	18.95098	26.26374
8	20	27.40437	3.314837	14.4617	9.81023	20.14548	27.11624
8	21	27.61108	2.073946	14.25192	9.782043	18.50336	27.61108
8	22	29.5299	2.234801	13.43714	7.864877	19.36817	23.9152
8	23	32.18748	2.085535	13.93492	9.88847	17.3289	19.54411
8	24	30.47117	2.680137	13.37921	8.397669	17.90535	15.58639
8	25	27.54902	3.060095	13.69972	8.184061	18.62132	14.61868
8	26	35.68095	2.171072	13.34941	7.743424	18.47567	17.92155
8	27	36.65883	1.803839	13.46138	7.367191	18.28565	18.0118
8	28	29.1557	2.277929	13.76242	8.224886	19.67562	8.746077
8	29	25.00723	2.256372	14.02795	9.136755	19.30585	7.626574
8	30	30.08702	3.22929	13.82179	9.554708	18.03783	9.554708
8	31	25.17435	2.268546	13.32792	8.28077	17.80157	11.5935
9	1	28.83899	2.622657	13.67502	8.935108	19.06461	8.935108
9	2	28.99003	2.112006	13.45028	8.094654	18.45318	20.36038
9	3	28.42647	2.194833	13.86643	9.385888	19.11707	22.79269
9	4	34.89425	2.914725	12.98815	7.621956	17.88461	23.35563
9	5	30.09762	2.496302	14.37561	9.188276	20.40943	30.09762
9	6	31.7638	1.798613	13.82222	7.087829	19.25535	28.34982
9	7	30.59418	1.951338	14.26076	8.805379	18.07711	26.393
9	8	35.1936	2.457891	14.33355	7.068772	20.07746	27.4827
9	9	30.42305	2.008002	13.38472	8.570171	18.22193	22.99817
9	10	29.35549	1.883919	13.65822	7.306972	18.87497	26.84969
9	11	29.00687	3.039166	13.96451	8.748949	19.56803	24.31874
9	12	28.36431	1.243947	14.2251	7.872422	20.30927	15.60165
9	13	35.2772	2.167483	14.24105	10.31037	18.42339	7.747481
9	14	33.3038	2.845207	14.21777	9.542687	18.92044	3.721819
9	15	30.319	1.532905	12.19755	6.535285	16.81821	7.218611
9	16	28.71349	1.365452	13.51776	8.287681	17.5506	13.31091
9	17	32.18945	1.94692	13.10847	7.986989	18.16963	18.54743
9	18	32.17137	2.024721	12.67283	6.715164	17.95125	25.14136

9	19	31.87751	0.996903	13.83207	8.218564	17.73355	15.49619
9	20	32.83917	1.853833	13.49195	7.258324	18.34521	8.560987
9	21	31.37038	2.75472	14.47991	8.302602	19.02926	4.30903
9	22	29.905	2.347984	14.56679	9.556859	18.75456	9.666166
9	23	31.31668	1.405089	13.43292	7.363627	18.72711	4.952223
9	24	29.49474	1.948919	13.40736	6.922174	19.09687	11.83276
9	25	28.58879	1.998317	13.21842	7.800088	16.89239	27.85141
9	26	32.76054	1.950258	13.94283	7.223367	19.1332	29.70884
9	27	34.05285	2.588058	13.34999	6.87787	19.21342	30.42891
9	28	31.60332	2.718599	13.69419	8.470731	18.28673	16.69416
9	29	31.14302	1.578616	13.32967	8.3008	18.0602	17.41819
9	30	29.27439	1.700889	13.24404	6.853659	17.1237	21.49095

Table A3. Precipitation daily statistics (JAS) – ERA5 (mm/day) (Figure 4.12.)

MONTH	DAY	Max	Min	Mean	25th Percentile	75th Percentile	2023
7	1	38.81766	0	2.017545	0.004429	1.090363	0
7	2	21.31198	0	1.488634	0.00122	0.811755	0.001993
7	3	26.89603	0	1.533194	0.000109	1.017633	1.238709
7	4	12.06958	0	1.104982	4.3E-05	0.928017	0.056702
7	5	47.25975	0	1.180146	0.000367	0.516445	0.075924
7	6	16.54444	0	0.5955	0	0.432607	0.048637
7	7	6.292036	0	0.586334	5.73E-05	0.264182	2.047667
7	8	16.13584	0	1.00501	0	0.441166	1.357292
7	9	14.15325	0	0.640161	0	0.52087	0.012728
7	10	17.13319	0	1.208785	0	0.661644	0.00042
7	11	12.7561	0	0.926554	0	0.455962	5.24E-05
7	12	7.183285	0	0.623623	0	0.210542	0.006528
7	13	4.236614	0	0.321366	0	0.185139	0.239543
7	14	12.43355	0	0.54126	0	0.297009	1.365851
7	15	9.681539	0	0.52251	0	0.304283	0.005492
7	16	43.11141	0	1.21729	0	0.236545	0
7	17	5.647721	0	0.342093	0	0.064367	0
7	18	6.157551	0	0.35752	0	0.216506	0.001783
7	19	6.849777	0	0.501135	0	0.298962	0.000181
7	20	7.822597	0	0.393645	0	0.10831	0.192596
7	21	6.411124	0	0.290612	0	0.064464	0.063439
7	22	9.857507	0	0.375382	0	0.054469	0.008652
7	23	7.7264	0	0.536483	0	0.098418	0.008241
7	24	15.7739	0	0.752239	0	0.306054	0.004611
7	25	5.576324	0	0.455036	0	0.281887	0
7	26	15.60356	0	0.598671	0	0.211779	0
7	27	16.68956	0	1.143048	0	0.3697	2.995076
7	28	21.02202	0	0.948298	0	0.183823	0

7	29	6.850479	0	0.330707	0	0.114641	0
7	30	15.40259	0	0.776009	0	0.202878	0
7	31	6.283794	0	0.290366	0	0.192089	0.125981
8	1	3.588468	0	0.304897	0	0.210561	0.190003
8	2	6.767259	0	0.381743	0	0.131108	0.00369
8	3	6.071244	0	0.349023	0	0.065092	0
8	4	8.376749	0	0.391069	0	0.049904	0
8	5	10.84733	0	0.435469	0	0.30473	0
8	6	14.81822	0	0.60473	0	0.255983	0.641427
8	7	12.88078	0	0.550923	0	0.093156	0.093156
8	8	13.84162	0	0.446751	0	0.094386	0.065778
8	9	17.33208	0	0.610358	0	0.132298	0
8	10	6.696517	0	0.497994	0	0.322036	0.007985
8	11	4.880164	0	0.376261	0	0.119775	0.00536
8	12	8.866438	0	0.425005	0	0.155462	0
8	13	7.947072	0	0.400024	0	0.088677	5.189828
8	14	7.642946	0	0.43569	0	0.114079	0.04553
8	15	6.496512	0	0.375616	0	0.068288	0.254875
8	16	7.640769	0	0.304767	0	0.068904	0.008733
8	17	9.347688	0	0.503974	0	0.063868	5.24E-05
8	18	4.795963	0	0.266004	0	0.084664	0.022402
8	19	4.325963	0	0.382654	0	0.164061	0.098757
8	20	25.7464	0	0.781912	0	0.242904	0.004038
8	21	14.50289	0	0.687943	0	0.176424	0
8	22	5.834665	0	0.541076	0	0.213386	0.000973
8	23	4.906684	0	0.259694	0	0.11642	0
8	24	15.02355	0	0.5762	0	0.097595	0.299364
8	25	14.01072	0	0.493846	0	0.065263	0.00558
8	26	13.54266	0	0.380816	0	0.074649	0
8	27	5.966144	0	0.345808	0	0.139993	0
8	28	6.66128	0	0.48382	0	0.176434	0.000105
8	29	7.325616	0	0.402601	0	0.145909	0.001101
8	30	17.62017	0	0.800517	0	0.245481	0.004276
8	31	5.081092	0	0.499563	0	0.323336	0.185889
9	1	10.91046	0	0.799889	0	0.30016	0.006231
9	2	4.84558	0	0.322371	0	0.140544	0.074009
9	3	16.96655	0	0.663264	0	0.185565	0
9	4	5.414543	0	0.257812	0	0.086219	3.492239
9	5	46.26471	0	1.4244	0	0.358576	2.733816
9	6	19.57154	0	0.96873	0	0.203763	0.426558
9	7	19.33972	0	1.513264	0	0.385175	0.126249
9	8	16.73281	0	0.756893	0	0.192521	0.044693
9	9	16.65846	0	0.463842	0	0.164722	0
9	10	30.54494	0	0.978964	0	0.264435	0.060183
9	11	29.91922	0	1.32277	0	0.232768	0

9	12	14.58474	0	0.866619	0	0.154162	0
9	13	15.01066	0	0.680999	0	0.118272	0
9	14	18.3807	0	0.397296	0	0.047509	4.3E-05
9	15	33.25484	0	0.69761	0	0.068359	0.011339
9	16	14.20097	0	0.452367	0	0.145338	0.023561
9	17	19.0007	0	0.531627	0	0.044109	0.089642
9	18	45.28265	0	1.086834	0	0.148783	0.023732
9	19	20.17317	0	0.640971	0	0.125661	0
9	20	31.10336	0	1.329678	0	0.188007	0.01085
9	21	9.461341	0	0.791971	0	0.419437	0.003415
9	22	51.24688	0	1.375264	0	0.186582	0
9	23	21.463	0	0.851414	0	0.190824	0
9	24	30.14483	0	1.481787	0	0.435788	0.002665
9	25	17.53447	0	0.946673	0	0.137934	0.034397
9	26	29.61576	0	1.660396	0	0.080305	0.064806
9	27	46.60827	0	1.958747	0	0.218729	0.632491
9	28	37.99691	0	1.629535	0	0.249404	3.475244
9	29	37.02019	0	2.42558	0	0.599842	0
9	30	14.38711	0	0.888308	0	0.231741	0

Table A4. Relative Humidity daily statistics (JAS) – ERA5 (%) (Figure 4.13.)

MONTH	DAY	Max	Min	Mean	25th Percentile	75th Percentile	2023
7	1	87.26907	30.37294	48.6543	41.70842	55.53963	44.46838
7	2	75.56993	28.24013	48.07356	40.39021	53.21973	49.26703
7	3	86.83646	27.03841	47.72102	39.64507	53.96909	52.9486
7	4	81.80242	26.34509	48.36854	41.92757	53.27155	47.80363
7	5	77.30765	27.06622	46.3598	40.65852	51.50206	46.72657
7	6	85.49683	29.62039	45.42899	39.02789	50.80494	41.81614
7	7	67.44054	25.78518	45.46489	38.7029	51.22049	48.16085
7	8	83.65449	21.50518	46.1636	39.3763	51.38607	48.4746
7	9	77.87955	25.56952	45.5769	39.97654	51.16077	40.36241
7	10	81.22379	27.10812	45.2084	38.16706	51.86759	37.5226
7	11	70.06492	27.85949	44.40248	38.25091	49.09409	38.52793
7	12	67.87246	27.96022	44.69282	38.381	49.66838	44.08622
7	13	69.85518	27.98432	42.95606	36.95802	48.94282	45.73597
7	14	74.08948	24.03943	43.58614	38.82378	47.80265	48.15713
7	15	61.54156	24.29766	43.19116	38.61297	46.80382	46.07259
7	16	77.37228	23.51813	44.40683	37.78816	48.27686	39.64797
7	17	76.77954	25.92137	42.96351	36.5275	47.15719	34.97879
7	18	70.85023	23.51218	42.96605	36.92711	47.38515	36.92711
7	19	66.99138	23.89342	42.84101	37.2254	48.35282	39.51706
7	20	70.91452	25.375	42.72208	36.82038	47.44887	41.20544
7	21	72.13564	25.78617	41.76258	37.17376	44.8792	38.60369

7	22	70.0044	23.95008	41.40797	35.90395	46.87888	48.88868
7	23	65.69099	25.9127	41.77986	36.04268	46.38264	34.40635
7	24	70.51154	24.79353	43.56912	36.28621	48.17542	44.53146
7	25	67.98578	28.24465	44.20096	38.58589	49.78773	50.35327
7	26	66.85527	28.5603	43.61547	37.31383	48.94345	50.46772
7	27	74.05891	25.90731	43.60622	36.72908	49.43221	59.46084
7	28	84.22005	22.2748	43.07561	35.51579	49.99385	35.32621
7	29	71.98262	23.10505	42.14522	35.36041	47.87214	35.89617
7	30	78.81527	23.94895	42.7314	35.56721	48.77408	37.42402
7	31	67.54424	21.60912	42.20046	36.27049	48.28495	43.5281
8	1	73.17227	24.58085	42.16448	36.36002	47.0621	47.14633
8	2	65.13835	24.83891	41.11997	35.58429	47.47195	48.94662
8	3	66.12328	24.03492	40.61466	34.93279	45.56323	44.92603
8	4	63.97842	26.92332	39.69448	34.44336	42.10194	36.81479
8	5	57.95114	24.29633	40.66757	35.06761	45.29758	46.39903
8	6	73.65925	26.20043	41.97704	36.43898	45.34883	62.46075
8	7	66.60313	25.48694	41.52791	35.00714	46.89521	38.98993
8	8	81.22469	25.69124	41.37836	33.60672	46.24644	44.31994
8	9	83.90797	24.38421	42.11889	35.6573	46.59201	38.04648
8	10	74.18777	22.95547	41.35838	35.70171	45.78874	46.86643
8	11	61.64631	23.05759	41.1047	35.19124	46.53072	37.30037
8	12	60.17898	21.32089	41.06774	33.15217	47.5198	33.07824
8	13	68.60369	21.41507	40.10836	34.8336	44.41531	61.53479
8	14	78.4168	21.03453	39.69315	33.5042	44.24932	51.24092
8	15	67.03221	23.056	40.75501	34.98695	45.67261	64.91156
8	16	59.93404	23.36714	40.50249	34.56223	45.82012	51.37349
8	17	62.33787	19.49775	41.18963	36.54903	46.36284	43.83002
8	18	64.8737	20.54062	40.05115	35.22957	44.74962	44.17384
8	19	79.52046	21.38163	40.54508	34.09634	45.97084	39.2917
8	20	72.94926	22.79582	41.29898	34.1847	46.25344	34.79996
8	21	78.979	20.74209	42.05368	35.97536	47.64006	21.19675
8	22	66.24207	20.30898	42.36664	35.82569	48.33586	27.04773
8	23	68.64191	22.04253	41.85417	34.59708	48.77153	33.44212
8	24	70.35345	22.52649	41.28795	33.70111	47.78722	40.9292
8	25	76.4608	17.5014	42.67081	35.41904	47.81551	39.4956
8	26	84.76004	25.00462	41.90588	35.82823	46.94057	33.65921
8	27	73.67439	26.50629	42.67	36.78175	47.84138	40.23977
8	28	64.73939	20.92195	41.47192	35.82404	46.6162	43.71659
8	29	68.55539	19.83935	42.78597	37.57322	47.56869	45.15163
8	30	71.11504	22.90764	43.80116	36.66811	49.45283	49.45283
8	31	64.26594	26.1499	44.38749	37.70206	50.2142	52.66138
9	1	75.53568	18.52161	43.80422	36.52575	48.89132	36.52575
9	2	77.11899	20.37774	43.18221	36.54445	47.68929	37.42316
9	3	84.47427	26.17379	43.76528	37.89004	47.50998	34.42327
9	4	65.37971	24.74692	42.60191	37.48038	47.56069	47.71988

9	5	81.46024	25.01265	45.08553	36.7795	50.70066	75.44262
9	6	78.71164	25.60107	43.73542	36.94382	47.71473	54.41924
9	7	89.01945	22.76277	45.70309	38.85247	50.22743	44.86093
9	8	83.8907	22.41482	43.83956	36.98245	48.98039	41.0984
9	9	70.21564	19.4935	43.77581	37.47531	48.90307	35.517
9	10	85.64912	23.74757	45.21618	38.35631	49.679	42.16856
9	11	78.46413	27.45491	45.84411	38.75131	51.1901	41.21384
9	12	84.23281	27.4052	46.73846	39.38322	51.39938	39.46637
9	13	81.47155	27.49067	46.55617	40.21883	49.88711	45.64669
9	14	92.90828	24.04663	44.43534	37.7414	49.49842	42.18819
9	15	85.75948	26.40269	45.63135	37.80422	50.23343	37.80422
9	16	75.31183	26.21124	46.26264	38.30961	53.4333	41.10871
9	17	86.23325	26.50083	46.03123	38.33002	50.77348	48.81125
9	18	86.81164	25.78105	46.79794	39.16162	53.35045	43.5563
9	19	82.80585	27.66443	47.68803	40.58816	52.57442	43.71584
9	20	81.98	28.40269	47.20887	41.26325	50.63761	44.63806
9	21	76.87238	23.51642	46.93084	41.38229	51.90791	47.10891
9	22	83.855	23.06957	47.55749	39.36065	52.67324	47.60474
9	23	76.72415	25.63331	47.57437	38.50426	54.78971	48.4259
9	24	88.54243	24.55655	48.93846	39.11256	55.08833	39.11256
9	25	97.82335	20.82619	49.42748	40.6349	53.92783	48.62337
9	26	92.8476	27.14254	50.52184	42.9651	55.97408	45.06315
9	27	90.07796	25.58296	51.37333	40.82749	58.39988	49.48108
9	28	96.7884	28.33131	51.56218	41.37375	59.57452	70.31747
9	29	96.24777	20.61261	53.15284	40.8248	59.36076	38.11662
9	30	83.75871	20.58063	50.19424	41.47855	54.92679	29.43746

Table A5. Histogram 1940-2024, ERA5 (Figure 4.14.)

bin	Value Frequency
5	15329
10	3574
15	2497
20	1932
25	1670
30	1512
35	1321
40	1060
45	755
50	544
55	377
60	228
65	142
70	61
75	24

80	17
85	2
90	2

Table A6. FWI daily statistics (JAS) – ERA5 (Figure 4.17)

DayOfYear	Min	Max	Mean	25th Percentile	75th Percentile	2023
07-01	0.010196	61.50262	18.20076	7.5406	26.48837	14.14386
07-02	0.36419	58.10225	18.79984	6.418519	27.3433	17.42245
07-03	0.022256	58.79985	19.36666	9.091045	28.91921	13.67484
07-04	0.246789	56.86171	18.70075	8.748118	25.74041	16.09439
07-05	0.083883	50.50968	20.11721	10.19202	26.55587	25.33644
07-06	0.029943	54.13193	21.5104	12.54745	29.18725	27.34874
07-07	0.506677	56.01114	22.68804	13.99989	32.28775	12.39991
07-08	0.138227	62.71726	22.18942	12.68428	31.9868	17.43102
07-09	0.741427	55.0484	23.14205	14.37313	32.64047	22.72719
07-10	0.572145	53.42698	22.18715	12.84547	31.8866	24.36814
07-11	0.66664	49.66817	23.32772	15.19326	31.50202	25.82023
07-12	0.635031	54.62373	24.52792	16.60961	32.71672	25.0232
07-13	1.529101	61.54403	26.11883	16.60872	35.27623	24.06388
07-14	0.09191	68.93902	26.97008	17.46686	35.37556	17.87584
07-15	1.70985	58.31228	26.16676	18.54282	33.64614	29.5435
07-16	0.244438	64.86493	26.95324	19.7472	32.98285	32.43211
07-17	0.208727	63.26195	28.1969	19.89055	36.3855	37.00376
07-18	0.196283	60.07354	29.59091	22.25998	36.1667	34.28899
07-19	0.841417	66.96106	28.08697	20.23704	35.21676	33.27493
07-20	0.743582	63.80831	30.53406	22.98737	38.74575	30.24284
07-21	0.492195	73.24309	31.11116	22.27524	38.88399	33.79731
07-22	0.112794	78.29335	32.36381	23.12856	40.00601	28.60352
07-23	0.705192	75.27584	31.28161	22.29326	39.50911	36.40832
07-24	0.537913	62.96641	28.41877	20.858	37.59959	33.16457
07-25	0.539893	69.71484	30.64379	21.83253	38.10777	33.25074
07-26	0.595747	70.63504	31.48461	22.9643	40.2592	46.41681
07-27	0.046145	62.15498	30.07956	19.82255	40.61735	14.08265
07-28	0.010465	70.33471	29.46456	19.64177	40.67912	21.38995
07-29	0.696631	68.97448	30.76301	18.47543	40.4473	31.14753
07-30	0.20893	56.83605	30.85475	22.92502	40.89761	32.32787
07-31	2.904563	65.84468	32.6257	24.31994	42.32011	37.32127
08-01	2.065278	67.03095	33.90247	24.64884	43.74519	27.18308
08-02	2.830042	66.86666	33.88114	24.82581	42.7578	32.45144
08-03	3.762681	74.99149	34.5054	23.82488	44.69439	28.33169
08-04	1.577857	68.23063	34.14655	24.0319	45.71602	36.84479
08-05	0.929695	59.054	34.80362	23.26876	45.65675	37.79363
08-06	0.808972	67.28564	34.88257	24.47498	46.08145	35.99829
08-07	1.944381	68.34087	34.47678	23.85115	47.27024	31.04232
08-08	0.558479	68.4166	34.75387	26.70661	46.15503	53.74643

08-09	0.352937	70.6179	34.24898	23.48497	44.37317	44.37317
08-10	1.928876	63.94913	34.25584	24.89055	43.41661	38.51122
08-11	3.63859	75.80672	34.24934	23.88491	43.44281	41.1903
08-12	1.78084	76.95822	35.11434	24.93099	43.61336	60.75195
08-13	1.226872	72.37377	35.26431	25.23526	43.77021	13.22006
08-14	2.387691	77.7112	35.31229	27.0806	46.79537	38.18308
08-15	2.951707	66.35267	35.00364	23.44163	47.29809	26.46205
08-16	2.643241	70.4516	36.78311	25.73207	46.1449	31.50415
08-17	0.478143	78.21466	36.53631	24.98544	43.31882	46.60848
08-18	4.511625	79.28244	36.43282	26.20333	45.47193	51.25241
08-19	4.781576	77.77088	36.66999	26.42446	47.56615	54.91749
08-20	0.604753	73.91691	36.51769	26.58887	48.85384	62.48973
08-21	0.366159	84.53464	35.37257	27.25251	46.31611	84.53464
08-22	0.739084	77.04416	34.21394	24.29146	43.22144	76.69501
08-23	0.634658	67.63004	35.67541	26.55657	44.4164	60.79293
08-24	0.914293	67.04503	34.87762	26.74764	45.81308	47.24156
08-25	0.056157	87.16004	35.42135	26.22238	44.75548	46.2389
08-26	0.184092	77.20288	35.54636	25.97613	46.88957	51.81332
08-27	0.994561	80.22143	35.39691	27.18208	46.74657	50.24035
08-28	5.426025	85.86321	34.73305	22.02216	48.3983	35.28152
08-29	6.290971	75.56585	34.01145	22.87473	44.2442	33.40505
08-30	0.860967	72.90726	32.72201	23.47991	40.46975	32.86264
08-31	0.963301	63.58078	31.53727	23.11222	41.10299	33.08478
09-01	0.730353	64.32367	31.39107	23.00081	44.75176	34.2469
09-02	1.759508	65.0216	31.89071	22.48921	43.21751	49.94471
09-03	0.247977	63.64704	32.03389	21.28958	41.70233	56.34985
09-04	2.869764	60.52822	32.07748	23.43855	41.45883	20.94447
09-05	0.372286	63.98965	31.22341	23.55697	38.93938	14.95699
09-06	0.058739	65.92253	30.13011	19.70276	38.64004	34.74609
09-07	0.014197	63.09255	29.42497	19.04422	40.70952	44.95873
09-08	0.063116	66.08352	30.40865	19.67297	41.25009	51.08193
09-09	0.051497	66.29508	30.07789	20.47554	39.89868	48.2829
09-10	0.005018	63.02266	29.85262	19.00672	40.25361	55.19273
09-11	0.155487	68.25489	29.9066	19.54716	38.53435	51.59225
09-12	0.34632	66.98423	28.48312	16.93059	39.49263	39.49263
09-13	0.31351	65.4511	28.77834	20.01571	36.9369	29.85165
09-14	0.000281	77.88554	30.61483	20.33955	41.40634	26.29092
09-15	0.013096	67.32858	28.96413	21.07647	37.49076	30.09113
09-16	0.077607	65.21481	29.8625	19.88866	37.99715	37.28459
09-17	0.13712	67.5012	29.322	22.023	36.93231	41.57071
09-18	0.001923	55.21	28.03248	20.45426	38.48419	51.74263
09-19	0.1393	59.81967	28.3068	17.91205	37.39525	38.28913
09-20	0.000956	54.60225	28.08492	18.40639	38.19763	30.63671
09-21	0.050507	61.67643	27.54204	17.8912	36.27775	26.49015
09-22	0.099902	68.19356	27.45436	16.20525	36.82568	32.07876
09-23	0.579428	67.04594	25.58252	18.48986	34.57537	27.5308

09-24	0.001495	57.1317	25.16973	16.17772	34.78535	36.61207
09-25	5.89E-06	57.44715	25.14293	16.63592	33.55199	57.44715
09-26	0.006353	61.23345	24.97078	12.7663	34.04513	61.23345
09-27	0.000349	63.93303	24.00788	11.84411	31.66125	51.96008
09-28	6.39E-07	56.31026	23.11547	14.08398	31.56211	8.653024
09-29	1.38E-05	52.16125	22.16526	12.13141	31.2488	30.64549
09-30	0.064327	51.56828	22.00028	8.717638	32.94933	51.56828

Table A7. Histogram 1941-2019, Obsclim (Figure 4.19)

bin	Value Frequency
0	18504
5	3431
10	2451
15	1881
20	1444
25	694
30	310
35	110
40	26
45	2
50	1
55	0

Table A8. FWI daily statistics (JAS) – Obsclim (Figure 4.21.)

Date	Min	Max	Mean	25th Percentile	75th Percentile
07-01	0.032327	26.53496	9.698973	2.926898	16.99094
07-02	0.000635	30.80235	10.13734	3.480704	15.80091
07-03	0.043038	30.76181	9.9201	4.193459	15.06958
07-04	0.006797	25.02987	9.898669	3.766985	14.64202
07-05	0.001939	25.81998	10.99233	6.282363	15.67288
07-06	7.49E-06	29.45015	11.97147	6.345529	17.25115
07-07	0.009056	34.55458	12.17929	7.157895	16.76591
07-08	0.010313	28.30979	11.72243	6.894832	17.44387
07-09	0.036709	32.30024	11.47547	4.841088	16.9549
07-10	0.038599	37.35005	11.53796	4.297652	15.94025
07-11	0.00576	33.29054	11.92232	5.622686	17.33242
07-12	5.61E-05	34.16094	12.49604	7.140076	16.48909
07-13	0.001758	36.631	13.42006	8.75489	17.78097
07-14	0.095466	41.91415	13.34583	9.206806	18.35333
07-15	0.137895	36.14139	13.26473	6.460348	18.60305
07-16	0.697349	30.0922	14.18151	8.895781	18.69228
07-17	0.498661	33.93935	14.80681	10.03248	19.2759
07-18	0.847148	37.02545	15.27629	11.09108	20.1108

07-19	0.885225	39.60135	16.26383	11.52043	21.01615
07-20	1.63692	35.58077	17.10126	11.28382	20.68443
07-21	0.866105	37.23618	17.69741	12.82399	22.65519
07-22	0.62924	40.25928	17.49141	13.40737	21.73801
07-23	0.076292	40.23043	17.40238	13.88638	21.35965
07-24	0.055142	38.77274	17.17687	13.46653	21.92514
07-25	0.037748	51.80154	17.21157	13.3542	22.69265
07-26	0.001231	39.75136	15.89707	9.867685	21.74847
07-27	0.001239	38.16093	15.8925	9.967827	22.46741
07-28	0.246616	39.65241	16	8.261559	22.58411
07-29	0.047336	39.46574	15.8457	7.642133	22.7054
07-30	1.46E-05	39.63272	16.78596	9.677607	22.90094
07-31	7.49E-05	42.69083	16.52371	6.847722	24.14028
08-01	0.00044	34.97671	17.35773	8.813184	24.75245
08-02	0.184137	35.34491	17.63094	10.05685	23.88344
08-03	0.556305	34.24474	17.66916	10.97837	22.92646
08-04	0.223281	37.23714	17.90871	11.57463	22.44651
08-05	0.105823	37.96302	18.61936	11.77977	24.50784
08-06	0.038877	35.56501	18.39892	11.72937	25.25358
08-07	0.017344	39.22999	18.20879	11.66675	25.02328
08-08	0.362042	43.27366	18.44506	11.96042	25.30285
08-09	0.083021	40.45779	17.92854	10.74194	23.70044
08-10	0.479293	39.75302	18.86541	12.28631	26.11201
08-11	0.591703	37.24988	19.07507	12.07825	25.85102
08-12	0.506772	37.14166	18.38348	11.55774	24.41403
08-13	0.33735	38.11871	18.60993	13.38865	24.82232
08-14	0.081287	43.68187	18.62901	11.66567	26.0865
08-15	0.255475	43.12831	19.03267	12.15379	24.49144
08-16	0.073915	44.38952	18.52257	12.04121	26.80464
08-17	0.410503	43.06468	19.17885	12.47424	25.39682
08-18	1.228991	38.74277	19.44952	13.20029	25.95533
08-19	0.158586	40.59955	19.78516	13.41948	25.76924
08-20	0.596414	40.03992	19.68108	13.30058	25.88936
08-21	0.157962	38.89025	18.87942	12.78023	25.28255
08-22	0.907887	39.07227	18.81262	12.23512	24.55133
08-23	0.126734	42.81599	19.05907	12.11698	25.27377
08-24	0.060436	46.06064	18.87535	13.17399	24.89892
08-25	1.880823	42.09166	19.11522	12.80721	25.78233
08-26	0.180901	45.2408	19.2856	12.42513	25.5694
08-27	1.213966	41.91004	19.24916	13.14418	25.79359
08-28	0.053391	39.10867	18.95717	12.74616	25.15982
08-29	0.057895	34.12185	17.48812	11.04353	25.13385
08-30	0.45852	38.43893	18.08818	12.02926	24.10865
08-31	0.178117	36.59673	17.88467	12.144	24.94249
09-01	0.294276	38.19679	17.77475	11.30202	25.3142
09-02	0.08339	40.55912	17.60956	9.805167	24.97899

09-03	0.081232	39.05688	17.62856	12.13823	22.14501
09-04	1.69E-05	34.94809	17.4369	12.77944	23.57847
09-05	0.003193	33.58044	16.74975	10.88307	23.34783
09-06	0.052608	32.19416	16.15751	9.305149	23.93305
09-07	0.002199	35.04402	15.72395	8.181814	23.15277
09-08	0.078436	38.20556	16.17918	8.449587	22.66847
09-09	0.333318	32.19241	16.11202	8.993507	22.41512
09-10	0.061553	35.58146	16.05839	7.873615	22.5413
09-11	0.011033	33.85595	15.48104	8.705003	23.88528
09-12	0.047489	40.43728	15.35911	8.139735	22.36565
09-13	2.41E-05	40.03815	15.64706	8.704499	22.55037
09-14	0.00208	32.93363	15.54637	8.965776	22.05991
09-15	0.002014	32.97694	15.55238	10.45467	20.61085
09-16	0.036048	33.59162	15.62706	10.37976	20.72098
09-17	0.00128	31.95068	14.5012	8.856323	20.54627
09-18	0.03071	27.22609	14.24716	9.023847	19.99178
09-19	0.000103	32.1096	14.69852	9.856935	20.5263
09-20	0.004791	28.82237	13.76094	6.52586	20.35564
09-21	0.004956	31.16547	14.2452	8.465787	20.13303
09-22	0.203381	31.89797	13.38711	8.914712	18.72678
09-23	2.61E-05	29.92523	12.73634	7.466814	18.38941
09-24	4.06E-06	34.62922	12.50501	5.529791	18.85525
09-25	3.45E-07	40.55165	11.67805	3.722566	16.89543
09-26	9.1E-06	37.10177	11.73354	3.46458	17.01375
09-27	7.35E-08	27.20003	11.04878	3.758298	16.39835
09-28	1.46E-06	25.87949	10.37057	1.894652	16.00649
09-29	7.93E-07	31.89826	9.290935	1.344998	15.69378
09-30	7E-06	30.12102	9.659394	1.70177	17.02916

Table A9. Histogram 1941-2019, Counterclim (Figure 4.23.)

Bin	Value Frequency
0	19036
5	3476
10	2532
15	1993
20	1175
25	477
30	140
35	24
40	1
45	0

Table A10. FWI daily statistics (JAS) – Counterclim

Date	Min	Max	Mean	25th Percentile	75th Percentile
07-01	0.020662	25.66392	9.021871	2.666268	15.75686
07-02	0.000227	29.70528	9.422679	3.19325	14.77682
07-03	0.018065	29.69107	9.198986	3.715847	14.14737
07-04	0.00412	24.33135	9.175667	3.33251	14.03208
07-05	0.00127	25.09094	10.16806	5.688697	14.58652
07-06	4.76E-06	27.32588	11.08089	5.825483	15.93801
07-07	0.006472	31.79276	11.25588	6.523086	15.35502
07-08	0.007502	26.34006	10.81251	6.361607	15.95917
07-09	0.027658	29.82724	10.58288	4.076008	15.38633
07-10	0.01605	33.81644	10.56729	3.613164	15.1284
07-11	0.004002	29.44412	10.88923	4.648327	16.23468
07-12	3.63E-05	30.54672	11.41357	6.100963	15.43809
07-13	0.000667	33.31435	12.24507	7.72247	16.58531
07-14	0.071262	37.83082	12.15292	8.399036	17.26429
07-15	0.056895	32.91833	12.00588	5.418953	16.69915
07-16	0.5694	27.14179	12.88284	7.969904	17.10683
07-17	0.366004	30.44589	13.45751	9.141956	17.70968
07-18	0.672618	33.24919	13.82949	9.338522	18.26364
07-19	0.770092	35.42603	14.65701	10.10189	19.32226
07-20	1.235264	33.32865	15.40884	9.838061	19.53366
07-21	0.71099	35.5372	15.91912	11.26206	20.50265
07-22	0.397504	38.33275	15.76732	11.37227	19.91719
07-23	0.021837	36.87842	15.596	12.29803	19.4413
07-24	0.011877	35.01495	15.33491	11.57749	19.99537
07-25	0.006991	44.9617	15.20549	10.87246	20.7447
07-26	0.000146	35.02847	14.0301	7.894377	19.87329
07-27	0.00024	33.79447	13.99695	7.34499	19.88059
07-28	0.091724	35.02433	13.967	6.314314	21.01603
07-29	0.017033	34.0207	13.67988	5.640884	20.36285
07-30	6.41E-06	34.2152	14.46505	7.589492	20.17386
07-31	3.24E-05	36.4901	14.11239	5.245234	20.49759
08-01	0.00021	30.5891	14.88349	6.741469	21.55022
08-02	0.129778	32.39304	15.17073	8.277422	20.73947
08-03	0.392545	30.14912	15.18782	8.373431	20.06945
08-04	0.163116	31.00158	15.25075	8.744044	20.55714
08-05	0.018689	34.17195	15.97147	9.508089	21.31366
08-06	0.02088	30.23854	15.73277	9.239002	22.40139
08-07	0.009314	33.85497	15.54115	9.506737	21.28752
08-08	0.308219	37.0156	15.66249	10.33451	21.02702
08-09	0.01782	34.09812	15.09305	7.734493	20.66234
08-10	0.145823	34.41545	15.99587	9.549368	21.66466
08-11	0.188096	30.92335	16.05857	9.490652	22.18995
08-12	0.12331	33.80519	15.49768	8.637346	21.31565

08-13	0.171797	31.66954	15.75363	10.71935	21.44815
08-14	0.03284	35.87887	15.78413	9.197306	23.15697
08-15	0.058782	34.97104	15.85974	9.266249	22.05666
08-16	0.025851	34.45464	15.5875	9.144294	22.47394
08-17	0.274036	33.94947	16.21922	10.08083	22.21235
08-18	0.626078	31.0415	16.5341	11.1097	22.40787
08-19	0.090818	31.51955	16.81228	11.3078	22.01111
08-20	0.134701	36.45632	16.76964	10.40228	21.96426
08-21	0.061294	31.97523	16.01553	10.2535	21.98519
08-22	0.685142	31.93799	15.89492	9.856924	21.59409
08-23	0.065621	35.11265	16.19914	9.82722	22.19396
08-24	0.025457	37.40365	16.07624	11.12881	22.43146
08-25	0.994545	34.46657	16.22486	10.37092	21.76977
08-26	0.080933	38.02031	16.42942	10.26703	22.8503
08-27	0.471832	38.69155	16.37203	10.04228	22.86993
08-28	0.02662	33.75653	16.14599	10.94762	21.78024
08-29	0.032161	29.20305	14.98884	8.697048	21.25306
08-30	0.244233	35.22167	15.50269	10.05585	21.35439
08-31	0.06806	30.02401	15.40475	9.875857	22.09225
09-01	0.179449	35.37928	15.33771	9.248465	21.59653
09-02	0.01815	37.53328	15.20943	7.295946	21.73037
09-03	0.040252	36.30842	15.26215	9.767271	19.47789
09-04	6.97E-06	32.53948	15.12979	10.65508	19.87523
09-05	0.00022	31.66239	14.61776	8.906456	20.4854
09-06	0.01489	29.98809	14.14161	7.618549	21.30712
09-07	0.000732	29.94686	13.85812	6.140837	20.90439
09-08	0.037341	36.84308	14.32794	6.40763	20.28392
09-09	0.25757	30.24995	14.23955	6.994781	20.33699
09-10	0.019673	30.65711	14.31729	6.846893	21.47976
09-11	0.008878	31.90262	13.84391	7.617326	21.79295
09-12	0.024942	31.24428	13.72759	6.902576	21.18817
09-13	5.17E-06	31.93776	13.94091	7.509129	19.79359
09-14	0.001187	29.60573	13.92415	7.24607	19.68778
09-15	0.001321	29.24514	13.99718	8.673146	18.64495
09-16	0.02546	31.72751	14.22537	9.325564	18.99137
09-17	0.000774	27.86152	13.26925	8.676677	18.81019
09-18	0.013305	24.91214	13.11094	8.211285	18.73049
09-19	3.87E-05	30.31976	13.52278	8.823114	19.26876
09-20	0.00212	27.37868	12.74268	6.667538	19.00339
09-21	0.001622	29.33307	13.13505	7.669547	19.05539
09-22	0.166221	27.56817	12.35302	7.801606	17.45532
09-23	1.54E-05	28.49734	11.82078	7.004749	16.87886
09-24	2.65E-06	29.22269	11.59988	4.819214	17.28729
09-25	2.17E-07	34.12639	10.81558	3.626984	16.17347
09-26	5.62E-06	31.52481	10.92969	3.285048	16.0111
09-27	3.63E-08	25.38579	10.4455	2.763259	16.24623

09-28	5.7E-07	25.10374	9.760131	1.867151	14.76305
09-29	6.65E-07	30.83718	8.831771	0.904952	14.59373
09-30	2.63E-06	29.00072	9.097651	1.296898	15.8545

Figure A1. FWI per day – ERA5

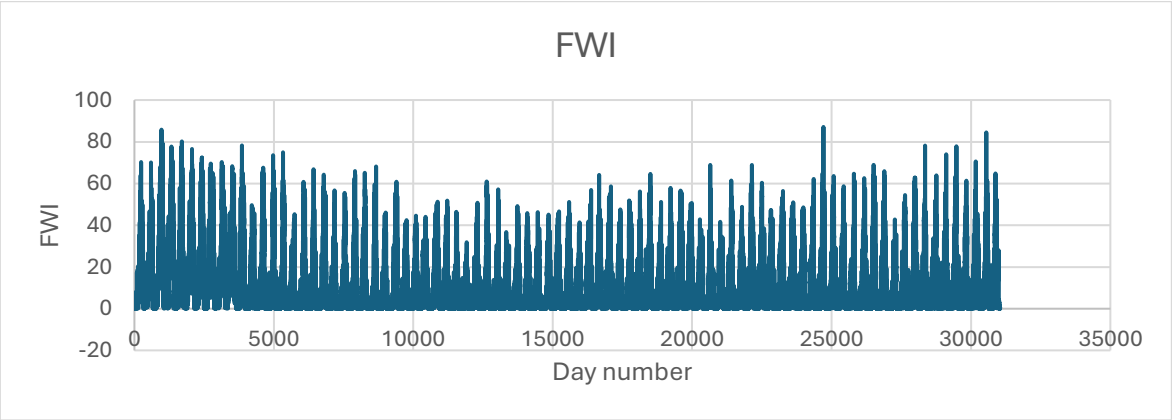

Figure A2. FWI per day - Obsclim

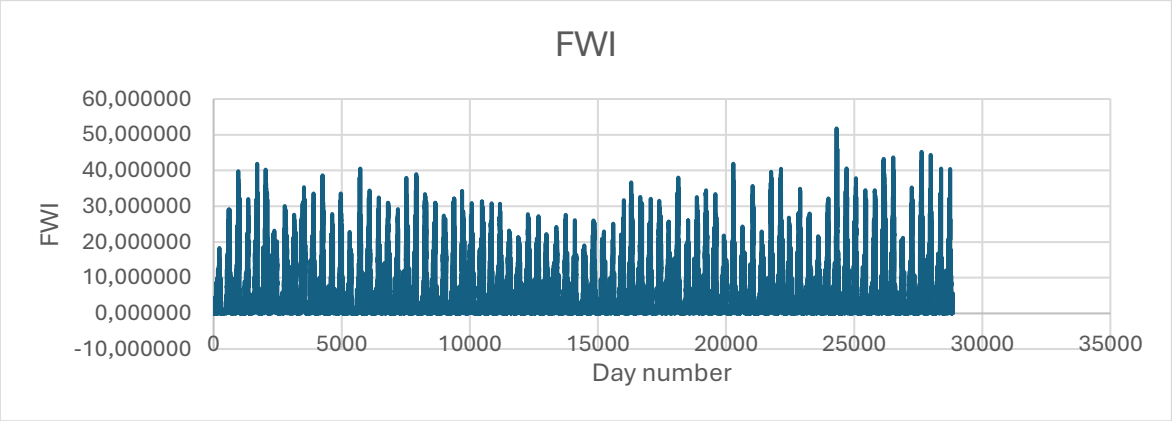

Figure A3. FWI per day – Counterclim